

**EVALUATING THE INFLUENCE OF THE LAND SURFACE AND AIR
TEMPERATURE GRADIENT ON TERRESTRIAL FLUX ESTIMATES
DERIVED USING SATELLITE EARTH OBSERVATION DATA**

SAMEERA KHAN

Submitted in fulfilment of the requirements
for the degree of MSc Hydrology

School of Agricultural, Earth and Environmental Sciences
University of KwaZulu-Natal
Pietermaritzburg
South Africa

March 2020

Supervisor: Ms KT Chetty
Co-Supervisor: Dr S Gokool

ABSTRACT

One of the most challenging processes of the hydrological cycle to determine accurately especially in arid and semi-arid regions, is actual evapotranspiration (ET_a). Numerous approaches are recognised and have been established to account for ET_a at various spatial and temporal scales. Satellite earth observation (SEO) methods have been utilised as an alternative to conventional methods to estimate ET_a , as they provide estimates over larger geographical scales.

Satellite-based ET models have been shown to provide fairly reliable estimates of terrestrial fluxes and ET_a . However, these models have the tendency to perform poorly in water stressed environments due to an inherent limitation in their conceptualisation, which relates to the temperature gradient ($T_o - T_a$). Due to the dynamic nature of the $T_o - T_a$ gradient, the study aimed to establish whether the selection of an image based upon the satellite overpass time influences the accuracy of the modelled flux and ET_a estimates. For this purpose, the Surface Energy Balance Systems (SEBS) model was implemented using SEO data using Moderate Resolution Imaging Spectroradiometer (MODIS) imagery. The simulated fluxes and ET_a were compared against *in-situ* Eddy Covariance (EC) data, as well as ET_a estimates obtained from MOD16 to quantify the influence of $T_o - T_a$. The study was undertaken during the 2015 dry period within the Luvuhu and Letaba Water Management Area, situated in the semi-arid north-eastern region of South Africa. This period coincided with a large El Niño induced drought, which provided an ideal opportunity to assess the model's ability to adequately simulate ET_a during conditions of water stress.

The results of the investigations undertaken in this study indicated that both the ET_{Terra} and ET_{Aqua} largely overestimated ET_a when compared to *in-situ* riparian ET_a measurements, yielding a Relative Volume Error (RVE) of -123.04% and -159.41%, respectively. Overall, the SEBS derived MODIS Aqua estimates compared relatively favourably with the *in-situ* measurements. The aggregated 8-day ET_{Terra} and ET_{Aqua} generally overestimated ET_a , whilst $ET_{MOD16A2}$ tends to underestimate ET_a during summer months when compared to *in-situ* ET_a . The degree of overestimation of $ET_{MOD16A2}$ was lower than the aggregated ET_{Terra} and ET_{Aqua} estimates. The SEBS results and the MOD16 product emphasized the importance of the satellite overpass times and the limitations that are observed in the SEBS model. The MOD16 product and satellite-based ET models can be used to assist in decision making and can provide long-term data records over remote areas.

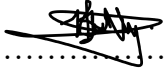
DECLARATION- PLAGIARISM

I, Sameera Khan declare that:

- (i) The research reported in this dissertation, except where otherwise indicated, is my original work.
- (ii) This dissertation has not been submitted for any degree or examination at any other university.
- (iii) This dissertation does not contain other persons' data, pictures, graphs or other information, unless specifically acknowledged as being sourced from other persons.
- (iv) This dissertation does not contain other persons' writing, unless specifically acknowledged as being sourced from other researchers. Where other written sources have been quoted, then:
 - (a) their words have been re-written but the general information attributed to them has been referenced;
 - (b) where their exact words have been used, their writing has been placed inside quotation marks, and referenced.
- (v) Where I have reproduced a publication of which I am an author, co-author or editor, I have indicated in detail which part of the publication was actually written by myself alone and have fully referenced such publications.
- (vi) This dissertation does not contain text, graphics or tables copied and pasted from the Internet, unless specifically acknowledged, and the source being detailed in the Dissertation and in the Reference sections.

Signed:

Sameera Khan

Supervisor:

Ms KT Chetty

PREFACE

The work described in this dissertation was carried out in the Centre for Water Resources Research, School of Agricultural, Earth and Environmental Sciences, University of KwaZulu-Natal, Pietermaritzburg, under the supervision of Ms KT Chetty and Dr S Gokool.

The research represents original work by the author and has not otherwise been submitted in any form for any degree or diploma to any tertiary institution. Where use has been made of the work of others it is duly acknowledged in the text.

The financial assistance of the National Research Foundation (NRF) towards this research is acknowledged. Opinions expressed in this dissertation and the conclusions arrived at, are those of the author, and are not necessarily to be attributed to the National Research Foundation.

The financial assistance of the South African National Space Agency (SANSA) towards this research is acknowledged.

ACKNOWLEDGEMENTS

All praise is due to the Almighty for blessing me with the opportunity to complete my studies and for allowing me to accomplish things that I had always believed were out of my reach. The following Masters Research Project titled “**Evaluating the influence of the land surface and air temperature gradient on terrestrial flux estimates derived using satellite earth observation data**” has been funded by the South African National Space Agency (SANSA) and the National Research Foundation (NRF). I wish to thank the aforementioned institutions for the funding received towards this project. I would also like to thank the following people and institutions:

- My sincere gratitude to Ms KT Chetty, my supervisor; for the guidance, continuous support and valuable time throughout the duration of the project.
- I am extremely thankful to Dr S Gokool, my co-supervisor, for his assistance and direction, patience, persistent support and time towards the completion of this project. Thank you for constantly being there to look into my methods and assist whenever guidance was required. I will forever be grateful to you for increasing my knowledge and making me a better person.
- I would like to acknowledge the Council for Scientific and Industrial Research (CSIR) for the provision of observed field data.
- I would like to acknowledge the South African National Space Agency (SANSA) for the funding received in the second year of my masters.
- I would like to acknowledge the National Research Foundation (NRF) for the funding received in the first year of my masters.
- I would like to thank my parents and brother for their continuous support and understanding, and the opportunity for allowing me to further my studies. I would also like to thank my extended family for supporting me in my endeavours.
- My family, thank you for the constant love, support and motivation.
- Thank you to my colleagues for the help and support provided throughout the year.
- The academic and administrative staff in the Hydrology department for making my postgraduate experience memorable.

TABLE OF CONTENTS

	Page
1. INTRODUCTION	1
1.1 Background and Significance	1
1.2 Rationale	2
1.3 Aims and Objectives	4
1.4 Research Questions	4
1.5 Research Hypotheses	4
1.6 Organisation of Dissertation	4
2. LITERATURE REVIEW	6
2.1 Conventional Methods of Estimating Actual Evapotranspiration	6
2.1.1 The surface renewal method.....	6
2.1.2 Scintillometry	7
2.1.3 The eddy covariance method.....	8
2.2 Satellite Earth Observation Methods to Estimate Actual Evapotranspiration	10
2.3 SEBS Formulation	13
2.3.1 Case studies on the application of the SEBS model.....	17
2.3.2 Limitations of satellite earth observation techniques and the SEBS model	20
2.3.3 Influence of the land surface and air temperature gradient derived using satellite earth observation data	20
2.4 Satellite Earth Observation Evapotranspiration Products.....	22

2.5	MOD16 Product to Estimate Actual Evapotranspiration	24
2.5.1	The MOD16 algorithm	24
2.5.2	Case studies on the use of the MOD16 product	33
2.6	Synthesis of Literature	36
3.	METHODOLOGY	38
3.1	General Methodology	38
3.2	Description of the Study Sites	40
3.3	Meteorological Data Acquisition for the SEBS Model	42
3.4	Satellite Data Acquisition as an Input into the SEBS Model	43
3.4.1	The pre-processing of MODIS Terra and Aqua satellite imagery	44
3.5	Acquisition of The MOD16 Product	47
3.6	Statistical Metrics Used in the Study	48
4.	RESULTS AND DISCUSSION	50
4.1	Terrestrial Flux Estimates at the Riparian Site	50
4.1.1	Net radiation	50
4.1.2	Soil heat flux	53
4.1.3	Sensible heat flux	56
4.1.4	Latent heat flux	60
4.2	Analysis of the Actual Evapotranspiration Estimates	63
4.2.1	Evaluation of the MOD16 product and the aggregated SEBS derived ET_a estimates	71
5.	CONCLUSION AND RECOMMENDATIONS	78

5.1	Conclusion	78
5.2	Recommendations.....	82
6.	REFERENCES	85
7.	APPENDICES	102
7.1	Appendix A.....	102

LIST OF FIGURES

	Page
Figure 2.1 Estimation of actual evapotranspiration and flux estimates using the SEBS model (Szporak-Wasilewska <i>et al.</i> , 2013)	12
Figure 2.2 Flow diagram of the old MOD16 algorithm (Mu <i>et al.</i> , 2007)	26
Figure 2.3 Flow diagram of the improved MOD16 algorithm (Mu <i>et al.</i> , 2011)	26
Figure 3.1 Graphical illustration of the methodology that was adopted in this study	40
Figure 3.2 Location of the study sites within the Letaba Catchment, Limpopo Province, South Africa	42
Figure 4.1 A time series comparison of Rn_{Terra} estimates obtained from implementing the SEBS model and observed data at the riparian region	52
Figure 4.2 A time series comparison of Rn_{Aqua} estimates obtained from implementing the SEBS model and observed data at the riparian region	52
Figure 4.3 A time series comparison of GO_{Terra} estimates obtained from implementing the SEBS model and observed data at the riparian region	55
Figure 4.4 A time series comparison of GO_{Aqua} estimates obtained from implementing the SEBS model and observed data at the riparian region	55
Figure 4.5 A time series comparison of H_{Terra} estimates obtained from implementing the SEBS model and observed data at the riparian region	58
Figure 4.6 A time series comparison of H_{Aqua} estimates obtained from implementing the SEBS model and observed data at the riparian region	58
Figure 4.7 A time series comparison of observed and simulated H values during the 2015 measurement period, where the observed data is the <i>in-situ</i> H value at the instantaneous overpass time	59
Figure 4.8 A time series comparison of LE_{Terra} estimates obtained from implementing the SEBS model and observed data at the riparian region	62

Figure 4.9 A time series comparison of LE_{Aqua} estimates obtained from implementing the SEBS model and observed data at the riparian region.....	62
Figure 4.10 A comparison of ET_a estimates obtained from implementing the SEBS model and observed data at the riparian region	64
Figure 4.11 A time series comparison of ET_a estimates obtained from implementing the SEBS model and observed data at the riparian region.....	65
Figure 4.12 Simulated ET_a estimates obtained within an acceptable accuracy range (AAR) of $\pm 30\%$	66
Figure 4.13 A comparison of ET_a estimates obtained from implementing the SEBS model and <i>in-situ</i> data at the savanna region	68
Figure 4.14 A time series comparison of ET_a estimates obtained from implementing the SEBS model and observed data at the savanna region	68
Figure 4.15 A time series comparison of aggregated 8-day ET_a estimates obtained from implementing the SEBS model and <i>in-situ</i> data at the riparian region.....	73
Figure 4.16 A comparison of the MOD16 product and the aggregated 8-day ET_a estimates obtained from implementing the SEBS model for 26 June 2015	74
Figure 4.17 A time series comparison of aggregated 8-day ET_a estimates obtained from implementing the SEBS model and <i>in-situ</i> data at the savanna region	75
Figure 7.1 Sample of the code used to extract ET_a data from the MOD16A2 product for the Malopeni (savanna) study site.....	102
Figure 7.2 The script used to export an image into a GeoTiff format	103

LIST OF TABLES

	Page
Table 2.1 Satellite Earth Observation (SEO) methods based on the parameterisation of the shortened energy balance equation	11
Table 2.2 Case studies on the application of the SEBS model	18
Table 2.3 Satellite earth observation ET_a products	23
Table 2.4 Case studies on the application of the MOD16 and MOD16A2 product	34
Table 3.1 Description of the MODIS Terra and Aqua imagery used in the SEBS model.....	45
Table 3.2 Bands that are extracted and utilised in ILWIS (adapted from Su and Wang, 2013)	46
Table 4.1 Validation of Rn estimates obtained from implementing the SEBS model within the riparian region	51
Table 4.2 Validation of Go estimates obtained from implementing the SEBS model within the riparian region	54
Table 4.3 Validation of H estimates obtained from implementing the SEBS model within the riparian region	57
Table 4.4 Validation of LE estimates obtained from implementing the SEBS model within the riparian region	61
Table 4.5 Validation of ET_a estimates obtained from implementing the SEBS model within the riparian region	64
Table 4.6 Validation of ET_a estimates obtained from implementing the SEBS model within the savanna region	67
Table 4.7 Validation of aggregated 8-day ET_a estimates obtained from implementing the SEBS model within the riparian region	72

Table 4.8 A comparison of derived ET_a estimates from various spatial resolutions for Site 1 for 26 June 2015.....	73
Table 4.9 Validation of aggregated 8-day ET_a estimates obtained from implementing the SEBS model within the savanna region.....	75

LIST OF SYMBOLS AND ACRONYMS

a	Air temperature ramp amplitude (°C)
A	Available energy partitioned between H , LE and G on the land surface
A_c	Available energy at the canopy level
btm_{31}	Brightness temperature (K)
C_1	Blackbody constants
C_d	Drag coefficient of foliage elements (presumed value of 0.2)
C_L	Mean potential stomatal conductance per unit leaf area ($\text{mmol. m}^{-2} \cdot \text{s}^{-1}$)
C_p	Specific heat capacity of air at constant pressure ($\text{J. Kg}^{-1} \cdot \text{K}^{-1}$)
C_t	Heat transfer coefficient of the leaf
C_t^*	Heat transfer coefficient of the soil
d_o	Displacement height (m)
e_a	Actual vapour pressure of the air (hPa)
VPD	Vapour Pressure Deficit (kPa)
e_{sat}	Saturated vapour pressure (hPa)
ε_s	Surface emissivity and is assumed to be 0.97
ε_a	Atmospheric emissivity
f_c	Fractional vegetative cover
f_s	Complement to the fractional vegetation cover (dimensionless)
g	Acceleration due to gravity (m. s^{-2})
G	Soil heat flux (W. m^{-2})
G_o	Soil heat flux (W. m^{-2})
gl_{sh}	Leaf conductance to sensible heat per unit LAI (m. s^{-1})

gl_{e_wv}	Leaf conductance to evaporated water vapour per unit LAI (m. s ⁻¹)
G_s^I	Daytime and night-time stomatal conductance (m. s ⁻¹)
G_{cu}	Leaf cuticular conductance (m. s ⁻¹)
g_{cu}	Cuticular conductance per unit LAI (0 m. s ⁻¹ for all biomes)
G_s^2	Leaf boundary-layer conductance
g_{sh}	Leaf conductance to sensible heat per unit LAI (m. s ⁻¹)
G_{STD}	Standard gravitational acceleration (9.81 m. s ⁻²)
H	Sensible heat flux (W. m ⁻²)
H_{wet}	Sensible heat flux at the wet limit (W. m ⁻²)
H_{dry}	Sensible heat flux at the dry limit (W. m ⁻²)
h_s	Roughness height of the soil (m)
H_{SR}	Sensible heat flux density (W. m ⁻²)
k	von Karman's constant of 0.4
kB^{-1}	Inverse Stanton number (dimensionless)
$KB^{-1}s$	Inverse Stanton number for bare soils (dimensionless)
L	Monin-Obukhov length (m)
l	Increasing or decreasing air temperature ramp (s).
LE_{SR}	Latent heat flux density (W. m ⁻²)
LR_{STD}	Standard temperature lapse rate (constant value of 0.0065 K. m ⁻¹)
$m(T_{min})$	Multiplier that limits potential stomatal conductance by minimum air temperatures
n	Within canopy wind profile extinction coefficient
N	Number of sides of the leaf that is part of the heat transfer process
P_a	Atmospheric pressure (Pa)

Pr	Prandtl number
P_{STD}	Standard pressure at 0 m elevation (101325 Pa)
R^2	Coefficient of determination
r_a	Aerodynamic resistance to water vapour diffusing into the atmospheric boundary layer (s. m ⁻¹)
r_{corr}	Correction for atmospheric temperature and pressure
Re^*	Roughness Reynolds number
r_e	External resistance (s. m ⁻¹)
r_{hc}	Wet canopy resistance to sensible heat (s. m ⁻¹)
r_i	External resistance (s. m ⁻¹)
RL_{wd}	Incoming longwave thermal wavelength (W. m ⁻²)
R_n	Net radiation (W. m ⁻²)
R_{n24}	Daily net radiation (W. m ⁻²)
R_{net}	Net incoming solar radiation (W. m ⁻²)
RR	Gas law constant (8.3143 m ³ . Pa. mol ⁻¹ . K ⁻¹)
rrc	Resistance to radiative heat transfer through air (s. m ⁻¹)
r_s	Surface resistance to water vapour transfer (s. m ⁻¹)
R_s	Downward shortwave radiation (W. m ⁻²)
RS_{wd}	Incoming solar radiation (W. m ⁻²)
rvc	Wet canopy resistance (s. m ⁻¹)
s_l	Quiescent ramp period (s)
T_{avg}	Daily average air temperature (°C)
T_{day}	Average of the daytime air temperature (°C)
T_{night}	Average night-time air temperature (°C)

T'	Air temperature (°C)
T_c	Brightness temperature from a central wavelength (K)
T_o	Surface temperature (K)
T_i	Average daytime or night-time in °C
$T_{ann\ avg}$	Annual average daily temperature (°C)
$T_{min\ close}$	Threshold value below which the stomata will close completely, and plant transpiration will cease (°C)
T_{STD}	Standard room temperature at 0 m elevation (288.15 K)
u	Wind speed (m. s ⁻¹)
u_*	Friction-velocity (m. s ⁻¹)
$u(h)$	Horizontal wind speed at the top of the canopy (m. s ⁻¹)
ν	Kinematic viscosity of the air
α_1	Coefficient of calibration
ρ	Air density (Kg. m ⁻³)
ω'	Vertical wind speed (m. s ⁻¹)
σ	Stefan-Boltzman constant (5.670 x 10 ⁻⁸ W. m ⁻² . K ⁻⁴)
Γ_c	0.05 for a completely covered vegetated canopy (Monteith, 1973)
Γ_s	0.315 for a bare surface (Kustas and Daughtry, 1990)
z	Height above the surface (m)
Z_{om}	Roughness height for momentum transfer (m)
Z_{oh}	Scalar roughness height for heat transfer (m)
Ψ_m	Stability correction function for momentum (m)
Ψ_h	Stability correction function for sensible heat transfer (m)
θ_o	Potential temperature at the surface (K)

θ_a	Potential temperature at height z (K)
θ_v	Virtual temperature near the surface (K)
p_o	Ambient pressure at 101.3 kPa
Λ_r	Relative evaporation
Δ	Rate of change of saturated vapour pressure with temperature (hPa. K ⁻¹)
γ	psychometric constant (kPa. K ⁻¹)
Λ	Evaporative fraction
Λ_o^{24}	Daily evaporative fraction
λ	Latent heat of vaporization (J. kg ⁻¹)
ρ_w	Density of water (Kg. m ⁻³)
λET	Latent heat flux (W. m ⁻²)
λE_{soil}	Actual soil evaporation (W. m ⁻²)
λE_{soil_pot}	Potential soil evaporation (W. m ⁻²)
λE_{wet_c}	Evaporation from the wet canopy surface (W. m ⁻²)
λE_{trans}	Transpiration from the dry canopy surface (W. m ⁻²)
λ_c	Sensors central wavelength (μ m)

LIST OF ABBREVIATIONS

BLS	Boundary Layer Scintillometer
CWSI	Crop Water Stress Index
DEM	Digital Elevation Model
DN	Digital Number
E_{daily}	Daily total evaporation
EC	Eddy Covariance
EC_{ET}	Observed Eddy Covariance Evapotranspiration
EF	Evaporative Fraction
EOS	Earth Observing System
ET_a	Actual evapotranspiration
ET_{Aqua}	SEBS derived MODIS Aqua evapotranspiration estimate
$ET_{in-situ}$	Observed <i>in-situ</i> ET_a estimate
ET_{Terra}	SEBS derived MODIS Terra evapotranspiration estimate
FPAR	Fraction of Photosynthetically Active Radiation
Go_{Aqua}	SEBS derived MODIS Aqua soil heat flux estimate
Go_{Terra}	SEBS derived MODIS Terra soil heat flux estimate
GEE	Google Earth Engine
GIS	Geographic Information Systems
GLEAM	Global Land Evaporation Amsterdam Model
H_{Aqua}	SEBS derived MODIS Aqua sensible heat flux estimate
H_{Terra}	SEBS derived MODIS Terra sensible heat flux estimate
ILWIS	Integrated Land and Water Information System

IRGA	Infrared Gas Analyser
IT	Information Technology
LAI	Leaf Area Index
LAS	Large Aperture Scintillometer
LE_{Aqua}	SEBS derived MODIS Aqua latent heat flux estimate
LE_{Terra}	SEBS derived MODIS Terra latent heat flux estimate
LSA-SAF	Land Surface Analysis Satellite Applications Facility
LST	Land Surface Temperature
MAD	Mean Absolute Difference
MAP	Mean Annual Precipitation
MAR	Mean Annual Runoff
MAT	Mean Annual Temperature
METRIC	Mapping Evapotranspiration with High Resolution and Internalised Calibration
MOD17 GPP/NPP	MODIS global terrestrial gross and net primary production
MODIS	Moderate Resolution Imaging Spectroradiometer
MOST	Monin-Obukhov Similarity Theory
NDVI	Normalised Difference Vegetation Index
OLI	Operational Land Imager
OPEC	Open Path Eddy Covariance
RH	Relative Humidity
RMSE	Root Mean Square Error
Rn_{Aqua}	SEBS derived MODIS Aqua net radiation estimate

Rn_{Terra}	SEBS derived MODIS Terra net radiation estimate
RS-PM	Revised algorithm based on the Penman-Monteith equation
RVE	Relative Volume Error
SEBAL	Surface Energy Balance Algorithm for Land
SEBI	Surface Energy Balance Index
SEBS	Surface Energy Balance System
SI	Simplified Integer
SLS	Surface Layer Scintillometer
SMAC	Simplified Model for Atmospheric Correction
TOA	Top of Atmosphere
WRC	Water Research Commission
XLAS	Extra-Large Aperture Scintillometer

1. INTRODUCTION

1.1 Background and Significance

South Africa is considered as a semi-arid and water-scarce country (Percival and Homer-Dixon, 1998; Jarman *et al.*, 2009; Ramoelo *et al.*, 2014), and global climate change has placed further strain on our limited water resources (Doll *et al.*, 2003). Approximately 25% of the Earth's surface is occupied by semi-arid and arid environments (Li *et al.*, 2019). Fensholt *et al.* (2012) states that these environments are characterised by sparse vegetation, limited water availability and fragile ecosystems. More than 90% of the annual rainfall in these regions, returns to the atmosphere as actual evapotranspiration (Wilcox *et al.*, 2003; Garcia *et al.*, 2013). Actual evapotranspiration (ET_a) is defined as the water that is transpired from the stomata of plants and lost from the upper layers of the soil (Thornthwaite, 1948; Allen *et al.*, 1998; Denis, 2013; Gu *et al.*, 2017; Running *et al.*, 2017). Ramoelo *et al.* (2014) states that large quantities of precipitation are lost as a result of ET_a . It is imperative for us to understand this particular process of the hydrological cycle in greater detail, as it directly influences water resources management decisions.

Accurate estimates and measurements of ET_a are required for, *inter alia*, drought monitoring, water resources allocation, agricultural water management and climatic applications (Timmermans *et al.*, 2013; Ramoelo *et al.*, 2014; Ke *et al.*, 2016; Gu *et al.*, 2017). Actual evapotranspiration is one of the most challenging processes of the hydrological cycle to determine accurately, especially in arid and semi-arid regions, as there is a decline and limited access of monitoring hydrological variables in these regions (Wheater *et al.*, 2007; Jovanovic *et al.*, 2015).

Numerous approaches have been established and recognised to quantify ET_a at various spatial and temporal scales. The advancements of these techniques and tools assists decision makers on the sustainable management, use and planning of water resources (Ramoelo *et al.*, 2014). Micro-meteorological methods are amongst the most frequently applied approaches to estimate ET_a (Jarman *et al.*, 2009). These methods are used to acquire point or line averaged ET_a estimates, allowing for the validation and calibration of several ET_a models, which are used to assist in water resources management and decision making. However, whilst these techniques have demonstrated to be vital in increasing our understanding of water and energy fluxes, they

are unable to provide representative large-scale ET_a estimates (Spittlehouse and Black, 1980; Courault *et al.*, 2005; Li *et al.*, 2009).

Satellite earth observation (SEO) methods have been utilised as an alternative to conventional methods to estimate ET_a , as the remotely sensed data has sufficiently longer data records compared to *in-situ* measurements, are easily accessible and provide inexpensive access to spatially representative data, at near-real time (Courault *et al.*, 2005; Xue and Su, 2017; Indirabai *et al.*, 2019). Montanari *et al.* (2013) states that remotely sensed data has the capacity to transform hydrological modelling approaches, especially in areas where meteorological networks and monitoring is sparse.

1.2 Rationale

Multiple approaches have been established to quantify ET_a using SEO data. Jarman *et al.* (2009) states, that the methods based on the parameterisation of the shortened energy balance equation are often applied, with the most frequently utilised selections including; the Surface Energy Balance Index (SEBI) (Menenti and Choudhury, 1993), the Surface Energy Balance Algorithm for Land (SEBAL) (Bastiaanssen *et al.*, 1998), the Surface Energy Balance System (SEBS) (Su, 2002), Mapping Evapotranspiration with High Resolution and Internalised Calibration (METRIC) (Allen *et al.*, 2007) and ETLOOK (Pelgrum *et al.*, 2010).

Although satellite-based ET models generally provide fairly reliable estimates of terrestrial fluxes and ET_a , these models have the tendency to perform poorly in water stressed environments due to an inherent limitation in their conceptualisation, which relates to the temperature gradient ($T_o - T_a$). The temperature gradient ($T_o - T_a$) can be defined as, the difference between the land surface (T_o) and air temperature (T_a). As a result of the diverse meteorological conditions and the differences in $T_o - T_a$ due to the differential heating of the land surface and air, variations and uncertainties are observed within the simulated and *in-situ* terrestrial flux estimates as a lag effect occurs (Gibson, 2013; Brenner *et al.*, 2017). Therefore, indicating the importance of the time of day of image acquisition and the choice of satellite sensor (MODIS Terra or Aqua) being utilised, to estimate ET_a and terrestrial flux estimates.

Considering the aforementioned limitations as a point of departure, the study aimed to establish whether the selection of an image based upon the satellite overpass time influences the accuracy of the modelled flux and ET_a estimates, as this is closely linked to the dynamic nature of $T_o - T_a$. Therefore, a model was implemented using satellite-derived input variables derived

from MODIS Terra and Aqua imagery, respectively. These imageries were utilised, as they are freely available and are obtained at different times during the day. The simulated fluxes and ET_a were compared against *in-situ* data to quantify the influence of T_o-T_a on the modelled variables.

The temperature gradient influences the latent heat flux (LE), net radiation (Rn), soil heat flux (Go) and sensible heat flux (H), which are components of the energy balance equation. Increased LE estimates result from a high land surface temperature (LST) and reduced relative humidity (Roxy *et al.*, 2014). The latent heat flux (LE) is a function of available energy (climatic variables), soil moisture and vegetation characteristics. As SEBS does not calculate LE as the energy balance residual, but using the Evaporative Fraction (EF), this results in an increased LE . The difference between the roughness height for momentum transfer (Z_{om}) and the scalar roughness height for heat transfer (Z_{oh}) is described by the kB^{-1} factor. Earlier studies have stated uncertain characterisation of the kB^{-1} factor in water stressed and in sparse vegetation cover environments. The underestimation of H possibly occurs as a result of the overestimation of the kB^{-1} factor at low Leaf Area Indices (LAIs) (Chirouze *et al.*, 2014). Overestimating the kB^{-1} factor in these environmental conditions would result in an overestimation of Z_{oh} , therefore underestimating H and subsequently overestimating ET_a .

In arid and semi-arid regions, the overestimation of ET_a usually arises when water availability limits ET_a (Li *et al.*, 2015). Therefore, by modifying the kB^{-1} value and introducing soil moisture corrections, the limitations of the overestimation of ET_a using satellite-based ET_a models, particularly in water stressed environments can be adjusted (Li *et al.*, 2015). The kB^{-1} factor can correct the differences between radiometric and atmospheric temperature and is influenced by numerous variables that relate to structural parameters and environmental conditions. Consequently, this method is utilised to correct the underestimation of sensible heat flux (H) proposed by Gokmen *et al.* (2012) to avoid the overestimation of LE and EF .

To supplement these investigations, the MOD16A2 ET_a product was acquired and evaluated. Since the MOD16 algorithm does not utilise T_o-T_a during the estimation of ET_a , the use of the MOD16A2 product provides an ideal opportunity to further gauge the influence the satellite-based energy balance ET_a model conceptualisation has on the accuracy of the terrestrial flux estimates.

1.3 Aims and Objectives

The aim of this study is to evaluate the influence which the land surface (T_o) and air temperature (T_a) gradient has on terrestrial fluxes and ET_a estimates.

The following objectives have been formulated, to fulfil the aims of this study:

- i. To evaluate the accuracy of satellite-derived ET_a and terrestrial flux estimates against *in-situ* measurements.
- ii. To implement a satellite-based ET_a model to estimate ET_a and terrestrial fluxes.
- iii. Establish the influence of the land surface and air temperature gradient on ET_a and terrestrial flux estimates through comparisons against *in-situ* measurements, as well as the MOD16 derived ET_a .

1.4 Research Questions

- i. How significant is the influence of the land surface and air temperature gradient on the accuracy of satellite-derived terrestrial fluxes and ET_a estimates?
- ii. Does the MOD16 product produce more reliable estimates of ET_a , since it is not influenced by land surface temperature?

1.5 Research Hypotheses

The null hypothesis (H_o) and alternate hypothesis (H_a) are stated as follows:

- i. H_o : The gradient between land surface and air temperature does not significantly influence the accuracy of satellite-derived ET_a and terrestrial flux estimates.
- ii. H_a : The gradient between land surface and air temperature significantly influences the accuracy of satellite-derived ET_a and terrestrial flux estimates.

1.6 Organisation of Dissertation

This dissertation comprises of five chapters, beginning with the introduction in chapter one, and ending with the conclusion and recommendations in Chapter 5. An outline of the dissertation is presented as follows:

Chapter 2 includes the literature review on the use of satellite observed methods to estimate ET_a . An explanation of the SEBS formulation and the MOD16 product formulation is provided,

to describe the process in estimating ET_a and terrestrial flux estimates. This chapter concludes with a synthesis of the literature, which discusses research gaps that are found in the literature and lays the groundwork for the methodology. Chapter 3 contains a description of the study sites and a description of the satellite and meteorological data that are utilised in this study. A description of the processing techniques that are used to estimate ET_a and the flux estimates are also subsumed within this chapter. Chapter 4 includes the results from the applied methodology and the discussion of the results obtained. The dissertation culminates with the conclusion, limitations experienced and recommendations for future studies in Chapter 5.

2. LITERATURE REVIEW

2.1 Conventional Methods of Estimating Actual Evapotranspiration

Conventional ET_a estimation techniques have been applied to aid in data collection, water resources management and in decision making (Tsouni *et al.*, 2008; Jarmain *et al.*, 2009; Ramoelo *et al.*, 2014). Micro-meteorological methods are amongst the most widely used conventional techniques and are frequently applied to validate satellite earth observed estimates of ET_a (Jarmain *et al.*, 2009). These methods are based on the shortened surface energy balance equation, which is expressed as (Courault *et al.*, 2005; Jarmain *et al.*, 2009):

$$R_n = LE + G + H \quad (2.1)$$

where R_n is the net radiation ($W \cdot m^{-2}$), LE is the latent heat flux ($W \cdot m^{-2}$), G is the soil heat flux ($W \cdot m^{-2}$) and H is the sensible heat flux ($W \cdot m^{-2}$). Advection and stored heat, water in the vegetation and water vapour in the air are omitted (Jarmain *et al.*, 2009). The most frequently applied micro-meteorological techniques include, eddy covariance, scintillometry, the surface renewal method and the Bowen ratio. A brief description of a few of these methods is detailed in the proceeding subsections.

2.1.1 The surface renewal method

The surface renewal method is based on the ramp theory, which is based on the sweep and ejection mechanisms of air parcels, due to the change in air density (Qiu *et al.*, 1995; Snyder *et al.*, 1996; Jarmain *et al.*, 2009). The air parcel located near the vegetation surface is replaced with an air parcel (ejection), which is sweeping from above.

A net radiometer is used to measure R_n , and G is measured using soil heat flux plates. Fine-wire thermocouples are used to measure air temperature at high frequencies, usually at 8 Hz (Snyder *et al.*, 1996; Jarmain *et al.*, 2009). The fundamental aspect of this approach is to derive H , together with R_n and G estimates, to compute LE as a residual of the shortened energy balance equation (Jarmain *et al.*, 2009). The sensible heat flux density (H_{SR}) is expressed as (Jarmain *et al.*, 2009):

$$H_{SR} = \alpha_1 z \rho_a C_p \frac{a}{s_1 + l} \quad (2.2)$$

Where H_{SR} is the sensible heat flux density derived by the surface renewal method ($\text{W} \cdot \text{m}^{-2}$), α_1 is the coefficient of calibration, z is the measurement height (m), ρ_a is the air density ($\text{Kg} \cdot \text{m}^{-3}$), C_p is the specific heat capacity of air at constant pressure ($\text{J} \cdot \text{Kg}^{-1} \cdot \text{K}^{-1}$), a is the air temperature ramp amplitude ($^{\circ}\text{C}$), s_l is the quiescent ramp period and l is the increasing or decreasing air temperature ramp (s).

Subsequently, LE is calculated as the residual of the shortened energy balance equation, which is expressed as:

$$LE_{SR} = R_n - G - H_{SR} \quad (2.3)$$

The measurement height, rate of change in air temperature and the weighting factor are required to apply the surface renewal method (Qiu *et al.*, 1995; Snyder *et al.*, 1996; Jarman *et al.*, 2009; Mengistu and Savage, 2010). The weighting factor, also known as the coefficient of calibration, must be determined, *a priori*, and is dependent on thermocouple size, measurement height and the type of vegetation (Jarman *et al.*, 2009; Mengistu and Savage, 2010).

The advantages of the surface renewal method include; low cost of equipment, easy installation and low power requirements. However, the technique is limited to point-based spatial representativity of ET_a estimates, fragile sensors, and expensive data logging equipment are required to acquire high frequency air temperature measurements (Jarman *et al.*, 2009).

2.1.2 Scintillometry

The scintillometer is an optical instrument which comprises of a transmitter and a receiver that measures the intensity fluctuations of a radiation beam (Thiermann and Grassl, 1992; Jarman *et al.*, 2009; Odhiambo and Savage, 2009). The receiver is made up of a detector and a data retrieval system. Radiation intensity fluctuations are the result of the refractive scattering of small air parcels that are located along the path of the radiation beam (Jarman *et al.*, 2009; Odhiambo and Savage, 2009). The fluctuations are measured at high frequencies under weak scattering conditions.

The scintillometer method is based on the Monin-Obukhov Similarity Theory (MOST) empirical relationship, from which H is estimated (Thiermann and Grassl, 1992; Jarman *et al.*, 2009; Odhiambo and Savage, 2009). There are various types of scintillometers, such as; (a) Surface Layer Scintillometer (SLS), (b) Large Aperture Scintillometer (LAS), (c) Extra-Large

Aperture Scintillometer (XLAS) and (d) Boundary Layer Scintillometer (BLS) (Jarman *et al.*, 2009; Odhiambo and Savage, 2009). The path lengths vary for the SLS, LAS and XLAS; and range between 50 to 250 m, 0.25 to 5 km and 1 to 8 km, respectively for each scintillometer (Kohsiek *et al.*, 2002; Timmermans *et al.*, 2009).

The advantages of using a scintillometer include; its ability to acquire measurements across large geographic extents, real-time monitoring and portability of the instrumentation (Dye *et al.*, 2008; Jarman *et al.*, 2009). However, the application of this approach can be limited by; the equipment costs, accurate information on the transect elevation is required as installation above tall canopies is challenging, additional evaluations of atmospheric stability to determine the direction of sensible heat flux, and turbulent conditions as the method is based on the weak scattering of the scintillometry beam (Jarman *et al.*, 2009).

2.1.3 The eddy covariance method

The eddy covariance method is widely used to measure energy fluxes that are situated within the atmospheric boundary layer (Glenn *et al.*, 2007; Jarman *et al.*, 2009; Scott, 2010; Burba, 2013). It was developed by Brutsaert (1982), to determine ET_a , using high frequency measurements, ranging between 10 Hz to 20 Hz, of water vapour and carbon dioxide above a canopy with a large and uniform fetch. Flux measurements consist of multiple rotating eddies and are used to approximate the exchange of heat and water (Burba, 2013). A flux is defined as the measure of an object which passes through a specific region within a specified time (Burba, 2013).

The principle of the eddy covariance system is the movement of air parcels by an eddy at a certain speed. Burba (2013) states, that the atmospheric flux can be approximated if the wind speed is known, as each air parcel has a specific temperature, concentration and humidity. A 3-dimensional sonic anemometer is used to measure the vertical wind speed and air temperature, which are in turn used for the estimation of H :

$$H = \rho_a C_p \overline{\omega' T'} \quad (2.4)$$

where ρ_a is the air density (Kg. m^{-3}), C_p is the specific heat capacity of air at constant pressure ($\text{J. Kg}^{-1}. \text{K}^{-1}$), ω' is the vertical wind speed (m. s^{-1}) and T' is the air temperature ($^{\circ}\text{C}$).

The eddy covariance system can be applied indirectly to determine LE as a residual of the shortened energy balance equation, or directly using an Infrared Gas Analyser (IRGA) to determine LE (Baldocchi, 2003; Burba, 2013). Measurements of R_n are obtained using a net radiometer, whilst probes on a psychrometer are utilised to measure relative humidity and air temperature. The soil heat flux variable, G , is measured using soil heat flux plates at 8 cm beneath the ground surface (Baldocchi, 2003). The eddy covariance system is able to provide direct measurements of turbulent fluxes, and the advances in computer technology and data processing capacity has promoted the use of this system (Liang *et al.*, 2012; Zitouna-Chebbi *et al.*, 2018). However, the system is expensive, and challenges are experienced when setting up the system over tall, heterogenous tree canopies and on sloping surfaces (Monteith and Unsworth, 2013).

The estimation of LE can be expressed as (Burba and Anderson, 2007):

$$LE = \lambda \frac{\frac{Mw}{Pa}}{\rho_a} \overline{\omega' e'} \quad (2.5)$$

where ρ_a is the air density (Kg. m^{-3}), λ is the latent heat of vapourisation (J. Kg^{-1}), ω' is the vertical wind speed (m. s^{-1}), Mw is the mass of water (Kg) and Ma is the mass of air (Kg).

There are certain corrections that are critical for the eddy covariance method, and the data obtained requires strict quality control and filtering, namely, anemometer tilt correction (coordinate rotation, planar fit), spike detection and trend removal (Meyers and Baldocchi, 2005). Sensors are required to measure vertical wind speed, sonic temperature and atmospheric humidity with enough frequency response, to record the change in fluctuations that are needed in the diffusion process (Drexler *et al.*, 2004).

While the usage of the aforementioned conventional methods has proven invaluable to the measurement and monitoring of terrestrial fluxes and ET_a , the application of these approaches over large geographic extents remains challenging due to, *inter alia*, the spatial representativity of these estimates as well as the extensive labour, skilled manpower and cost implications associated with setting up these monitoring networks. Subsequently, alternative approaches have been advocated to acquire spatially representative hydrological process information over large geographic extents (Spittlehouse and Black, 1980; Courault *et al.*, 2005; Li *et al.*, 2009).

2.2 Satellite Earth Observation Methods to Estimate Actual Evapotranspiration

Satellite earth observation (SEO) methods have been identified as a suitable alternative to conventional approaches to acquire spatially representative hydrological process information over large geographic extents. It is used to measure and provide useful information regarding hydrological variables, such as precipitation, ET_a and soil moisture (Schmugge *et al.*, 2002).

The advantages of using SEO data include; sufficiently longer data records as compared to conventional methods, easily accessible and inexpensive spatially representative data, at near-real time (Courault *et al.*, 2005; Xue and Su, 2017; Indirabai *et al.*, 2019). Furthermore, the use of SEO technologies can be used to provide data for remote and data scarce regions, thereby allowing for improved hydrological decision making.

The use of SEO technologies and associated data sets have frequently been applied for the estimation of ET_a (Stancalie *et al.*, 2010; Hollman *et al.*, 2013; McCabe *et al.*, 2019; Running *et al.*, 2019). These methods can broadly be categorised as; empirical methods, deterministic methods, vegetation index methods and parameterisation of the shortened energy balance equation (Courault *et al.*, 2005).

The empirical method uses SEO data as an input into empirical models (Courault *et al.*, 2005). This method is usually used to map ET_a over large geographic areas, which is based on surface temperature (Jensen, 1967; Courault *et al.*, 2005; Bicalho *et al.*, 2016). Deterministic (indirect) methods make use of complex models to estimate various elements of the energy budget (Courault *et al.*, 2005). This method makes use of SEO data and aims to obtain the required parameters to estimate ET_a (Courault *et al.*, 2005; Zhao *et al.*, 2013; Song *et al.*, 2019). Vegetation index methods make use of a SEO derived reduction factor to estimate ET_a (Courault *et al.*, 2005). This is used in combination with a reference evaporation, to estimate ET_a (Courault *et al.*, 2005; Glenn *et al.*, 2010).

The methods based on the parameterisation of the shortened energy balance equation are among the most frequently applied approaches, with the most commonly utilised options being; the Surface Energy Balance Index (SEBI) (Menenti and Choudhury, 1993), the Surface Energy Balance Algorithm for Land (SEBAL) (Bastiaanssen *et al.*, 1998), the Surface Energy Balance System (SEBS) (Su, 2002), Mapping Evapotranspiration with High Resolution and Internalised Calibration (METRIC) (Allen *et al.*, 2007) and ETLOOK (Pelgrum *et al.*, 2010). A summary of the key information associated with the abovementioned techniques are seen in Table 2.1.

Table 2.1 Satellite Earth Observation (SEO) methods based on the parameterisation of the shortened energy balance equation

Method	Attributes
SEBI	<ul style="list-style-type: none"> • Is a single-source model, which was proposed by Menenti and Choudhury (1993). • Makes use of planetary boundary layer scaling. • Is an altered Crop Water Stress Index (CWSI) approach. • ET_a is derived from the evaporative fraction (EF), by estimating the difference between hot and cold pixels, also known as dry and wet pixels. • Requires <i>in-situ</i> data and is now outdated (Menenti <i>et al.</i>, 2003; Li <i>et al.</i>, 2009).
SEBAL	<ul style="list-style-type: none"> • Established by Bastiaanssen <i>et al.</i> (1998) to estimate ET_a whilst using minimum <i>in-situ</i> measurements. • Foremost assumption is that the wet and dry pixels are present in the region being studied. • Visible and near-infrared input data are required to approximate the flux components of the shortened energy balance equation. • Assumes that the EF is constant throughout the day. • Calculates energy fluxes from various land covers and no prior knowledge is needed regarding the land cover. • Is a single-source model (Bhattarai <i>et al.</i>, 2016).
METRIC	<ul style="list-style-type: none"> • Utilised for the mapping of ET_a as a residual of the surface energy balance (Allen <i>et al.</i>, 2007). • Is a derivative of SEBAL, that is less influenced by climatic measurements to estimate ET_a (Li <i>et al.</i>, 2009; Awad, 2019; Kong <i>et al.</i>, 2019). • Does not require prior knowledge of crop type (Allen <i>et al.</i>, 2007). • Uses a daily soil water balance to prove that ET_a is zero for hot pixels. • Cold pixels in an agricultural setting should have biophysical attributes similar to the alfafa reference crop. • Able to estimate ET_a in topographically complex regions (Gibson <i>et al.</i>, 2013). • Is a single-source model (Bhattarai <i>et al.</i>, 2016).
SEBS	<ul style="list-style-type: none"> • Is a single-source model (Su, 2002; Gibson <i>et al.</i>, 2013), which utilises remote sensing and meteorological data to estimate turbulent fluxes and EF. • Fairly accurately characterises the spatio-temporal dynamics in ET_a (Su <i>et al.</i>, 2005). • Open source and freely available.

The SEBS model was selected for application in this study, as it is an open source, freely available user-friendly software, which is accessible from the Integrated Land and Water Information System (ILWIS) (Gibson *et al.*, 2013).

Prior studies have highlighted the reliability of the SEBS model, which can provide relatively credible estimates of ET_a whilst making fewer assumptions when compared against other models. The SEBS model is viewed as a promising tool to assist in decision making and water resources management (Su, 2002, Gibson *et al.*, 2011; Su and Wang, 2013). Meteorological, and biophysical data are required as inputs to the SEBS model to estimate ET_a as depicted in Figure 2.1 (Su, 2002; Li *et al.*, 2009; Jarman *et al.*, 2009; Gibson, 2013). Biophysical information is obtained from remotely sensed data (Jarman *et al.*, 2009), whilst meteorological data is acquired from *in-situ* measurements. The radiation data includes; downward solar and longwave radiation, which and is measured or estimated as a model output (Su *et al.*, 2005; Li *et al.*, 2009; Gibson, 2013).

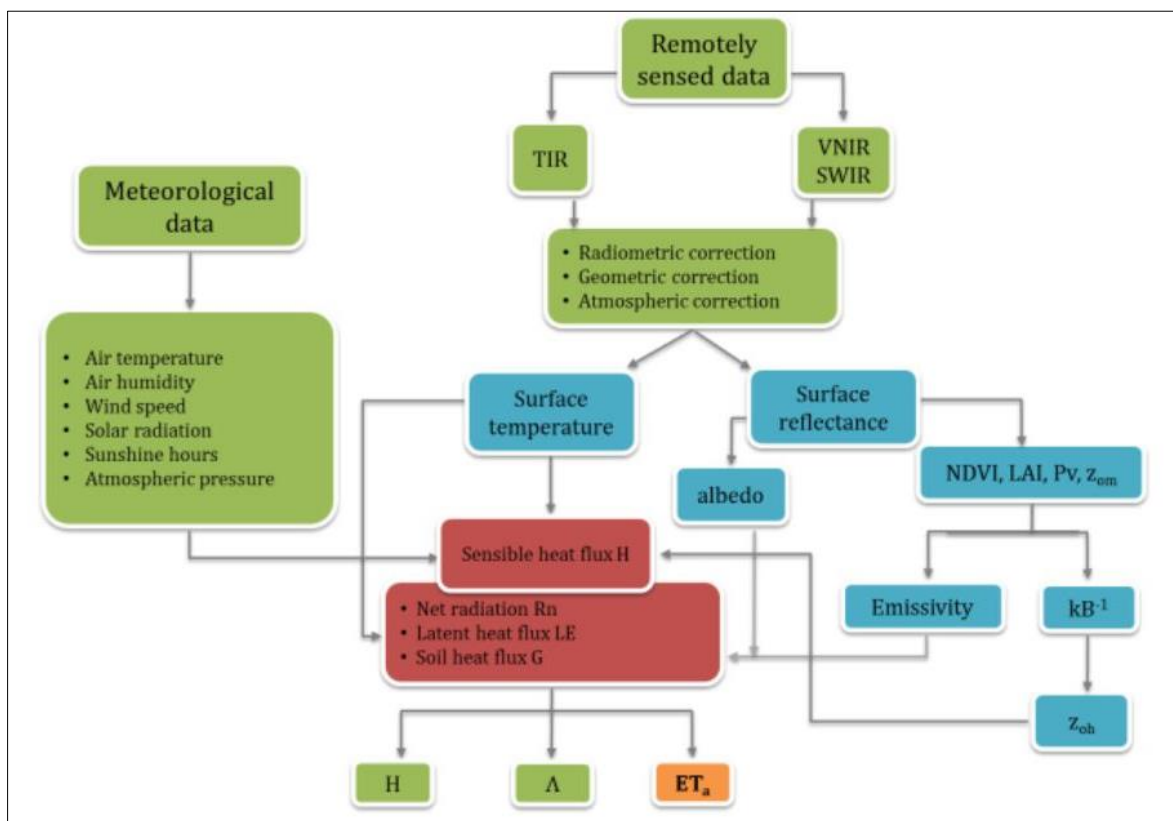


Figure 2.1 Estimation of actual evapotranspiration and flux estimates using the SEBS model (Szporak-Wasilewska *et al.*, 2013)

2.3 SEBS Formulation

The SEBS model is based on the parametrisation of the shortened energy balance equation expressed in Equation 2.1, which differentiates the available energy into H and LE (Su, 2002). The net radiation (R_n) equation is expressed in Equation 2.6 as (Su, 2002):

$$R_n = [(1 - \alpha)RS_{wd}] + [\varepsilon_a RL_{wd} - \varepsilon_s \sigma T_o^4] \quad (2.6)$$

where α is the land surface albedo, RS_{wd} is the incoming solar radiation (W. m^{-2}), ε_s is the surface emissivity, ε_a is the emissivity of the air, RL_{wd} is the incoming longwave thermal wavelength (W. m^{-2}), σ is the Stefan-Boltzman constant ($5.670 \times 10^{-8} \text{W. m}^{-2} \cdot \text{K}^{-4}$) and T_o is the surface temperature (K).

The soil heat flux equation is expressed as (Su, 2002):

$$G_o = (R_n)[\Gamma_c + (1 - f_c) \cdot (\Gamma_s - \Gamma_c)] \quad (2.7)$$

where G_o is the soil heat flux (W. m^{-2}), Γ_c is presumed to be 0.05 for a completely covered vegetated canopy (Monteith, 1973), f_c is the fractional vegetative cover and Γ_s is assumed to be 0.315 for a bare surface (Kustas and Daughtry, 1990).

The SEBS model makes use of the Monin-Obukhov Similarity Theory (MOST) in the estimation of H (Su, 2002). The H is expressed in Equations 2.8 and 2.9, and the Obukhov length is expressed in Equation 2.10 (Su, 2002):

$$u = \left(\frac{u_*}{k}\right) \times \left[\ln\left(\frac{z-d_o}{Z_{om}}\right) - \Psi_m\left(\frac{z-d_o}{L}\right) + \Psi_m\left(\frac{Z_{om}}{L}\right)\right] \quad (2.8)$$

$$\theta_o - \theta_a = \left(\frac{H}{k u_* \rho c_p}\right) \times \left[\ln\left(\frac{z-d_o}{Z_{oh}}\right) - \Psi_h\left(\frac{z-d_o}{L}\right) + \Psi_h\left(\frac{Z_{oh}}{L}\right)\right] \quad (2.9)$$

$$L = -\left(\frac{\rho c_p u_*^3 \theta_v}{k g H}\right) \quad (2.10)$$

where u is the wind velocity (m. s^{-1}), u_* is the friction velocity (m. s^{-1}), k is the von Karman's constant with a value of 0.4, z is the height above the surface (m), d_o is the displacement height (m), Z_{om} is the roughness height for momentum transfer (m), Z_{oh} is the scalar roughness height for heat transfer (m), Ψ_m is the stability correction function for momentum (m), Ψ_h is the stability correction function for sensible heat transfer (m), θ_o is the potential temperature at the

surface (K), θ_a is the potential temperature at height z (K), ρ is the air density (Kg. m^{-3}), C_p is the specific heat capacity of air at constant pressure ($\text{J. Kg}^{-1} \cdot \text{K}^{-1}$), L is the Obukhov length (m), g is the acceleration due to gravity (m. s^{-2}) and θ_v is the virtual temperature near the surface (K).

The Z_{om} can be determined using empirical relationships with NDVI (Su and Jacobs, 2001). Brutsaert (1982) states that empirical relationships are used in the estimation of vegetation height (h) and d_o , and are expressed as:

$$Z_{om} = 0.005 + 0.5 \left(\frac{NDVI}{NDVI_{max}} \right)^{2.5} \quad (2.11)$$

$$h = \frac{Z_{om}}{0.316} \quad (2.12)$$

$$d_o = \frac{2}{3} (h) \quad (2.13)$$

Aerodynamic resistance varies according to the condition of the environment at the time, as it influences sensible heat and latent heat fluxes and impacts ET_a (Sugita and Kishii, 2002). The Z_{om} and Z_{oh} are required to estimate H and are given as:

$$Z_{oh} = \frac{Z_{om}}{\exp(kB^{-1})} \quad (2.14)$$

where kB^{-1} is the inverse Stanton number, which is a dimensionless heat transfer coefficient. Su (2002) stated that the kB^{-1} value is expressed in Equation 2.15 and 2.16 as:

$$kB^{-1}_{SEBS} = (kB^{-1}_c \times fc^2) + (kB^{-1}_m \times fcfs) + (kB^{-1}_s \times fs^2) \quad (2.15)$$

$$kB^{-1} = \left[\left(\frac{kC_d}{4C_t \times \frac{u^*}{u(h)} \times \left(1 - e^{-\frac{n}{2}} \right)} \right) \times (f_c^2) \right] + \left[\left(\frac{k \times \frac{u^*}{u(h)} \times \frac{Z_{om}}{h}}{C_t^*} \right) \times (f_c^2) \times (f_s^2) \right] + \left[(kB^{-1}_s \times f_s^2) \right] \quad (2.16)$$

where C_d is presumed to have a value of 0.2 and it is the drag coefficient of foliage elements, $u(h)$ is the horizontal wind speed at the top of the canopy, n is the within canopy wind profile extinction coefficient, f_c and f_s are the fractional canopy coverage and its compliment, respectively.

C_t is the heat transfer coefficient of the leaf which for most canopies and environmental conditions is bound between $0.005N \leq C_t \leq 0.075N$, where N is the number of sides of the leaf that is part of the heat transfer process.

C_t^* is the heat transfer coefficient of the soil, and is expressed as $C_t^* = Pr^{-\frac{2}{3}} \times Re^{*\frac{1}{2}}$, where Pr is the Prandtl number and Re^* is the roughness Reynolds number and is estimated as $Re^* = \frac{h_s \times u_*}{\nu}$, h_s is the roughness height of the soil and ν is the kinematic viscosity of the air, and is expressed as (Massman, 1999), $\nu = (1.327 \times 10^{-5}) \times \left(\frac{p_o}{p}\right) \times \left(\frac{T}{T_o}\right)^{1.81}$, where p and T are the ambient pressure and temperature, and p_o is 101.3 kPa and T_o is 273.5 K, respectively.

For bare soils, the kB^{-1} value is expressed in Equation 2.17 (Brutsaert, 1982) as:

$$kB^{-1}_s = 2.46(Re^*)^{\frac{1}{4}} - \ln(7.4) \quad (2.17)$$

The actual H ranges between the sensible heat flux at the wet limit (H_{wet}) and the sensible heat flux at the dry limit (H_{dry}). At the wet limit, H possesses its minimum value, as evaporation can occur at near potential rates (Su, 2002). At the dry limit, H possesses its maximum value, and LE is zero as a result of being limited by soil moisture. Equations 2.18 and 2.19 are the equations for H_{wet} and H_{dry} is expressed as (Su, 2002):

$$H_{wet} = R_n - G_o - \lambda E_{wet} \quad (2.18)$$

$$H_{dry} = R_n - G_o \quad (2.19)$$

The relative evaporation can be expressed as (Su, 2002):

$$\Lambda_r = \left[1 - \left(\frac{H - H_{wet}}{H_{dry} - H_{wet}}\right)\right] \quad (2.20)$$

where Λ_r is the relative evaporation and H is the sensible heat flux ($W \cdot m^{-2}$).

Su (2002) combined Equation 2.18 and a combination equation similar to the Penman combination equation, to determine the EF . As stated by Menenti (1984), when the resistance terms are classified into the bulk internal and external resistances, the combination equation is expressed as:

$$\lambda E = \frac{[s \times r_e \times (R_n - G_o) + \rho C_p \times (e_{sat} - e)]}{[r_e \times (\gamma + \Delta) + \gamma \times r_i]} \quad (2.21)$$

where s is the rate of change of saturated vapour pressure with temperature ($\text{hPa} \cdot \text{K}^{-1}$), r_e is the external resistance ($\text{s} \cdot \text{m}^{-1}$), e_{sat} and e are the saturated and actual vapour pressure (hPa) respectively, γ is the psychrometric constant ($\text{hPa} \cdot \text{K}^{-1}$) and r_i is the internal resistance ($\text{s} \cdot \text{m}^{-1}$).

In Equation 2.21, it is presumed that the roughness lengths for heat and vapour transfer are equivalent (Brutsaert, 1982). Su (2002), states that the Penman-Monteith equation is only effective for a vegetated canopy, whilst Equation 2.16 is valid for a vegetated canopy and a soil surface with defined bulk surface internal resistance. The use of Equation 2.21 to determine the latent heat energy is complex, as a result of the difficulties in determining r_i as this is regulated by the accessibility of soil moisture (Su, 2002). Therefore, Su (2002) suggested an alternative to the direct use of r_i in estimating λE .

According to the definition, r_i at the wet limit is equal to zero. By including this value into Equation 2.21, and amending the variable to reflect the wet limit conditions, the sensible heat flux is expressed as (Su, 2002):

$$H_{wet} = \frac{\left[(R_n - G_o) - \frac{\rho C_p}{r_{ew}} \times \left(\frac{e_{sat} - e}{\gamma} \right) \right]}{\left[1 + \frac{\Delta}{\gamma} \right]} \quad (2.22)$$

Where r_{ew} is the external resistance, which depends on the Obukhov length (L), and is a function of the sensible heat flux and the friction velocity (Su, 2002) Equation 2.8 - Equation 2.10. The friction velocity and L , which have been previously determined are then utilised to estimate r_{ew} from Equation 2.9 as:

$$r_e = \frac{1}{ku_*} \times \left[\ln \left(\frac{z - d_o}{z_{oh}} \right) - \Psi_h \left(\frac{z - d_o}{L} \right) + \Psi_h \left(\frac{z_{oh}}{L} \right) \right] \quad (2.23)$$

The external resistance at the wet limit is expressed as (Su, 2002):

$$r_{ew} = \frac{1}{ku_*} \times \left[\ln \left(\frac{z - d_o}{z_{oh}} \right) - \Psi_h \left(\frac{z - d_o}{L_w} \right) + \Psi_h \left(\frac{z_{oh}}{L_w} \right) \right] \quad (2.24)$$

The wet limit stability length is discussed in further detail in Su (2002) and is determined as:

$$L_w = - \frac{pu_*^3}{\left[\frac{kg \times 0.61 \times (R_n - G_o)}{\lambda} \right]} \quad (2.25)$$

The evaporative fraction is expressed as (Su, 2002):

$$\Lambda = \frac{(\lambda E)}{(R_n - G)}$$

$$= \frac{(\Lambda_r)(\lambda E_{wet})}{(R_n - G)} \quad (2.26)$$

Assuming that the evaporative fraction is constant during the day, the daily actual evapotranspiration is expressed as (Su, 2002):

$$E_{daily} = (8.64 \times 10^7) \times (\Lambda_o^{24}) \times \left[\frac{(R_{n24} - G_o)}{\lambda \rho_w} \right] \quad (2.27)$$

where E_{daily} is the daily total evaporation (mm. day⁻¹), Λ_o^{24} is the daily evaporative fraction, R_{n24} is the daily net radiation (W. m⁻²), λ is the latent heat of vaporization (J. kg⁻¹) and ρ_w is the density of water (Kg. m⁻³).

2.3.1 Case studies on the application of the SEBS model

Many studies have implemented the SEBS model to estimate ET_a , and a select few relevant case studies have been presented in Table 2.2.

Table 2.2 Case studies on the application of the SEBS model

Study	Main objective	Satellite Sensor	Key findings
Su, 2002	The estimation of atmospheric turbulent fluxes and the EF , whilst using remote sensing and field data.	MODIS TERRA	<ul style="list-style-type: none"> • The SEBS model resulted in accurate outputs; however, the model is sensitive to surface roughness. • The mean error of SEBS produced estimates is approximately 20 % relative to the mean sensible heat flux, provided that the input geometrical and physical variables are reliable.
McCabe <i>et al.</i> , 2008	To utilise multi-sensor remote sensing data for water and energy cycle studies, to understand the variability and feedback of land surface and atmospheric processes.	MODIS TERRA and MODIS AQUA	<ul style="list-style-type: none"> • MODIS TERRA and MODIS AQUA data were used as inputs into the SEBS model to estimate ET_a. • Soil moisture anomalies from the AMSR-E sensor indicate that there is a significant agreement with sensible heat predictions.
Pan <i>et al.</i> , 2008	To estimate the regional scale terrestrial water cycle using remote sensing, and the use of MODIS TERRA and MODIS AQUA as inputs into the SEBS model to estimate ET_a .	MODIS TERRA and MODIS AQUA	<ul style="list-style-type: none"> • The SEBS derived ET_a values are overestimated to a greater amount than the Variable Infiltration Capacity (VIC) ET_a estimates. • Challenging to improve the results by assimilating ET_a estimated from remotely sensed data.

Study	Main objective	Satellite Sensor	Key findings
Gibson <i>et al.</i> , 2011	The use of SEBS to estimate ET_a in a heterogeneous region, and the uncertainties experienced when using a pre-packaged SEBS model.	MODIS TERRA and MODIS AQUA	<ul style="list-style-type: none"> Uncertainties were introduced due to model sensitivity, which resulted from land surface and air temperature gradients, heterogeneous vegetation, the selection of a fractional vegetation cover formula and the displacement height and height at which wind speed is estimated. The fractional vegetation cover formula influenced the total evaporation by 0.7 mm.
Lu <i>et al.</i> , 2013	To estimate the EF from MODIS TERRA and MODIS AQUA data using the SEBS model in a subtropical evergreen coniferous plantation.	MODIS TERRA and MODIS AQUA	<ul style="list-style-type: none"> The SEBS estimated EF was higher than the measured EF, resulting from the lack of energy-balance closure. The MODIS pixel size covers a larger region than the <i>in-situ</i> data, resulting in an overestimation of EF. SEBS produced Rn was overestimated and produced an RMSE of 84.8 W. m⁻². SEBS estimated G was overestimated and produced an R² of 0.042.
Gokool <i>et al.</i> , 2016	To validate satellite derived ET_a estimates against the surface renewal method, and to assess the infilling techniques that produce a time series of daily satellite derived ET_a .	MODIS TERRA	<ul style="list-style-type: none"> The SEBS ET_a estimates resulted in a R² value of 0.33 and a RMSE value of 2.19 mm. d⁻¹, when compared to <i>in-situ</i> ET_a values. The infilling techniques, the Kc_{act} and the linear interpolation method resulted in a poor correlation between the SEBS ET_a values, yielding a RMSE value of 1.96 mm. d⁻¹ and 1.54 mm. d⁻¹ respectively.

2.3.2 Limitations of satellite earth observation techniques and the SEBS model

Although SEO techniques to estimate ET_a are easily accessible, the acquisition of data does have limitations which include cloud cover, the revisit and repeat cycle of satellites, the analysis of images and human induced errors (Moran *et al.*, 1997; Gokool *et al.*, 2016). Depending on the satellite imagery being used, cloud coverage may reduce the quality of the images and the frequency at which the images are obtained, therefore resulting in an inadequate repeat coverage for applications such as intensive agricultural management among other applications (Moran *et al.*, 1997; Gokool *et al.*, 2016; Righini and Surian, 2018). Human induced errors are introduced, as humans select the data that is necessary, specify the resolution, determine the date of the image that is required and specify the processing method of the data (Righini and Surian, 2018).

Additionally, these limitations may be further compounded by model specific limitations which further propagates uncertainty into the final model output. There are multiple model specific limitations in the pre-packaged version of the SEBS model that is available in ILWIS and are discussed in Gibson *et al.* (2013). The SEBS model is sensitive to the uncertainties related to the land surface and air temperature gradient (Gibson *et al.*, 2013; Gokool *et al.*, 2016), the fractional vegetation cover formula, the displacement height and the height of wind speed measurements (Gokool *et al.*, 2016) and the diversity in topography and vegetation cover (Gibson *et al.*, 2013; Gokool *et al.*, 2016). The assumption that the EF is constant throughout the day is also considered as a limitation of the SEBS model (Su *et al.*, 2005).

2.3.3 Influence of the land surface and air temperature gradient derived using satellite earth observation data

Satellite-based ET_a estimation techniques frequently overestimate ET_a in arid and semi-arid environments, where water stress limits ET_a (Seneviratne *et al.*, 2010). One of the main restrictions of models that are based on the shortened energy balance equation include the overestimation of ET_a in water limited conditions. This occurs as a result of its inability to effectively account for soil moisture (Gokmen *et al.*, 2012; Gibson *et al.*, 2013; Yi *et al.*, 2018; Dzikiti *et al.*, 2019).

Preceding studies have stated uncertain characterisation of the kB^{-1} factor in water limited and in sparse vegetation cover environments (Gokmen *et al.*, 2012; Gibson, 2013; Paul *et al.*, 2014; Bhattarai *et al.*, 2018; Khand *et al.*, 2019). In recent years modifications to the SEBS

formulation, have been carried out to account for the influence of soil moisture during the derivation of terrestrial fluxes and ET_a , which is achieved through the integration of a stress factor to address the kB^{-1} factor (Gokmen *et al.*, 2012; Pardo *et al.*, 2014; Li *et al.*, 2015). According to Gokmen *et al.* (2012), application of the modified SEBS formulation can improve the estimation of energy and water fluxes, in water-stressed regions. Zhuang *et al.* (2016) states that the kB^{-1} factor can correct the differences between the temperature gradient ($T_o - T_a$), and it is influenced by numerous variables that relate to structural parameters and environmental conditions.

Days that have a large difference between radiometric and atmospheric temperature, may occur as a result of the $T_o - T_a$ gradient. This influences the ET_a and terrestrial flux estimates and would require a high kB^{-1} factor to moderate it (Brenner *et al.*, 2017). A decrease in the kB^{-1} factor, would result in a higher land surface and air temperature gradient, and an increased EF , resulting in an increased ET_a estimate. The land surface temperature (LST) estimate is influenced by the shortened energy balance equation, and spatially distributed ET_a estimates are based on manipulating LST information obtained from thermal infrared remote (TIR) sensing located on satellite or airborne platforms (Brenner *et al.*, 2017). As a result of the satellite overpass times, and the imagery being obtained at different times, as MODIS Terra satellite passes over the equator at 10:30 am (descending) (Muhammed, 2012), and the MODIS Aqua satellite passes over the equator at 1:30 pm (ascending) (Savtchenko *et al.*, 2004), differences in ET_a and terrestrial flux estimates may occur. This could occur as a result of the $T_o - T_a$ gradient, which influences the ET_a and terrestrial flux estimates.

When a model estimated LST is less than the air temperature, a negative H value is obtained, indicating an underestimation of the parameter. According to Lu *et al.* (2013), this arises either from stable or strong horizontal advection conditions. The underestimation of H , and the overestimation of EF , either result from; a lack of the energy balance closure, the underestimation of $R_n - G$, land types with higher ET_a in a MODIS pixel and incorrect calculation of the aerodynamic parameters (Lu *et al.*, 2013). The SEBS model is highly complex, and a combination of several minor factors may result in the overestimation of ET_a and terrestrial flux estimates. According to Kalma *et al.* (2008), the temperature gradient and LST impact LE , R_n , G_o and H , which are components of the energy balance equation. The errors related with utilising surface temperature to estimate H , include; errors in observed meteorological data, errors in model assumption and the significant inaccuracies in radiometric

temperature estimation and the inequality between the land surface and air temperature gradient (Kalma *et al.*, 2008).

Satellite earth observation data have effectively been used to estimate the spatial distribution of the available energy from combined visible and TIR data, and the spatial distribution of H from thermal data (Troufleau *et al.*, 1997). The H variable is usually related to the gradient between the land surface temperature and air temperature divided by an aerodynamic resistance. Satellites are able to provide information when ET_a estimates are needed at high spatio-temporal resolutions. However, whilst these techniques have been proven to be valuable, there still exists an influence of the land surface and air temperature gradient on ET_a and terrestrial flux estimates derived using SEO data.

2.4 Satellite Earth Observation Evapotranspiration Products

There is an increasing number of global and regional SEO products that are being developed and made available to account for ET_a (Long *et al.*, 2014; Karimi *et al.*, 2019). Usually, the level of expertise that is needed to use these data products is much lower than those essential for conducting remote sensing analysis.

The most frequently applied SEO ET_a products include; Global Land Evaporation Amsterdam Model (GLEAM) (Miralles *et al.*, 2011), Land Surface Analysis Satellite Applications Facility (LSA-SAF), MOD16 (Mu *et al.*, 2007) and MOD16A2 (Mu *et al.*, 2011). A summary of the key information of the abovementioned ET_a products are presented in Table 2.3.

Table 2.3 Satellite earth observation ET_a products

ET_a Product and Reference	Availability	Algorithm	Input Data	Temporal Resolution	Spatial Resolution	Data Source
MOD16 Mu <i>et al.</i> (2007)	2000-2010	Penman-Monteith	Land cover, albedo, LAI, air temperature, vapour pressure deficit, enhanced vegetation index.	8-day, monthly, annual	1 km	MODIS, GMAO
MOD16A2 Estimated using Mu <i>et al.</i> (2007) improved algorithm, Mu <i>et al.</i> (2011)	2000-Current	Penman-Monteith	Land cover, albedo, LAI, air temperature, vapour pressure deficit, enhanced vegetation index.	8-day	500 m	MODIS, GMAO
LSA-SAF LSA-SAF 2010 Product user manual, http://landsaf.meteo.pt/	2009-Current	Surface Energy Balance Equation	Air temperature, wind speed, dew point temperature, soil moisture, air pressure, land cover and specific humidity.	Daily	3-5 km, depending on latitude and distance to nadir view	ECMWF, ECOCLIMAP, MSG SEVIRI
GLEAM Miralles <i>et al.</i> (2011)	1984-2007	Priestley and Taylor	Air temperature, precipitation, snow water equivalents, radiation fluxes, and soil moisture and vegetation optical depth.	Daily	0.25°	CMORPH NSIDC, GEWEX SRB, TMMI+AMSR-E

The MOD16A2 product was selected for application, as it is a freely available satellite-based product that contains readily available ET_a . The MOD16A2 product utilises an algorithm that is based on the Penman-Monteith equation and comprises of daily inputs of meteorological reanalysis data and MODIS satellite products (Aguilar *et al.*, 2018). The MOD16A2 ET_a data was acquired and evaluated as part of the investigation. The rationale for this can be attributed to the absence of the temperature data used during the derivation of ET_a using the MOD16 algorithm (Mu *et al.*, 2007; Mu *et al.*, 2011), and having the finest spatial resolution from the aforementioned ET_a products. A study undertaken by Gibson *et al.* (2013), detailed the use of the SEBS model for agricultural and natural environments, and suggested the validation of current global ET_a products in South Africa and promoted their use. The validation of the MOD16 product is advantageous, as it avoids the use of thermal imagery (Gibson, 2013). This is beneficial, as the SEBS model is sensitive to $T_o - T_a$ and the uncertainties related to the T_o estimation.

2.5 MOD16 Product to Estimate Actual Evapotranspiration

Running *et al.* (2017) states that the MOD16 produced ET_a is as a result of the sum of ET_a from daytime and night. The MOD16 product has a spatial resolution of 1 km and a temporal resolution of 8-day ($\text{mm. } 8\text{d}^{-1}$), monthly and annual intervals (Running *et al.*, 2017). The 8-day ET_a value is a cumulative value of the ET_a estimates obtained (Ramoelo *et al.*, 2014). The MOD16 algorithm combines remotely sensed data on land use, land cover, albedo, Leaf Area Index (LAI) and fraction of photosynthetically active radiation ($FPAR$), with downward solar radiation (R_s), air temperature (T_a) and actual vapour pressure deficit (ea) to estimate global ET_a (Mu *et al.*, 2011).

2.5.1 The MOD16 algorithm

The satellite product used in this study was the MOD16A2 (MODIS TERRA Net Evapotranspiration 8-day Global 500 m resolution) product, which is a recently updated version of the MOD16 product (Mu *et al.*, 2013). The algorithm that was utilised for the MOD16 product was based on the Penman-Monteith equation and comprises daily inputs of meteorological reanalysis data and the MODIS satellite-derived products, such as; vegetation property dynamics, albedo and landcover (Aguilar *et al.*, 2018). The study therefore validated the MOD16A2 ET_a ($ET_{MOD16A2}$) estimates using *in-situ* data and examined if the MOD16A2

product identified and captured the variations in ET_a within the different study sites, with varying vegetation cover and land types.

The MOD16 algorithm was developed by Mu *et al.* (2007) and improved by Mu *et al.* (2011), and was based on the Penman-Monteith combination equation (Monteith, 1965; Allen *et al.*, 1998):

$$\lambda ET = \frac{sA' + \rho C_p \times \left(\frac{e_{sat} - e}{r_a} \right)}{s + \gamma \times \left(1 + \frac{r_s}{r_a} \right)} \quad (2.28)$$

Where λET is the latent heat flux, λ is the latent heat of vapourisation of water ($J. kg^{-1}$), $s = d(e_{sat})/dT$, which is the slope of the curve relating saturated water vapour pressure (e_{sat}) to temperature, e is the actual water vapour (Pa), A' is the available energy partitioned between sensible heat, latent heat and soil heat fluxes on land surface ($J. m^{-2}. s^{-1}$), ρ is air density ($kg. m^{-3}$), C_p is the specific heat capacity of air at constant pressure ($J. kg^{-1}. K^{-1}$), r_a is the aerodynamic resistance to water vapour diffusing into the atmospheric boundary layer ($s. m^{-1}$), γ is the psychometric constant ($0.066 kPa. K^{-1}$) and r_s is the surface resistance to water vapour transfer ($s. m^{-1}$) (Mu *et al.*, 2011).

Multiple improvements have been made to the MOD16 algorithm (Mu *et al.*, 2011) in relation to its preceding algorithm (Mu *et al.*, 2007), as seen in Figure 2.2 and Figure 2.3, and include:

- i. The canopy is separated into wet and dry surfaces and is able to provide water loss estimates of canopy evaporation and canopy transpiration from the wet and dry surfaces, respectively.
- ii. Day- and night-time ET_a estimates are included in the revised algorithm.
- iii. Wet surfaces and soil moisture are included, and the ground surface evaporation includes potential evaporation from the wet surface and evaporation from the moist soil.
- iv. The concern of negative ET_a and Potential Evapotranspiration (PET) values for some 8-day and monthly data has been resolved (Running *et al.*, 2017).
- v. The concern of invalid MODIS surface albedo values during the year for vegetated pixels, resulting from severe and constant cloudiness, has been resolved. An albedo value of 0.4 is specified to pixels, which is a typical value that is given to nearby rainforests with valid albedo values (Mu *et al.*, 2007; Running *et al.*, 2017).

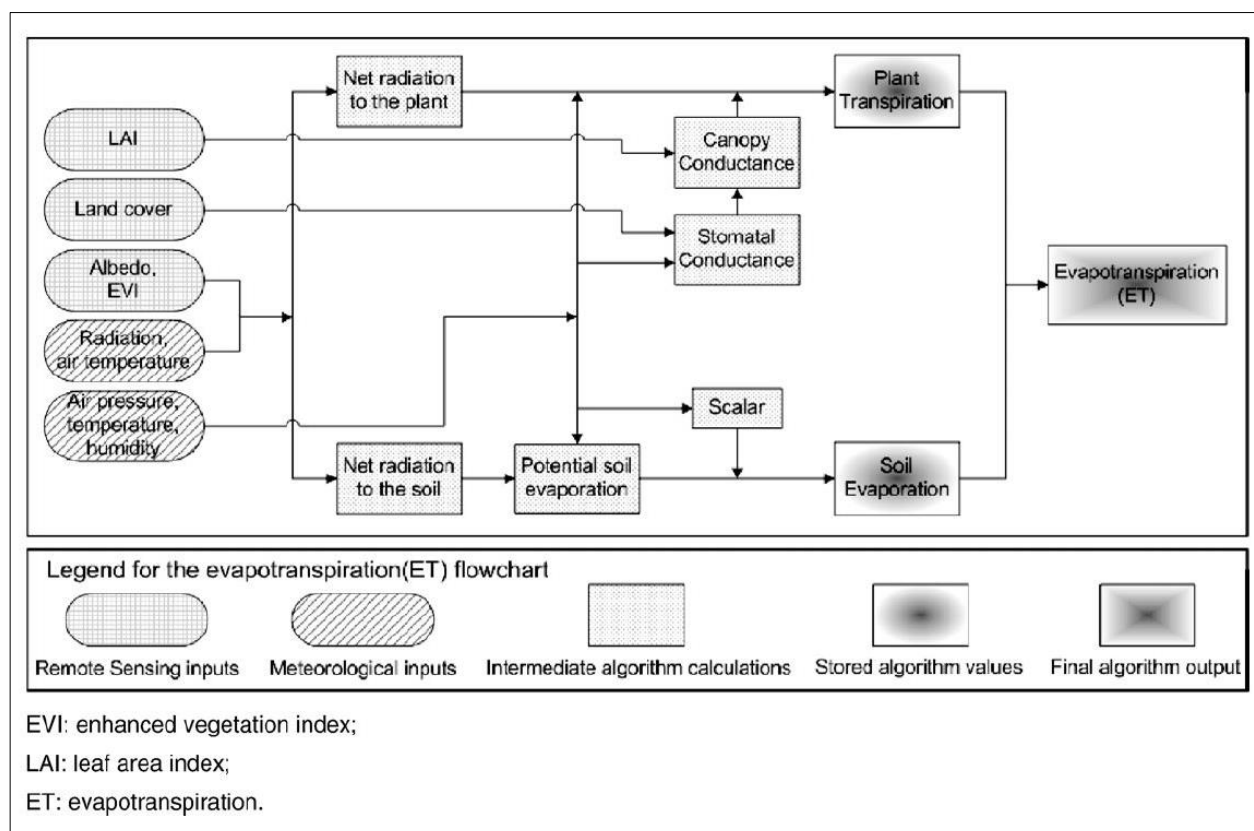


Figure 2.2 Flow diagram of the old MOD16 algorithm (Mu *et al.*, 2007)

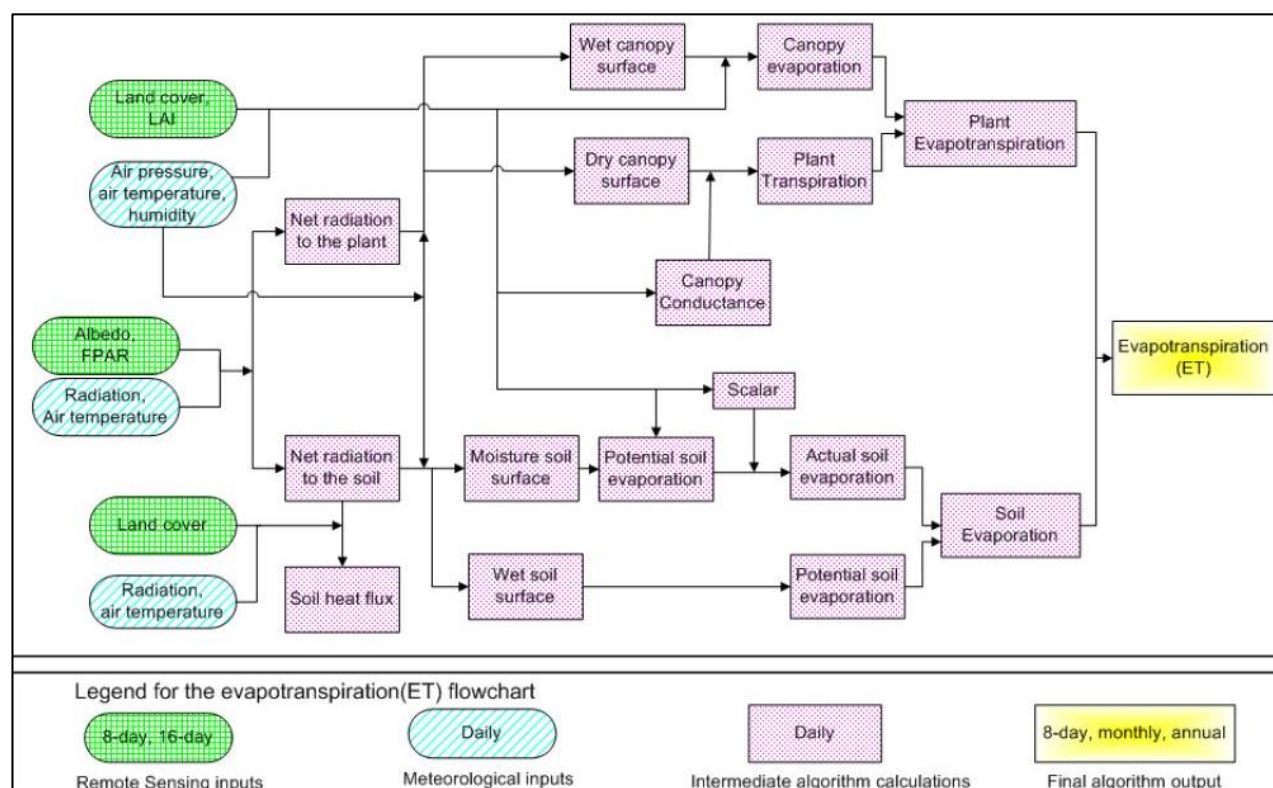


Figure 2.3 Flow diagram of the improved MOD16 algorithm (Mu *et al.*, 2011)

The MOD16 algorithm runs at a daily basis and the daily ETa is the sum of ETa from daytime and night. To acquire the average night-time air temperature (T_{night}), it is assumed that the daily average air temperature (T_{avg}) is the average of the daytime air temperature (T_{day}). Therefore, the T_{night} and T_{day} is the average air temperature when the downward solar radiation is above zero. Thus, T_{night} is expressed in Equation 2.29 as:

$$T_{night} = 2 \times T_{avg} - T_{day} \quad (2.29)$$

In the improved ET algorithm, the stomata are assumed to close fully and the plant transpiration through the stomata is zero, except for the transpiration that occurs through the leaf boundary-layer and the leaf cuticles.

The net incoming solar radiation (R_{net}) is expressed in Equations 2.30 and 2.31 as (Cleugh *et al.*, 2007):

$$R_{net} = (1 - \alpha) \times (R_{swd}) + \sigma [\varepsilon_a - \varepsilon_s] \times (273.15 + T)^4 \quad (2.30)$$

Where α is MODIS albedo, R_{swd} is the downward shortwave radiation, ε_s is the surface emissivity and is assumed to be 0.97, ε_a is the atmospheric emissivity and is expressed as $(1 - 0.26e^{-7.77 \times 10^{-4} T^2})$ and T_a is the air temperature in $^{\circ}\text{C}$.

In the preceding MOD16 algorithm, G was extracted from R_{net} to obtain the net radiation partitioned in the ET process as expressed in Equation 2.31 as:

$$A = R_{net} - G \quad (2.31)$$

Where A is the difference between the radiation partitioned on the soil surface and soil heat flux.

In the improved MOD16 algorithm, there is no soil heat flux interaction between the soil and the atmosphere, if the ground is entirely covered with vegetation. The energy that is received by the soil is the difference between the radiation partitioned on the soil surface and G , as expressed in Equations 2.32, 2.33 and 2.34 as (Mu *et al.*, 2011):

$$A = R_{net} \quad (2.32)$$

$$A_c = F_c \times A \quad (2.33)$$

$$A_{soil} = (1 - F_c) \times A - G \quad (2.34)$$

Where A_c is the part of A that is available to the canopy and A_{soil} is the part of A partitioned on the soil surface, and F_c is the vegetation cover fraction.

When the daytime and night-time temperature is low ($<5^\circ\text{C}$), there is no G . In the old MOD16 algorithm G is zero, however it is now estimated as Equation 2.35 as (Mu *et al.*, 2011):

$$G_{soil} = \begin{cases} 4.73T_i - 20.87 & T_{min\ close} \leq T_{ann\ avg} < 25^\circ\text{C}, T_{day} - T_{night} \geq 5^\circ\text{C} \\ 0 & T_{ann\ avg} \geq 25^\circ\text{C} \text{ or } T_{ann\ avg} < T_{min\ close} \text{ or } T_{day} - T_{night} \geq 5^\circ\text{C} \\ 0.39A_i & abs(G_{soil}) \times abs(A_i) \end{cases}$$

$$G = G_{soil}(1 - F_c) \quad (2.35)$$

Where G_{soil} is the soil heat flux when $F_c = 0$, T_i is the average daytime or night-time in $^\circ\text{C}$, $T_{ann\ avg}$ is the annual average daily temperature and $T_{min\ close}$ is the threshold value below which the stomata will close completely and plant transpiration will cease (Mu *et al.*, 2007; Running *et al.*, 2004).

In the old MOD16 algorithm, there was no difference between the ET on the saturated and moist bare soil surface, and there was no evaporation, however transpiration occurred on the canopy surface (Mu *et al.*, 2007). In the modified MOD16 algorithm, the water cover fraction (F_{wet}) which is taken from the Fisher *et al.* (2008) ET model, modified to be constrained to zero when the relative humidity (RH) is less than 70%:

$$F_{wet} = \begin{cases} 0.0 & RH < 70\% \\ RH^4 & 70\% \leq RH \leq 100\% \end{cases} \quad (2.36)$$

When RH is less than 70%, 0% of the surface is covered by water (Mu *et al.*, 2011). For the wet canopy and wet soil surface, the water evaporation is calculated as the potential evaporation, which is explained in further detail within the document.

Evaporation of precipitation that is intercepted by the canopy cover forms a considerable amount of upward water flux in ecosystems with large leaf area index (LAI). When the vegetation is covered with water, $F_{wet} \neq 0$, water evaporation from the vegetation surface will occur. Evapotranspiration rates from the vegetation is regulated by the aerodynamic resistance and the surface resistance. The aerodynamic resistance (r_{hrc}) and the wet canopy resistance

(*rvc*) to evaporated water on the wet canopy surface is expressed as Equation 2.39 and Equation 2.40 as (Mu *et al.*, 2011):

$$rhc = \frac{1}{gl_{sh} \times LAI \times F_{wet}} \quad (2.37)$$

$$rrc = \frac{\rho \times C_p}{4 \times \sigma \times T_i^3} \quad (2.38)$$

$$rhrc = \frac{rhc \times rrc}{rhc + rrc} \quad (2.39)$$

$$rvc = \frac{1}{gl_{e_{wv}} \times LAI \times F_{wet}} \quad (2.40)$$

Where *rhc* (s. m⁻¹) is the wet canopy resistance to sensible heat, *rrc* (s. m⁻¹) is the resistance to radiative heat transfer through air, *gl_{sh}* (s. m⁻¹) is the leaf conductance to sensible heat per unit LAI, *gl_{e_{wv}}* (s. m⁻¹) is the leaf conductance to evaporated water vapour per unit LAI and σ (W. m⁻². K⁻⁴) is the Stefan-Boltzmann constant.

Succeeding the Biome-BGC model (Thornton, 1998), *ET* on a wet canopy surface is expressed as Equation 2.41 as:

$$\lambda E_{wet_c} = \frac{\left[(s \times A_c \times F_c) + \left(\rho \times C_p \times F_c \times \frac{(e_{sat} - e)}{rhrc} \right) \right] \times F_{wet}}{s + \left(\frac{\rho \times C_p \times rvc}{\lambda \times \epsilon \times rhrc} \right)} \quad (2.41)$$

Where the resistance to latent heat transfer (*rvc*) is the sum of *rhrc* and *r_s* in Equation 2.28.

Plant transpiration occurs during both daytime and night-time, however night-time transpiration was ignored in the old MOD16 algorithm and is now included in the revised and updated MOD16 algorithm (Mu *et al.*, 2011). In the previous version of the MOD16 algorithm, the surface conductance (*C_c*) was estimated using LAI to scale stomatal conductance (*C_s*) from the leaf level up to the canopy level (Landsberg and Gower, 1997; Mu *et al.*, 2007), as expressed in Equation 2.42 and Equation 2.43 as:

$$C_s = C_L \times m(T_{min}) \times m(VPD) \quad (2.42)$$

$$C_c = C_s \times LAI \quad (2.43)$$

Where *C_L* is the mean potential stomatal conductance per unit leaf area, *m(T_{min})* is a multiplier that limits potential stomatal conductance by minimum air temperatures (*T_{min}*) and *m(VPD)* is

a multiplier used to reduce the potential stomatal conductance when VPD is high enough to reduce canopy conductance (Zhao *et al.*, 2005; Mu *et al.*, 2007). In the old MOD16 algorithm, C_L was constant for all variations of biomes. However, in the improved MOD16 algorithm, C_L varies according to the type of biome found, as shown in Kelliher *et al.* (1995); Schulze *et al.* (1994) and White *et al.* (2000).

In the modified MOD16 algorithm, the method to estimate C_c has been revised. The canopy conductance to transpired water vapour per unit area LAI, results from the stomatal and cuticular conductance that are parallel with each other and are both in series with leaf boundary layer conductance (Thornton, 1998; Running and Kimball, 2006).

$$r_{corr} = \frac{1}{\left(\frac{101300}{P_a}\right) \times \left(\frac{T_i + 273.15}{293.15}\right)^{1.75}} \quad (2.44)$$

$$G_s^1 = \begin{cases} C_L \times m(T_{min}) \times m(VPD) \times r_{corr} & i = \text{daytime} \\ 0 & i = \text{night-time} \end{cases}$$

$$G_{cu} = g_{cu} \times r_{corr} \quad (2.45)$$

$$G_s^2 = g_{sh} \quad (2.46)$$

$$G_{c_i} = \begin{cases} \left[\frac{G_s^2 \times (G_s^1 + G_{cu})}{G_s^1 + G_s^2 + G_{cu}} \right] \times LAI \times (1 - F_{wet}) & [LAI > 0, (1 - F_{wet}) > 0] \\ 0 & [LAI = 0, (1 - F_{wet}) = 0] \end{cases}$$

$$r_{s_i} = \frac{1}{c_{c_i}} \quad (2.47)$$

Where P_a is the atmospheric pressure, G_s^i are daytime and night-time stomatal conductance, G_{cu} is the leaf cuticular conductance, g_{cu} is the cuticular conductance per unit LAI, which has a constant value of 0.0001 m.s^{-1} for all biomes, G_s^2 is the leaf boundary-layer conductance and g_{sh} is the leaf conductance to sensible heat per unit LAI and further information for each constant value is given in Mu *et al.* (2011).

In the revised version of the MOD16 algorithm, P_a is calculated as a function of the elevation (Thornton, 1998) and is expressed as Equation 2.50 as:

$$t_1 = 1 - \frac{LR_{STD} \times Elev}{T_{STD}} \quad (2.48)$$

$$t_2 = \frac{G_{STD}}{LR_{STD} \times \frac{RR}{MA}} \quad (2.49)$$

$$P_a = P_{STD} \times t_1^{t_2} \quad (2.50)$$

Where LR_{STD} is the standard temperature lapse rate and has a constant value of 0.0065 K. m⁻¹, T_{STD} is the standard room temperature at 0 m elevation and has a constant value of 288.15 K, G_{STD} is the standard gravitational acceleration and has a constant value of 9.82 m. s⁻², RR is a gas law constant with a value of 8.3143 m³. Pa. mol⁻¹. K⁻¹, MA has a constant value of 28.9644e-3 kg. mol⁻¹ and is the molecular weight of air, and P_{STD} is the standard pressure at 0 m elevation and has a constant value of 101325 Pa (Mu *et al.*, 2011).

The transfer of heat and water vapour from the dry canopy surface into the air above the canopy is determined by the aerodynamic resistance (r_a), which is considered as a parallel resistance to convective (rh) and radiative (rr) heat transfer following Biome-BGC model (Thornton, 1998).

$$r_a = \frac{rh \times rr}{rh + rr} \quad (2.51)$$

$$rh = \frac{1}{gl_{bl}} \quad (2.52)$$

$$rr = \frac{\rho \times C_p}{4 \times \sigma \times (T_i + 273.15)^3} \quad (2.53)$$

Where gl_{bl} is the leaf-scale boundary layer conductance (m. s⁻¹) and is equal to gl_{sh} and σ (W. m⁻². K⁻⁴) is the Stefan-Boltzmann constant.

The plant transpiration (λE_{trans}) is calculated as Equation 2.54 (Mu *et al.*, 2011) as:

$$\lambda E_{trans} = \frac{\left[(s \times A_c) + \rho \times C_p \times F_c \times \left(\frac{e_{sat} - e}{r_a} \right) \right] \times (1 - F_{wet})}{\left[s + \gamma \times \left(1 + \frac{r_s}{r_a} \right) \right]} \quad (2.54)$$

Where r_a is the aerodynamic resistance which was calculated in Equation 2.50.

The potential plant transpiration (λE_{pot_trans}) is calculated following the Priestly-Taylor (Priestley and Taylor, 1972), and is expressed as Equation 2.44 as:

$$\lambda E_{pot_trans} = \frac{\alpha_2 \times s \times A_c \times (1 - F_{wet})}{(s + \gamma)} \quad (2.55)$$

Where $\alpha_2 = 1.26$.

The soil surface is separated into the saturated surface covered with water and the moist surface by F_{wet} . The soil evaporation includes the potential evaporation from the saturated soil surface and evaporation from the moist soil surface (Mu *et al.*, 2011). The aerodynamic resistance to vapour transport (r_{tot}) is expressed as Equation 2.55 (van de Griend and Owe, 1994; Mu *et al.*, 2007) as:

$$r_{tot} = r_s + r_v \quad (2.56)$$

Where r_s is the surface resistance and r_v is the aerodynamic resistance to water vapour. In the old MOD16 algorithm, r_{tot} was assumed to be 107 s. m^{-1} globally (Wallace and Holwill, 1997), however it was corrected for atmospheric temperature (T_i) and pressure (P_a) (Jones, 1992) and is expressed in Equation 2.57 and Equation 2.58 as:

$$r_{corr} = \frac{1}{\frac{101300}{P_a} \times \left(\frac{T_i + 273.15}{293.15} \right)^{1.75}} \quad (2.57)$$

$$r_{tot} = r_{totc} \times r_{corr} \quad (2.58)$$

Where T_i and P_a are assumed to be 20°C and 101300 Pa , respectively, r_{corr} is the correction for atmospheric temperature and pressure and r_{totc} is assumed to have a value of $107 \text{ (s. m}^{-1})$. The aerodynamic resistance at the soil surface (r_{as}) is parallel to the resistance to convective heat transfer (r_{hs}) (s. m^{-1}) and the resistance to radiative heat transfer (r_{rs}) (s. m^{-1}) (Choudhury and DiGirolamo, 1998) and is expressed as:

$$r_{as} = \frac{r_{hs} \times r_{rs}}{r_{hs} + r_{rs}} \quad (2.59)$$

$$r_{hs} = r_{tot} \quad (2.60)$$

$$r_{rs} = \frac{\rho \times C_p}{4 \times \sigma \times (T_i + 273.15)^3} \quad (2.61)$$

In the improved MOD16 algorithm, r_{totc} is not constant. For a specific biome type, there is a maximum ($r_{bl_{max}}$) and a minimum value ($r_{bl_{min}}$) for r_{totc} , and r_{totc} is a function of VPD .

$$r_{totc} = \begin{cases} r_{bl_{max}} & VPD \leq VPD_{close} \\ r_{bl_{max}} - \left[\frac{(r_{bl_{max}} - r_{bl_{min}}) \times (VPD_{close} - VPD)}{(VPD_{close} - VPD_{open})} \right] & VPD_{open} < VPD < VPD_{close} \\ r_{bl_{min}} & VPD \geq VPD_{close} \end{cases}$$

The values for rbl_{max} and rbl_{min} , VPD_{open} and VPD_{close} vary for different biomes and are discussed in Mu *et al.* (2011).

The actual soil evaporation (λE_{soil}) is expressed as Equation 2.64, using potential soil evaporation (λE_{soil_pot}) and a soil moisture constraint function in the Fisher *et al.* (2008) *ET* model. This function defines the land-atmosphere interactions from air *VPD* and relative humidity (*RH*%) (Mu *et al.*, 2011).

$$\lambda E_{wet_soil} = \frac{[(s \times A_{soil}) + (\rho \times C_p \times (1 - F_c) \times \frac{VPD}{r_{as}})] \times F_{wet}}{(s + \gamma) \times \frac{r_{tot}}{r_{as}}} \quad (2.62)$$

$$\lambda E_{soil_pot} = \frac{[(s \times A_{soil}) + (\rho \times C_p \times (1 - F_c) \times \frac{VPD}{r_{as}})] \times (1 - F_{wet})}{(s + \gamma) \times \frac{r_{tot}}{r_{as}}} \quad (2.63)$$

$$\lambda E_{soil} = \lambda E_{wet_soil} + \lambda E_{soil_pot} \times \left(\frac{RH}{100}\right)^{\frac{VPD}{\beta}} \quad (2.64)$$

Where the value of β was 100 in the old MOD16 algorithm, and the value has been revised to 200 in the improved MOD16 algorithm (Mu *et al.*, 2011).

The total daily *ET* and the potential *ET* (λE_{pot}) are expressed in Equation 2.65 and Equation 2.66 respectively as (Mu *et al.*, 2011):

$$\lambda E = \lambda E_{wet_c} + \lambda E_{trans} + \lambda E_{soil} \quad (2.65)$$

$$\lambda E_{pot} = \lambda E_{wet_c} + \lambda E_{pot_trans} + \lambda E_{wet_soil} + \lambda E_{soil_pot} \quad (2.66)$$

Where λE_{wet_c} is the evaporation from the wet canopy surface, λE_{trans} is the transpiration from the dry canopy surface and λE_{soil} is the evaporation from the soil surface.

The combination of *ET* with λE_{pot} can assist in the determination of water stress and in the recognition of drought intensity (Mu *et al.*, 2011), and it is able to provide important information on global terrestrial water and energy cycles and environmental variations (Mu *et al.*, 2011).

2.5.2 Case studies on the use of the MOD16 product

Many studies have implemented the MOD16A2 product to estimate ET_a , and a select few case studies have been presented in Table 2.4.

Table 2.4 Case studies on the application of the MOD16 and MOD16A2 product

Study	Main objective	Key findings
Mu <i>et al.</i> , 2007	The development of a global ET_a algorithm based on MODIS imagery and global meteorological data.	<ul style="list-style-type: none"> Revised the RS-PM algorithm by adding VPD and temperature constraints on stomatal conductance; utilising LAI to estimate canopy conductance from stomatal conductance; replaced NDVI with EVI and altered the equation to calculate the vegetation cover fraction; and the addition of a distinct soil evaporation component to ET_a. The revised RS-PM algorithm substantially reduced the RMSE of LE that was averaged over 19 towers from 64.6 W. m⁻² to 27.3 W. m⁻². The spatial pattern of the MODIS ET_a agreed well with the MOD17 GPP/NPP. The highest ET_a was produced over tropical forests, and the lowest ET_a in dry regions with short growing seasons.
Mu <i>et al.</i> , 2011	The improvement of the MODIS global terrestrial ET_a algorithm.	<ul style="list-style-type: none"> When comparing the improved algorithm with the old algorithm, the global annual ET_a over the vegetated surface agreed well over the terrestrial land surface. The improved algorithm reduced the MAE of ET_a from 0.39 mm. d⁻¹ to 0.33 mm. d⁻¹, when compared against the old algorithm.
Ramoelo <i>et al.</i> , 2014	To validate the MOD16 ET_a using 2 EC flux tower data for a 10-year period.	<ul style="list-style-type: none"> The MOD16 ET_a showed inconsistent comparisons with the Skukuza flux tower results. R² values of 0.58 and 0.85 was obtained for the years 2003 and 2007 respectively. The Malopeni flux tower consisted of a shorter study period (one year), producing an overestimation of ET_a. This resulted in an R² value of 0.23 being obtained.

Study	Main objective	Key findings
Aguilar <i>et al.</i> , 2018	To evaluate the performance of the MOD16A2 product by comparing it with EC data.	<ul style="list-style-type: none"> • <i>In-situ</i> data was available for five sites in North western Mexico, for a variety of landcovers. • The best performance observed over the shrubs yielded an R^2 of 0.86, and an RMSE of 0.77 mm. d^{-1}. • In most cases, MOD16 ET_a values obtained were underestimated.
Chang <i>et al.</i> , 2018	To evaluate and improve the MOD16 algorithm for ET_a estimation over an alpine meadow on the TP in China.	<ul style="list-style-type: none"> • Results were validated against EC data. • The modified MOD16 2011 algorithm performed better than the original MOD16 algorithm. • The R^2 value improved from 0.26 to 0.68, and the RMSE decreased by 0.86 mm. d^{-1}. • The modified MOD16 algorithm was able to produce improved estimates of ET_a.
He <i>et al.</i> , 2019	To improve the delineation of field scale ET_a in CONUS croplands by making use of the 2011 modified MOD16 algorithm framework.	<ul style="list-style-type: none"> • Results obtained were validated against <i>in-situ</i> data. • The ET_{MOD16} (MODIS MOD16A2 global operational ET_a product) yielded an R^2 value 0.54, and an RMSE value of 0.82 mm. d^{-1}.
Dzikiti <i>et al.</i> , 2019	A comparison was carried out between the Penman-Monteith based MOD16 and the modified Priestley-Taylor (PT-JPL) model to estimate ET_a over 3 biomes in South Africa.	<ul style="list-style-type: none"> • $R^2 < 0.50$ and $RMSE > 0.80$ mm. d^{-1} were observed during year with prolonged summer dry spells in summer rainfall regions. • Improvements were made to the MOD16 predictions. • Adjustments to the PT-JPL model produced minimal improvements.

2.6 Synthesis of Literature

Ramoelo *et al.* (2014) states that large quantities of precipitation within South African environments are returned to the atmosphere through ET_a . Therefore, it is imperative for us to understand this major process of the hydrological cycle in further detail, as it largely influences water resources management decisions (Timmermans *et al.*, 2013; Ramoelo *et al.*, 2014; Ke *et al.*, 2016; Gu *et al.*, 2017).

Various methods have been developed to account for ET_a in the hydrological cycle at different spatial and temporal scales. Satellite earth observation methods have been proposed and utilised as an alternative to conventional ET_a estimation methods, as they are easily accessible and provide inexpensive access to spatially representative data, at near-real time (Courault *et al.*, 2005). Montanari *et al.* (2013) states that remotely sensed data has the capacity to transform hydrological modelling approaches, especially in areas where meteorological networks and monitoring is sparse, such as South Africa where there is a deficiency of reliable ET_a data.

Multiple approaches have been established to estimate ET_a using SEO data. Methods based on the parameterisation of the shortened energy balance are often applied, with the most frequently utilised selections including; ETLOOK, SEBI, SEBAL, METRIC and SEBS (Menenti and Choudhury, 1993; Bastiaanssen *et al.*, 1998; Su *et al.*, 2002; Allen *et al.*, 2007; Jarman *et al.*, 2009; Pelgrum *et al.*, 2010). While these techniques have generally been shown to provide reliable estimates of terrestrial fluxes and ET_a , there still exists an influence of the land surface and air temperature gradient on ET_a and terrestrial flux estimates derived using SEO data.

According to Kalma *et al.* (2008), the temperature gradient significantly impacts the LE , R_n , G_o and H , which are components of the energy balance equation. In order to gauge the influence which the model conceptualisation has on the accuracy of the estimates, the SEBS model was selected for application and implemented using satellite-derived input variables derived from MODIS Terra and Aqua imagery, respectively. As a result of the diverse meteorological conditions and the differences in $T_o - T_a$ due to the differential heating of the land surface and air, variations and uncertainties are observed within the simulated and *in-situ* terrestrial flux estimates, as a lag effect occurs (Gibson *et al.*, 2013; Brenner *et al.*, 2017). Therefore, promoting the importance of the time of day of image acquisition and the choice of satellite sensor (MODIS Terra or Aqua) being utilised.

Furthermore, $ET_{MOD16A2}$ data was acquired and evaluated as part of these investigations, since this approach does not utilise $T_o - T_a$ during the estimation of ET_a . Subsequently, the use of the MOD16A2 product provides an ideal opportunity to further gauge the influence which the satellite-based energy balance ET model conceptualisation has on the accuracy of the terrestrial flux estimates.

The following chapter provides a concise description of the required data and methods that were utilised in order to fulfil the specific objectives outlined in this study.

3. METHODOLOGY

The literature review identified relevant models and methods to estimate ET_a and terrestrial flux estimates in a South African context. This chapter reviews the general methodology, description of the study sites, as well as the *in-situ* and satellite earth observed data used with SEBS.

3.1 General Methodology

The general methodology implemented in this study was aimed at fulfilling the research objectives outlined in Chapter one, which included:

- i. Evaluating the accuracy of satellite-derived ET_a and terrestrial flux estimates against *in-situ* measurements.
- ii. Implementing a satellite-based ET_a model to estimate ET_a and terrestrial fluxes.
- iii. Establishing the influence of the land surface and air temperature gradient on ET_a and terrestrial flux estimates through comparisons against *in-situ* measurements, as well as the MOD16 derived ET_a .

The first section of this study was aimed at utilising MODIS Terra and MODIS Aqua satellite imagery to derive the requisite inputs used in the SEBS model. The SEBS derived MODIS Terra ET_a (ET_{Terra}), MODIS Aqua ET_a (ET_{Aqua}) and terrestrial flux estimates were compared against ET *in-situ* data measured using an Eddy Covariance system.

Following the validation of the SEBS derived satellite-based ET_a and terrestrial flux estimates, using MODIS Terra and Aqua imagery, the influence of the land surface temperature on the estimates were obtained. This could occur as a result of the imagery being obtained at different times. Therefore, differences in ET_a and terrestrial flux estimates may occur, resulting from the temperature gradient, which influences the ET_a and terrestrial flux estimates. Thereafter, the ET_{Terra} and ET_{Aqua} estimates were aggregated to 8-day ET_a estimates. The MOD16A2 ET_a ($ET_{MOD16A2}$) estimate, and the aggregated ET_{Terra} and ET_{Aqua} were thereafter compared against *in-situ* data at the riparian and savanna regions. Since the MOD16 algorithm does not utilise T_o-T_a during the estimation of ET_a , the use of the MOD16A2 product provides an ideal opportunity to further gauge the influence which satellite-based energy balance ET model conceptualisation has on the accuracy of the terrestrial flux estimates.

The comparisons that were carried out in this study are summarised in Figure 3.1. The methodology is structured such that the research questions and the aims and objectives identified in Chapter one is addressed. The SEBS model was implemented using satellite-derived input variables derived from MODIS Terra and Aqua imagery, respectively. Satellite earth observation data was collected during the period for which *in-situ* measurements were available (17th June to 12th August 2015 and 21st August to 21st October 2015). The EC system was initially installed near an irrigated farm, and measurements were obtained from the 17th June to 12th August 2015. Thereafter the system was relocated to a pristine protected region, 1.2 km downstream and measurements were obtained from the 21st August to 21st October 2015.

It should be noted that this period also coincided with a large El Niño induced drought (Kogan and Guo, 2017). The simulated terrestrial fluxes and ET_a were then compared against observed ET_a to quantify the influence of the temperature gradient on the modelled estimates. Although satellite-based ET models generally provide fairly reliable estimates of terrestrial fluxes and ET_a , these models have the tendency to perform poorly in water stressed environments, due to an inherent limitation in their conceptualisation which relates to T_o-T_a . As a result of the diverse meteorological conditions and the differences in T_o-T_a due to the differential heating of the land surface and air, variations and uncertainties are observed within the simulated and *in-situ* terrestrial flux estimates, as a lag effect occurs (Gibson *et al.*, 2013; Brenner *et al.*, 2017). Therefore, promoting the importance of the time of day of image acquisition and the selection of satellite sensor (MODIS Terra or Aqua) being utilised.

Thereafter, in order to determine, the influence which the model conceptualisation has on the accuracy of the estimates, $ET_{MOD16A2}$ data was acquired and evaluated as part of these investigations. Since the MOD16 algorithm does not utilise T_o-T_a during the estimation of ET_a , the use of the MOD16A2 product provides an ideal opportunity to further gauge the influence which satellite-based energy balance ET model conceptualisation has on the accuracy of the terrestrial flux estimates.

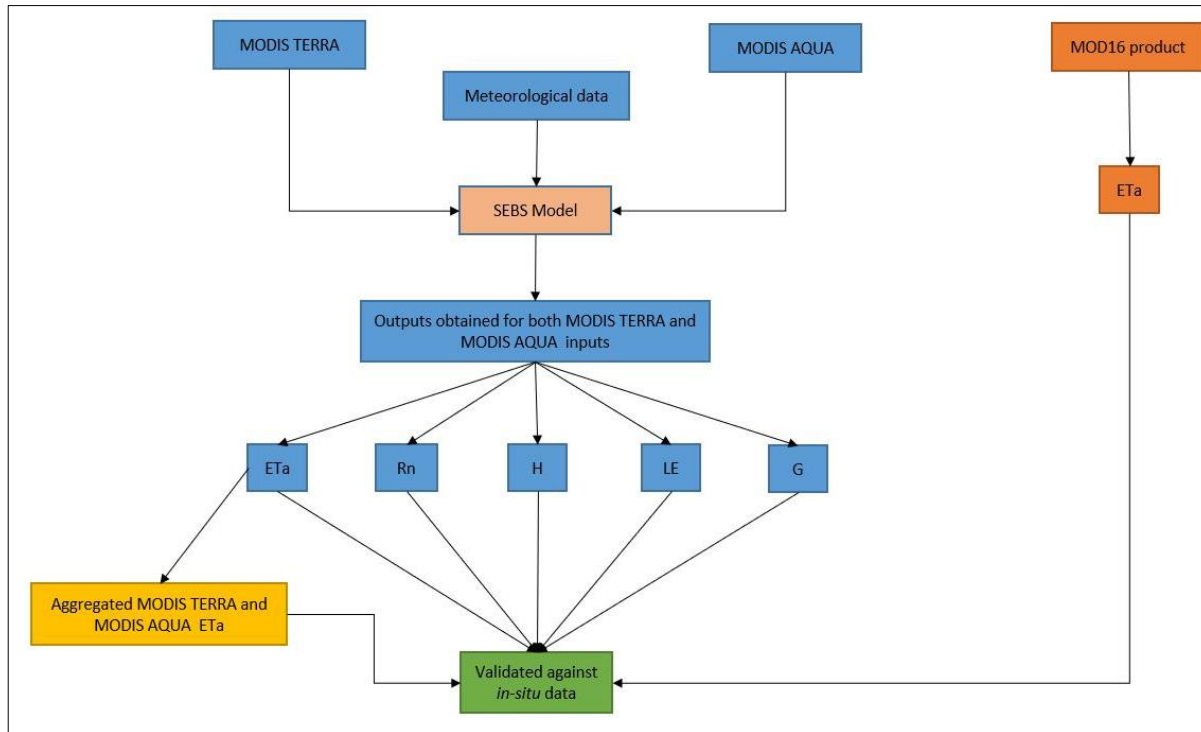


Figure 3.1 Graphical illustration of the methodology that was adopted in this study

3.2 Description of the Study Sites

The study area is situated in the Luvuhu and Letaba Water Management area within the Limpopo province, which is located in the north-eastern region of South Africa (Gokool *et al.*, 2017). Two study sites within this region were chosen to conduct the investigations. This was largely due to their contrasting environmental settings, as well as the availability of *in-situ* data records.

The riparian area sites are situated within the Letaba catchment along the Groot Letaba River channel, between the Letaba Ranch (23.66°S and 31.05°E) and the Mahale weirs (23.67°S and 31.05°E), 332 m above sea level, as seen in Figure 3.2. Site 1 is located at 23.67°S and 31.02°E, whilst site 2 is located at 23.67°S and 31.03°E. Site 1 consists of a greater amount of bare soil than site 2, which is a much more pristine area, and is influenced by climatic conditions. The Groot Letaba River which flows through the Kruger National Park (Gokool *et al.*, 2017), often experiences water shortages as a result of the increased water demands that is used for commercial agriculture in its upper reaches (Gokool *et al.*, 2019).

The Letaba catchment is regarded as being a semi-arid region, which frequently experiences water shortages (Pollard and du Toit, 2011). The Mean Annual Temperature (MAT) ranges

between 18.00°C and 28.00°C, with the temperature varying from cooler conditions in the mountainous regions and warmer conditions in the eastern regions (Sinha and Kumar, 2015). The Mean Annual Precipitation (MAP) is approximately 417.50 mm, and seasonal rainfall occurs, with majority of the rainfall occurring in the summer months, between October to March (Katambara and Ndiritu, 2010; Pollard and du Toit, 2011a; Strydom *et al.*, 2014), whilst the mean annual potential A-pan evaporation is approximately 2097.93 mm (Schulze *et al.*, 2008; Gokool *et al.*, 2017).

The study site is dominated by alluvial channel types (Heritage *et al.*, 2001), and the Mean Annual Runoff (MAR) of the catchment is approximately 574 million m³ (Sinha and Kumar, 2015). The catchment is dominated by savannah vegetation, and the soil structure is primarily sand, with most of the catchment being underlain with gneiss and granite rock (Heritage *et al.*, 2001; Pollard and du Toit, 2011).

The Malopeni flux tower is located at 23.83°S and 31.22°E, is situated along a hot and dry broad-leaf Mopane savanna and is 384 m above sea level. The annual rainfall ranges between 99.40 mm and 850.90 mm, whilst the MAP is approximately 472.00 mm (Kirton and Scholes, 2012). The temperature ranges between 12.40°C and 30.50°C (Kirton and Scholes, 2012). The Malopeni flux tower was established in 2009 as part of the CARBOAFRICA network, which is part of the quantification, understanding and prediction of carbon cycle and other GHG gases in Sub-Saharan Africa project (CARBOAFRICA) network (Gokool *et al.*, 2019). The CarboAfrica network is recognised as part of the global Fluxnet community, with strong connections to the CarboEurope network (Bombelli *et al.*, 2009; Merbold *et al.*, 2009).

The vegetation at the site is dominated by *Colophospermum mopane* (Ramoelo *et al.*, 2014), in addition *Combretum apiculatum* and *Verchellia nigrescens* are also abundant. The grass layer is dominated by *Schmidtia pappophoroides* and *Panicum maximum*. The underlying geology of the Malopeni study site is Archaean Basement granites and gneisses, with the soil texture primarily comprising of sandy loam (Kirton and Scholes, 2012).

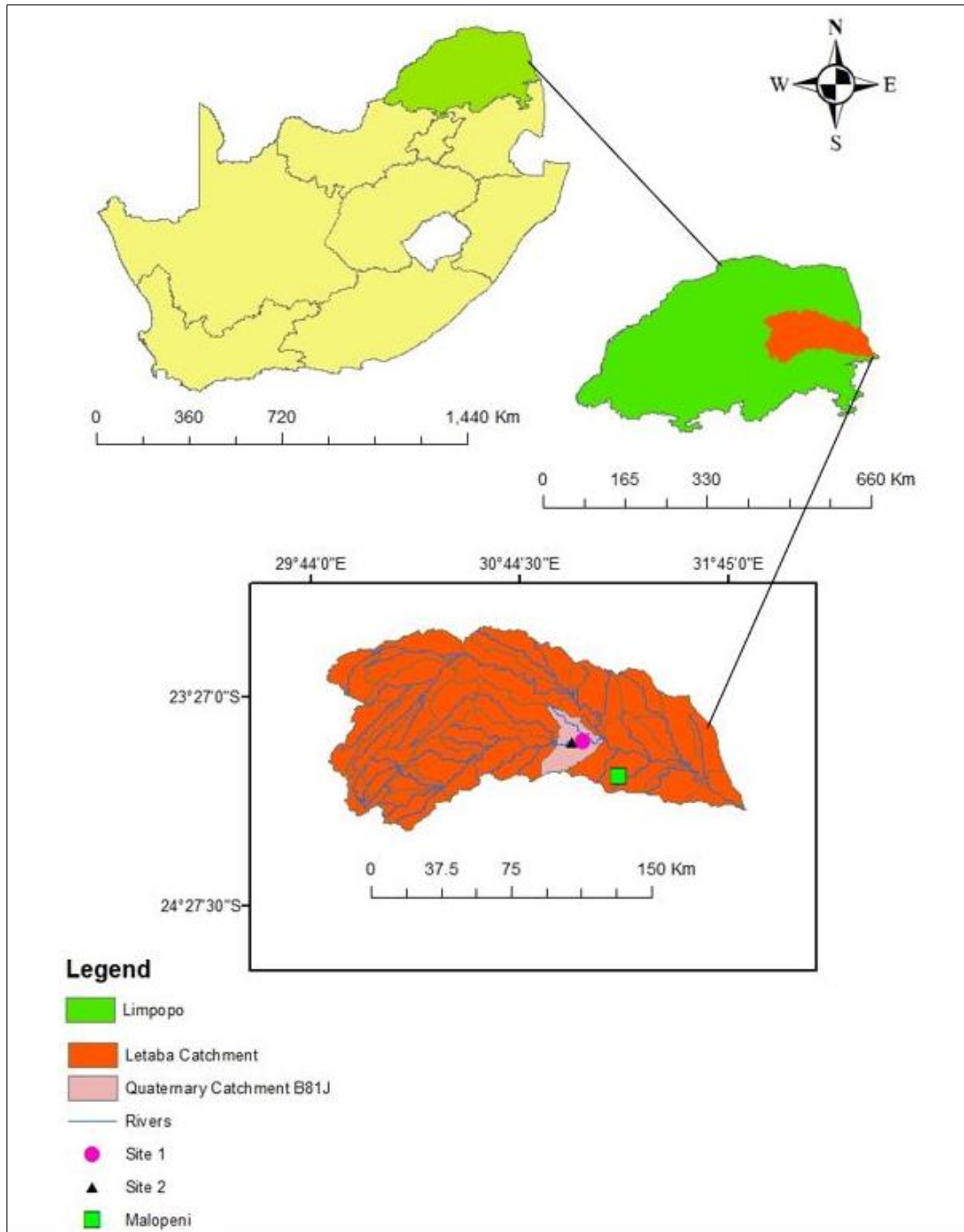


Figure 3.2 Location of the study sites within the Letaba Catchment, Limpopo Province, South Africa

3.3 Meteorological Data Acquisition for the SEBS Model

Meteorological data was obtained from a study undertaken by Gokool *et al.* (2017). It should be noted that the data collected for site 1 and site 2 were combined and treated as one data set in order to provide a longer data record which could be used for analysis. The *in-situ* measurements were used in conjunction with satellite-earth observation data acquired during

this study to derive input parameters that were required to perform simulations within the SEBS model. The data included net radiation, solar radiation, soil heat flux density, soil temperature, relative humidity, horizontal wind speed and direction, air temperature and rainfall. Gokool *et al.* (2017) installed an EC system at two different sites along the Groot Letaba River. Measurements were taken at a frequency of 10 Hz and logged every 10 minutes on a CR3000 data logger.

A CSAT 3-D sonic anemometer was used to measure air temperature, wind speed and 3-D wind direction. The anemometer was located at 2 m above the soil surface and approximately 1 m above the vegetation height (Gokool *et al.*, 2017). Two Kipp and Zonen NR Lite-Z net radiometers were installed approximately 1 m above the bare soil and vegetation, to measure net radiation above these surfaces. The instrumentation also consisted of a Texas Tipping bucket raingauge, Licor LI200X Pyranometer, RM Young wind sentry, HMP60 temperature and relative humidity sensor, six HFP01 Hukse Flux soil heat flux plates, three pairs of soil temperature averaging probes and two CS616 soil water reflectometers (Gokool *et al.*, 2017).

The EC system located at the Malopeni study site utilised was a LiCOR 7500 IRGA, with a Gill WindPro sonic anemometer (Gokool *et al.*, 2019). The EC sampling was undertaken at 8 m above ground level. The Decagon ECH₂O EC-5 soil moisture probes were located at four soil depths throughout the profile (0.05, 0.15, 0.25 and 0.40 m) (Gokool *et al.*, 2019). The Malopeni flux tower has been collecting data since 2008, however, due to equipment failure no data was recorded between January 2010 and January 2012 (Gokool *et al.*, 2019). The EC measurements were obtained from the 17th June to 12th August 2015, and from 21st August to 21st October 2015. The EC data that was considered, was from 6am until 6pm, assuming that ET_a takes place from sunrise till sunset (Gribovski *et al.*, 2010).

3.4 Satellite Data Acquisition as an Input into the SEBS Model

The water vapour content was attained from the NASA earth observatory website (<https://earthobservatory.nasa.gov>) and utilised as an input into the SEBS model. The SEBS model was implemented to estimate ET_a and terrestrial flux estimates, and thereafter compared against *in-situ* EC data at the various study sites. The satellite-derived input variables obtained were used to derive input parameters, that were required to perform simulations within the SEBS model, as seen in Figure 3.1. MODIS Terra and MODIS Aqua imagery were obtained for the corresponding period for which *in-situ* measurements were available. The pre-

processing and processing of the MODIS bands were undertaken based on the procedures carried out by Su and Wang (2013) and USGS (2016).

3.4.1 The pre-processing of MODIS Terra and Aqua satellite imagery

The MODIS Terra and MODIS Aqua satellites are able to view the entire earth's surface every, one to two days, therefore obtaining data in 36 spectral bands (Che *et al.*, 2003; Xiong *et al.*, 2008). MODIS has a swath width of 2330 km and it provides a global coverage daily. The data is obtained in 36 high spectral resolution bands, between 0.415 and 14.235 μm , with spatial resolutions of 250 m (2 bands), 500 m (5 bands) and 1000 m (29 bands) (Che *et al.*, 2003; Savtchenko *et al.*, 2004; Xiong *et al.*, 2008).

The MODIS instrument is located on the Terra (Earth Observing System (EOS) AM) and Aqua (EOS PM) satellites, which are in orbit approximately 705 km above the earth (Savtchenko *et al.*, 2004; Xiong *et al.*, 2009). The MODIS Terra and MODIS Aqua satellites were launched on 18 December 1999 and 4 May 2002, respectively (Xiong *et al.*, 2008). The orbits of the satellites differ, as the MODIS Terra satellite orbits the earth from North to South and passes over the equator at 10:30 am (descending) (Xiong *et al.*, 2008; Muhammed, 2012). Whilst the MODIS Aqua satellite orbits the earth from South to North and passes over the equator at 1:30 pm (ascending) (Xiong *et al.*, 2008; Savtchenko *et al.*, 2004). Therefore, the orbital times are beneficial in providing earth observations in the late morning and early afternoon. Salomonson *et al.* (2001) stated that this would aid in the analysis of daily changes of different systems and it would provide a long-term and reliable data set, utilising the same geophysical parameters for the study of climate and global change.

As a result of the imagery being obtained at different times, differences in ET_a and terrestrial flux estimates may occur. This could possibly occur as a result of the temperature gradient, which influences the ET_a and terrestrial flux estimates. This may arise, due to the inputs used in the SEBS model, such as; solar radiation, wind speed and air temperature, as these values vary for the acquisition times of MODIS Terra and Aqua imagery, respectively. The temperature gradient and land surface temperature impact LE , R_n , G_o and H , which are components of the energy balance equation (Kalma *et al.*, 2008). Kalma *et al.* (2008) states that there are errors related with utilising surface temperature to estimate H , such as; errors in observed meteorological data, errors in model assumption and the significant inaccuracies in

radiometric temperature estimation and the inequality between radiometric and aerodynamic surface temperature.

According to Yagci and Santanello (2017), land surface temperature derived from thermal infrared (TIR) region is a significant variable, as it comprises of information regarding the surface energy balance, terrestrial water stress and ET_a . Soil temperature, and consequently land surface temperature, increases with a decrease in soil moisture, while a deficiency of water content in plant root zones results in stomatal closure, to reduce water loss through transpiration, and ultimately increased canopy temperatures (Yagci and Santanello, 2017; Zheng *et al.*, 2019). Therefore, this influences the results obtained, as the study was conducted during a period with a large El Niño induced drought.

The use of MODIS imagery provides day and night images to be made available daily of the Earth (Hulley *et al.*, 2012). Terra and Aqua MODIS Level 1B calibrated radiances (MOD21KM and MYD21KM), as well as geolocation (MOD03 and MYD03) files were downloaded and utilised to derive the requisite inputs to estimate daily ET_a using SEBS. It should be noted that the SEBS ET_a output, is the output at the spatial scale of the thermal band, which is 1 km, as seen in Table 3.1.

Table 3.1 Description of the MODIS Terra and Aqua imagery used in the SEBS model

Sensors	Product	Level 1 Product	Spatial Resolution (Thermal Band)	Temporal Resolution
MODIS TERRA	MODO21KM	Level 1B calibrated radiances	1 Km	Daily
	MOD03	Geolocation	1 Km	Daily
MODIS AQUA	MYDO21KM	Level 1B calibrated radiances	1 Km	Daily
	MYD03	Geolocation	1 Km	Daily

There are four main steps in the processing of MODIS data, *viz*; re-projection and conversion of MODIS data, importing of MODIS images into ILWIS, pre-processing of data for SEBS and extraction of data from SEBS. The MODIS Level 1B data needed to be re-projected to a standard projection from an orbit-based format, to be compatible with Geographic Information Systems (GIS) software (Su and Wang, 2013). The ModisSwath Tool was used to convert MODIS data into GeoTIFF data. Table 3.2 displays the bands that were extracted using the ModisSwath Tool and subsequently used in ILWIS.

Table 3.2 Bands that are extracted and utilised in ILWIS (adapted from Su and Wang, 2013)

Input GeoTIFF filename	Output filename in ILWIS
EV_250_Aggr1KM_RefSB_b0.tif	Band1_dn
EV_250_Aggr1KM_RefSB_b1.tif	Band2_dn
EV_500_Aggr1KM_RefSB_b0.tif	Band3_dn
EV_500_Aggr1KM_RefSB_b1.tif	Band4_dn
EV_500_Aggr1KM_RefSB_b2.tif	Band5_dn
EV_500_Aggr1KM_RefSB_b4.tif	Band7_dn
EV_1KM_Emissive_b10.tif	Band31_dn
EV_1KM_Emissive_b10.tif	Band32_dn
SolarZenith.tif	sza_dn
SolarAzimuth.tif	saa_dn
SensorAzimuth.tif	vza_dn
SensorZenith.tif	vza_dn
Height.tif	Height

The MODIS Level 1B data was initially represented as a simplified integer (SI) number, which was required to be converted to obtain reflectance and radiance values. The conversion was conducted by applying a calibration coefficient, which was found in the metadata file and read using the HDFView software (Su and Wang, 2013). The zenith and azimuth maps were rescaled by finding the product between a scale factor of 0.01 and each map (Su and Wang, 2013).

The brightness temperature computation tool was used to convert bands 31 and 32 from radiances to blackbody temperatures by applying the Planck equation, expressed as Equation 3.1 (Su and Wang, 2013):

$$T_c = \frac{C_2}{\lambda_c \log\left(\frac{C_1}{(\lambda_c)^5 \pi L_s} + 1\right)} \quad (3.1)$$

Where T_c is the brightness temperature from a central wavelength, λ_c is the sensors central wavelength and C_1 and C_2 are the blackbody constants (Su and Wang, 2013).

The Simplified Model for Atmospheric Correction (SMAC) was developed by Rahman and Dedieu (1994) and was utilised to correct the atmospheric and scattering of bands 1 to 5 and band 7 in the visible channels (Su and Wang, 2013). Thereafter, bands 1 and 2 from this

correction were used to calculate the Normalised Difference Vegetation Index (NDVI), as seen in Equation 3.2:

$$NDVI = \frac{B_{nir} - B_{red}}{B_{nir} + B_{red}} \quad (3.2)$$

The land surface albedo was determined using the atmospherically correct bands 1 to 5 and band 7, using the Equation 3.3 which was derived by Liang (2001) and Liang *et al.* (2003):

$$Albedo = (0.160 \times r_1) + (0.291 \times r_2) + (0.243 \times r_3) + (0.116 \times r_4) + (0.112 \times r_5) + (0.018 \times r_7 - 0.0015) \quad (3.3)$$

Where r_1, r_2, r_3, r_4, r_5 and r_7 are bands 1 to 5 and band 7 in the visible channel.

The land surface emissivity was calculated to produce the surface emissivity using the visible and near-infrared bands, which was based on the method described by Sobrino *et al.* (2003).

The land surface temperature (LST) was estimated using a split window method, using Equation 3.4 derived by Sobrino *et al.* (2003):

$$LST = btm_{31} + 1.02 + (1.79) \times (btm_{31} - btm_{32}) + (1.2) \times (btm_{31} - btm_{32})^2 + (34.83 - 0.68 \times W) \times (1 - \varepsilon_s) + (-73.27 - 5.19 \times W) \times de \quad (3.4)$$

Where btm_{31} and btm_{32} are the brightness temperature, which were obtained from band 31 and band 32, W is the water vapour content, ε_s is the surface emissivity and de is the surface emissivity difference (Su and Wang, 2013).

Subsequent to the application of the SEBS model, statistical analysis was performed on the ET_a and terrestrial flux estimates that were attained. The results are presented in the following chapter.

3.5 Acquisition of The MOD16 Product

The continuous improvement of SEO data and GIS technologies has provided an alternative to conventional data acquisition approaches and are able to provide information within a range of spatio-temporal scales, and in data-scarce regions (Gokool *et al.*, 2016). However, challenges are experienced as a result of the application effort, technical expertise and information technology (IT) resources that are needed (Gorelick *et al.*, 2017).

Subsequently, this has limited the use of SEO data to those that are skilled and knowledgeable (Gorelick *et al.*, 2017). Recently, this situation has been altered with the introduction of Google Earth Engine (GEE). Gorelick *et al.* (2017) describes GEE as a cloud-based computing platform for planetary-scale geospatial analysis, which uses Google's computational power to process multi-petabyte curated collections of extensively used and freely available geo-spatial datasets (Sazib *et al.*, 2018).

In this study, GEE was used to obtain $ET_{MOD16A2}$ data for the various study sites. To access GEE, a registration and signup was required from <https://signup.earthengine.google.com/>. Thereafter, the required dataset was selected from the data catalogue, obtained from https://developers.google.com/earth-engine/datasets/catalog/MODIS_006_MOD16A2. A shapefile was created consisting of the required study sites and uploaded onto GEE. Scripts were created for the required dataset in the code editor within the GEE platform. The 'filterDate' code was used to specify the record length. Once the script was created, it was run, and the data was saved as a CSV file and opened in Microsoft Excel to be analysed.

The $ET_{MOD16A2}$ data was accessed via GEE, therefore reducing the computing time and making the satellite earth observed data readily available. Different datasets can be downloaded within GEE, such as; satellite, geophysical, weather images and demographic data (Sazib *et al.*, 2018). Thereafter, the $ET_{MOD16A2}$ estimates were validated against the aggregated *in-situ* EC data. This was recommended by Gibson (2013), as the MOD16 product does not require land surface temperature and observed data as inputs to obtain an ET_a estimate, therefore reducing uncertainties and errors in the data obtained. The MOD16A2 product, which is the most recent version of MOD16 (Aguilar *et al.*, 2018) was used in this study. An example of the script that was used within GEE is provided in Figure 7.1 of Appendix A.

The results of the $ET_{MOD16A2}$ estimates are presented in the subsequent chapter.

3.6 Statistical Metrics Used in the Study

In this study, satellite derived SEBS terrestrial flux estimates and ET_{Terra} , ET_{Aqua} and $ET_{MOD16A2}$ were compared against *in-situ* data. The model performance was evaluated using the coefficient of determination (R^2), Root Mean Square Error (RMSE) and Relative Volume Error (RVE) between the simulated ET_a and terrestrial flux estimates and the corresponding *in-situ* data (Krause *et al.*, 2005). The Pearson's correlation coefficient (r) was used to evaluate the strength of the relationship between the simulated and observed estimates (Reusser *et al.*, 2009), whilst

the Mean Absolute Difference (MAD) is a measure of statistical dispersion equal to the average absolute difference of two independent values drawn from a probability distribution (Willmott and Matsuura, 2005). Furthermore, the percentage of simulated ET_a estimates within an acceptable accuracy range (AAR) of $\pm 30\%$, when compared to *in-situ* observations were also determined (Kalma *et al.*, 2008; Gibson, 2013).

A Kruskal Wallis Test, which is a non-parametric test, was carried out, to identify significant relationships at the 95% significance threshold between the observed and simulated output (p-value ≤ 0.05) (Kruskal and Wallis, 1952). The null and alternate hypothesis were stated as follows:

H_0 : Simulated SEBS derived MODIS ET_a = Observed EC ET_a

H_a : Simulated SEBS derived MODIS $ET_a \neq$ Observed EC ET_a

4. RESULTS AND DISCUSSION

This chapter analyses and discusses the validation of ET_a and terrestrial flux estimates obtained from implementing the SEBS model using satellite derived input variables obtained from MODIS Terra and Aqua imagery, against *in-situ* data from the riparian and savanna regions. Thereafter, the 8-day aggregated simulated ET_{Terra} , ET_{Aqua} , and the $ET_{MOD16A2}$ estimates were compared against *in-situ* data from the study sites.

4.1 Terrestrial Flux Estimates at the Riparian Site

The *in-situ* measurements that were utilised in the riparian region were a combination of two study sites between the Letaba Ranch (23.66°S and 31.05°E) and the Mahale weirs (23.67°S and 31.05°E), therefore providing a data record of four months, as compared to two months had only one study site been observed.

4.1.1 Net radiation

Net radiation ($W \cdot m^{-2}$), R_n , is the total amount of radiation that reaches the earth's surface and is estimated from downward solar radiation (R_{swd}), reflected solar radiation and emitted longwave radiation (R_{lwd}). The SEBS derived R_n estimates showed a comparable correlation with the observed R_n data for both MODIS Terra and Aqua imagery, as shown in Table 4.1. Comparisons between the simulated R_{nTerra} and R_{nAqua} against the observed R_n data yielded R^2 values of 0.63 and 0.77, respectively. Although the simulated R_{nAqua} results were found to be marginally better than the R_{nTerra} when compared against the observed measurements, there still exists a fair degree of error between the two data sets.

Overall, SEBS was shown to overestimate R_n when compared against the *in-situ* measurements, as comparisons between R_{nTerra} and R_{nAqua} against the observed R_n data yielded Relative Volume Errors (RVE) of -56.06% and -53.09%, respectively. According to Lu *et al.* (2013), the main cause of the overestimation of R_n is the overestimation of the downward solar radiation. Therefore, the difference between the atmospheric, environmental and climatic conditions at the study sites may have resulted in the overestimation of R_n .

Table 4.1 Validation of Rn estimates obtained from implementing the SEBS model within the riparian region

	$Rn_{in-situ}$	Rn_{Terra}
AVERAGE (mm. d⁻¹)	268.78	419.47
STD DEV	163.75	206.32
RMSE (W. m⁻²)	195.78	
RVE (%)	-56.06	
MAD (mm. d⁻¹)	101.32	
PEARSON CORRELATION	0.79	
R²	0.63	

	$Rn_{in-situ}$	Rn_{Aqua}
AVERAGE (mm. d⁻¹)	329.79	504.88
STD DEV	139.36	198.16
RMSE (W. m⁻²)	201.80	
RVE (%)	-53.09	
MAD (mm. d⁻¹)	73.24	
PEARSON CORRELATION	0.88	
R²	0.77	

From Figure 4.1 and Figure 4.2, it can be seen that there is a greater overestimation of Rn for both Rn_{Terra} and Rn_{Aqua} from August 21st until October 21st 2015. However, both Rn_{Terra} and Rn_{Aqua} generally follow a similar trend as the *in-situ* data. The observed data used in this study for this particular region was acquired from two sites within the Letaba catchment, which were 1.2 km apart. The rationale for this was to combine the data for this region in order to have a longer-term dataset which could be used for statistical evaluations.

Study site 1 is strongly influenced by environmental conditions, such as land cover including bare soils, water limitations and atmospheric effects, whereas study site 2 within the riparian region is influenced by climatic conditions, as there is much more vegetation found in this region. Site 2 is a more pristine protected site, and livestock were prevented from grazing within this region (Gokool *et al.*, 2017). Seasonal and climatic changes also influence stress conditions which may have contributed to the increased vegetation cover at site 2. According to Gokool *et al.* (2017), the soil water availability along the section of the river that was studied was affected by the drought. Therefore, variations occurred in vegetation and canopy cover, and soil moisture status between site 1 and site 2, as discussed in Gokool *et al.* (2017). Small and Kurc (2001) state that in both grasslands and shrublands, when there is soil moisture, Rn and available energy both increase.

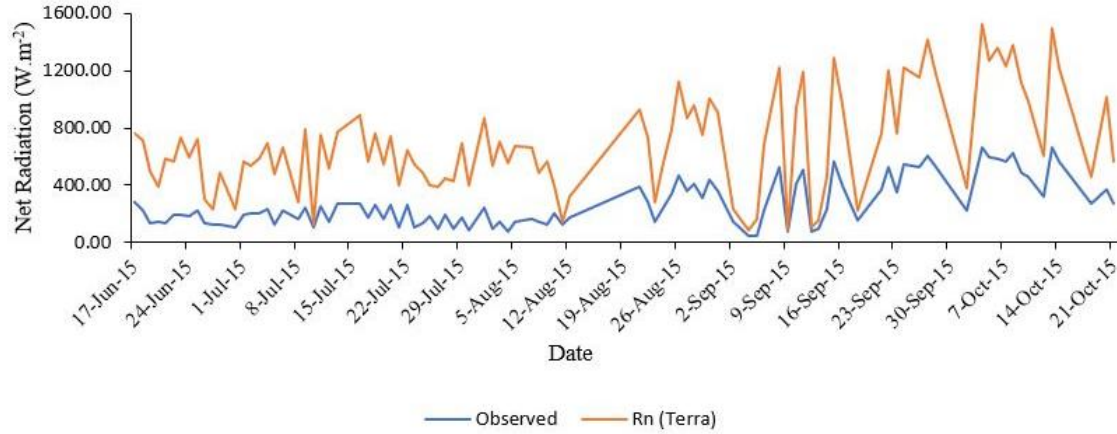


Figure 4.1 A time series comparison of Rn_{Terra} estimates obtained from implementing the SEBS model and observed data at the riparian region

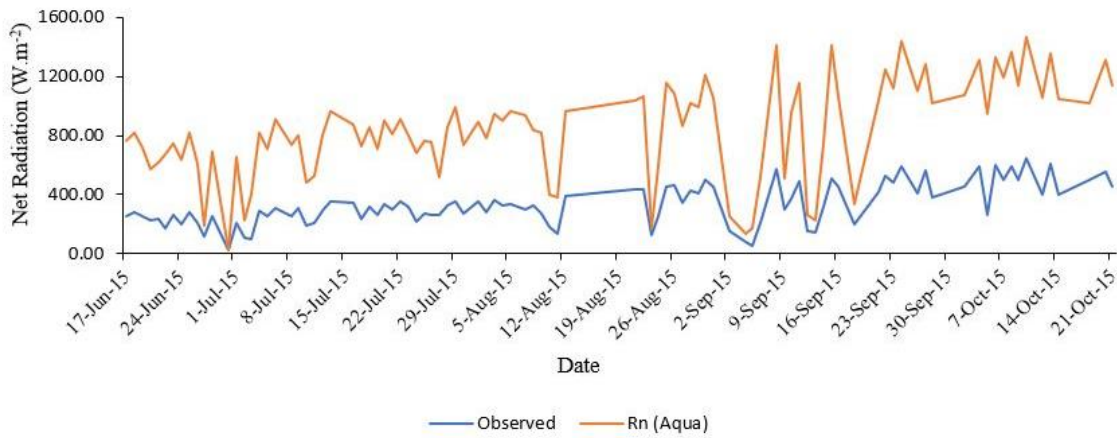


Figure 4.2 A time series comparison of Rn_{Aqua} estimates obtained from implementing the SEBS model and observed data at the riparian region

Overall, the simulated Rn estimates overestimates the *in-situ* Rn . This could possibly be as a result of the difference in the spatial and temporal scale of the measurements, that are observed by the field instruments and/or the MODIS Terra and Aqua sensors (Oku *et al.*, 2007). According to Tang *et al.* (2011), overestimations and uncertainties may also arise as a result of different spatial scales of remotely sensed data and *in-situ* data. The field instrument provides a point estimate, whilst *SEO* methods provide large scale estimates. The *in-situ* Rn measurements were determined using half-hourly averaged data, whilst the SEBS derived Rn_{Terra} and the Rn_{Aqua} were estimated using radiation values at the instantaneous time of the MODIS imagery.

Differences in Rn_{Terra} and the Rn_{Aqua} occur, as the MODIS Terra and MODIS Aqua imagery are obtained at different times, as a result of the different satellite overpass times. This may have an influence on the ET_a and terrestrial flux estimates obtained, which could possibly occur as a result of the land surface and air temperature gradient, that influences ET_a and terrestrial flux estimates. Regions consisting of sparse vegetation, are influenced by the amount of radiation reaching the soil and is highly dependent on the geometry of the sun and leaf orientations (Timmermans *et al.*, 2013).

According to Small and Kurc (2003), the relatively large EF fluctuations in semi-arid environments result in variations in surface temperature, which influences Rn through the influence of surface temperature on longwave radiation emitted from the surface. The Rn within the riparian region is overestimated, however, at site 2 (August 21st until October 21st 2015), the albedo of vegetated areas is much lower compared to bare soils (Van der Kwast *et al.*, 2009). According to Small and Kurc (2001), a lower albedo increases Rn , as a larger fraction of the incident short wave radiation is absorbed by the surface. In arid and semi-arid regions, the dry soil results in a higher albedo value, even though there are considerable variations in albedo under these conditions (Small and Kurc, 2001; Sumithranand *et al.*, 2009). Kjærsgaard *et al.* (2009) states that Rn normally fluctuates substantially during the day. If the surface Rn is larger, then the discrepancy between the estimated and measured Rn will be larger (Tang *et al.*, 2011).

4.1.2 Soil heat flux

The SEBS model was shown to overestimate Go as shown in Table 4.2, when compared against the *in-situ* measurements. Comparisons between the SEBS derived MODIS Terra soil heat flux estimate (Go_{Terra}) and SEBS derived MODIS Aqua soil heat flux estimate (Go_{Aqua}) estimate against the observed Go data yielded a RVE of -220.03% and -49.36%, respectively. This indicates an overestimation of both Go estimates, but a greater overestimation of Go_{Terra} estimates, when compared to the observed Go . The correlation between the data was 0.70 and 0.71 for Go_{Terra} and Go_{Aqua} respectively, indicating a positive association between the two variables.

Comparisons between the simulated Go_{Terra} and Go_{Aqua} , against the observed Go data yielded R^2 values of 0.49 and 0.51, respectively. Whilst an RMSE difference of 61.15 W. m⁻² was obtained between Go_{Terra} and Go_{Aqua} . As presented in Table 4.2, the assessment of error in data,

was carried out with the use of the Mean Absolute Difference (MAD) statistical metric, and yielded values of 34.43 mm. d⁻¹ and 31.19 mm. d⁻¹ for *Go_{Terra}* and *Go_{Aqua}* estimates, respectively.

Table 4.2 Validation of *Go* estimates obtained from implementing the SEBS model within the riparian region

	<i>Go_{in-situ}</i>	<i>Go_{Terra}</i>
AVERAGE (mm. d⁻¹)	38.74	123.99
STD DEV	38.21	57.87
RMSE	94.72	
RVE (%)	-220.03	
MAD (mm. d⁻¹)	34.43	
PEARSON CORRELATION	0.70	
R²	0.49	

	<i>Go_{in-situ}</i>	<i>Go_{Aqua}</i>
AVERAGE (mm. d⁻¹)	99.65	149.28
STD DEV	36.99	57.19
RMSE	63.57	
RVE (%)	-49.36	
MAD (mm. d⁻¹)	31.19	
PEARSON CORRELATION	0.71	
R²	0.51	

From Figure 4.3 and Figure 4.4, it can be seen that there is a greater overestimation of *Go* for both *Go_{Terra}* and *Go_{Aqua}* from August 21st until October 21st 2015. However, both *Go_{Terra}* and *Go_{Aqua}* generally follow a similar trend as the *in-situ* data. Seasonal changes in the *Go* also affect the surface energy balance, and hence the estimation of *ET_a*. The observed data used in this study for this particular region was acquired from two sites within the Letaba catchment, which were 1.2 km apart.

Study site 1 is more strongly influenced by environmental conditions, whereas study site 2 within the riparian region is influenced by climatic conditions, as there is much more vegetation found in this region. Site 2 is a more pristine protected site, and livestock were prohibited from grazing within this region (Gokool *et al.*, 2017). Seasonal and climatic changes also influence stress conditions, which may have contributed to the increased vegetation cover at site 2. According to Gokool *et al.* (2017), the soil water availability along the section of the river that was studied was affected by the drought. Therefore, variations occurred in vegetation and canopy cover, and soil moisture status between site 1 and site 2. Consequently, site 2 resulted in a greater overestimation of *Go* as compared to site 1. Cloudiness also influences the flow of heat into the soil. Therefore, less clouding results in a higher influx of heat into the soil, resulting in increased *Go* estimates being obtained (Roxy *et al.*, 2014).

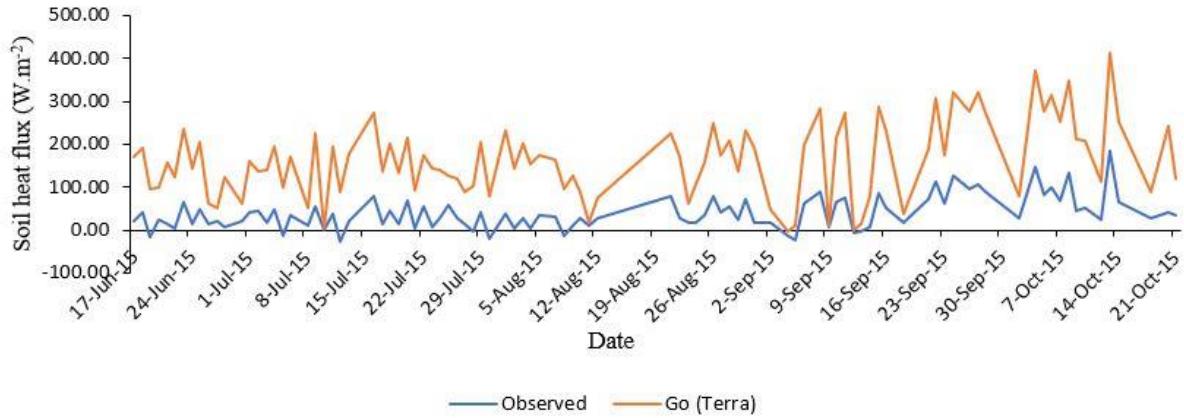


Figure 4.3 A time series comparison of Go_{Terra} estimates obtained from implementing the SEBS model and observed data at the riparian region

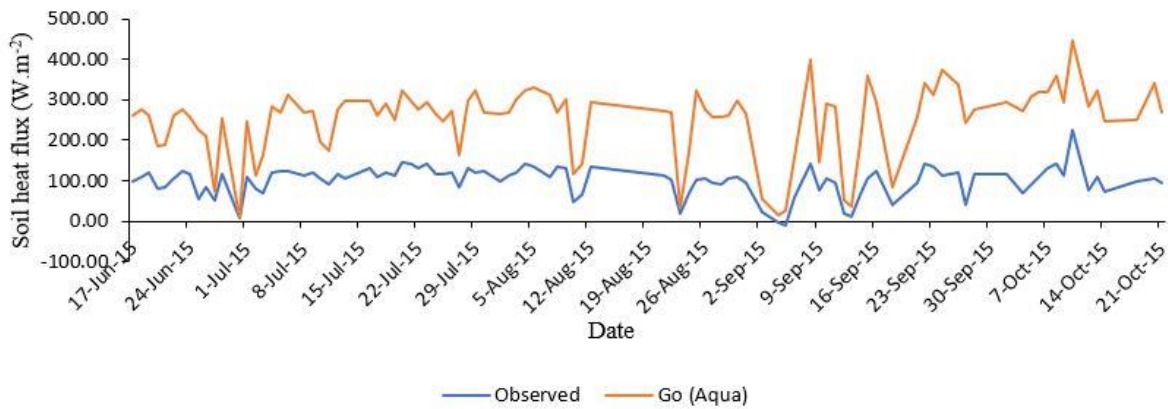


Figure 4.4 A time series comparison of Go_{Aqua} estimates obtained from implementing the SEBS model and observed data at the riparian region

Soil heat flux (Go) is the quantity of radiant energy, that is either absorbed or released at the soil surface (Roxy *et al.*, 2014). During non-rainy days, the net flow of heat is directed into the soil, and on rainy and cloudy days, the opposite occurs (Chacko and Renuka, 2002; Roxy *et al.*, 2014). Most of the days during the study period were non-rainy days, therefore resulting in higher Go values being obtained, as compared to instances where there had been an increase in soil water content. Soil heat flux is generally positive when it is directed into the soil, and negative when it is in the opposite direction (Roxy *et al.*, 2014).

Gokool (2017) states that site 1, had a greater amount of exposed bare soil as compared to site 2, and Riddell *et al.* (2017) states that the soils at site 1 was relatively drier than site 2. Therefore, the soil moisture and the amount of exposed bare soil influences the soil heat flux

density measured at the study sites (Sauer and Horton, 2005). In regions consisting of sparse vegetation, the amount of radiation reaching the soil depends on the geometry of the sun and leaf orientations (Timmermans *et al.*, 2013). Huang *et al.* (2015) states that the SEBS model overestimates ET_a in water limited conditions, whilst Pardo *et al.* (2014) and Gokmen *et al.* (2012) note that the overestimation of EF and LE in the SEBS model is higher, when the soil is dry and there is a reduced amount of vegetation cover. The direct soil evaporation component of ET_a is large, when there are vast areas of bare soil and when the soil is wet (Small and Kurc, 2003). According to Van der Kwast *et al.* (2009), the SEBS model is more sensitive to surface soil temperature than the surface aerodynamic parameters and was confirmed by Badola (2009).

Uncertainties arise as a result of calibration errors and errors related with field measurements, including spatial variation differences. The uncertainties related to *in-situ* measurements of G_o are dependent on the measurement errors due to variations in soil temperature from one measurement period to another and the uncertainty and errors in the measurement of soil water content (Savage *et al.*, 2004).

According to Xu *et al.* (2011), as satellite earth observed data is instantaneous, estimating the daily, monthly and annual fluxes may result in errors being observed. Tang *et al.* (2011) states that overestimations and uncertainties may arise due to the different spatial scales of the satellite earth observed data and *in-situ* data. Gibson *et al.* (2011) also emphasised the significance of the choice of satellite sensor being used, and therefore the pixel resolution and heterogeneity of the study area, as the uncertainties obtained are reflected in the estimation of ET_a .

4.1.3 Sensible heat flux

The SEBS model was shown to underestimate H as shown in Table 4.3, when compared against the *in-situ* measurements, as comparisons between the SEBS derived MODIS Terra sensible heat flux estimate (H_{Terra}) and SEBS derived MODIS Aqua sensible heat flux estimate (H_{Aqua}) against the observed H data yielded a RVE of 14.17% and 11.10%, respectively. This indicated an underestimation of both H estimates, but a greater underestimation of H_{Terra} , when compared to the observed H .

Comparisons between the simulated H_{Terra} and H_{Aqua} , against the observed H data yielded R^2 values of 0.02 and 0.01, respectively, indicating a large degree of error between the two

datasets. The R^2 and Pearson's R coefficient, although very low for both H_{Terra} and H_{Aqua} estimates, performed very similar with minimal difference between the values of both statistical indicators. Whilst the assessment of error in data, was carried out with the use of the Mean Absolute Difference (MAD) statistical metric, and yielded values of 34.73 mm. d⁻¹ and 48.85 mm. d⁻¹ for H_{Terra} and H_{Aqua} estimates, respectively.

Table 4.3 Validation of H estimates obtained from implementing the SEBS model within the riparian region

	$H_{in-situ}$	H_{Terra}
AVERAGE (mm. d⁻¹)	70.76	60.73
STD DEV	30.26	60.07
RMSE (W. m⁻²)	63.32	
RVE (%)	14.17	
MAD (mm. d⁻¹)	38.73	
PEARSON CORRELATION	0.16	
R²	0.02	

	$H_{in-situ}$	H_{Aqua}
AVERAGE (mm. d⁻¹)	69.77	62.02
STD DEV	30.94	65.21
RMSE (W. m⁻²)	69.41	
RVE (%)	11.10	
MAD (mm. d⁻¹)	48.85	
PEARSON CORRELATION	0.10	
R²	0.01	

From Figure 4.5 and Figure 4.6, it can be seen that there is a greater overestimation of H for both H_{Terra} and H_{Aqua} from August 21st until October 21st 2015. However, both H_{Terra} and H_{Aqua} generally follow a similar trend as the *in-situ* data. Seasonal changes in H also affect the surface energy balance, and hence the estimation of ET_a . The observed data used in this study for this particular region was acquired from two sites within the Letaba catchment, in order to have a longer-term dataset. Study site 1 is influenced by reduced land cover, increased amounts of bare soils, water limitations and atmospheric effects. Whilst site 2, is influenced by climatic conditions, and is a more pristine protected site, as livestock were prohibited from grazing within this region (Gokool *et al.*, 2017). The soil water availability differs along the portion of the river that was observed, hence variations in vegetation, canopy cover and soil moisture occur.

There is an extremely poor agreement between H_{Terra} and H_{Aqua} estimates when compared to the *in-situ* data, at their respective satellite overpass times. The underestimation of H and the overestimation of Rn , may have resulted in an overestimation of the latent heat flux (LE), resulting from decreased soil moisture, and an increase in the ability of evaporation and sparse vegetation cover (Zhuang and Wu, 2015). From August 21st until October 21st 2015 (Site 2), there is a greater difference between simulated and observed H estimates. This discrepancy

could have impacted on the remainder of the calculations carried out in the SEBS model, resulting in an increased EF , which results in an overestimation of ET_a . Several single-source models, such as the SEBS model underestimate H , especially over a partial canopy (Zhuang and Wu, 2015).

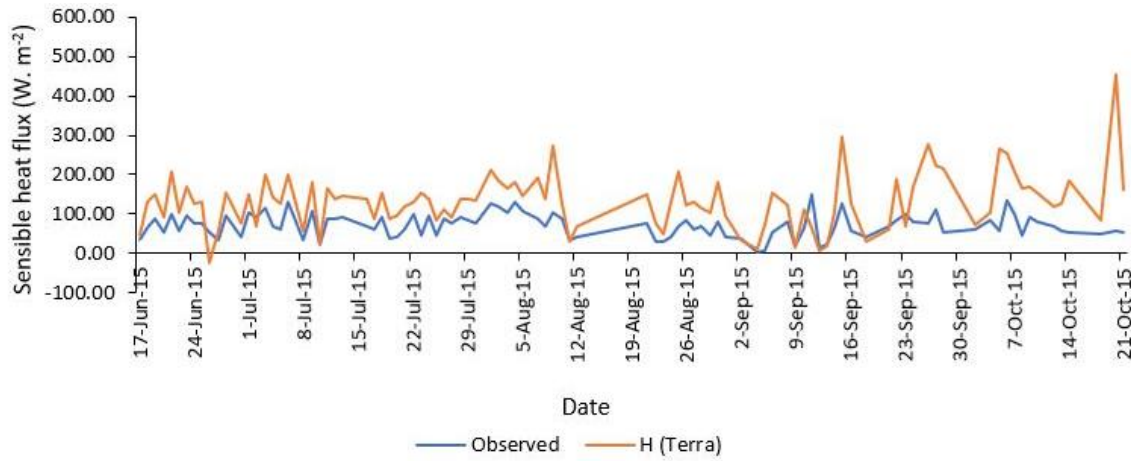


Figure 4.5 A time series comparison of H_{Terra} estimates obtained from implementing the SEBS model and observed data at the riparian region

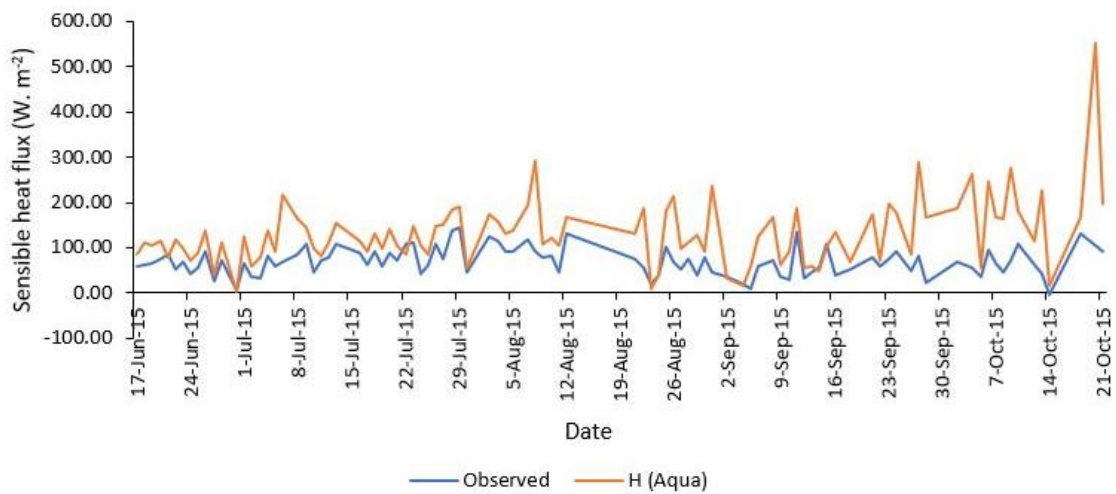


Figure 4.6 A time series comparison of H_{Aqua} estimates obtained from implementing the SEBS model and observed data at the riparian region

From Figure 4.7, it can be seen that the observed H estimate at the MODIS Aqua satellite overpass time, is much greater than the estimate obtained at the MODIS Terra satellite overpass time. This can be due to the difference in heating of the land, and the observed difference in land cover and vegetation found within the riparian region, as bare soil is dominant at site 1 and vegetation at site 2.

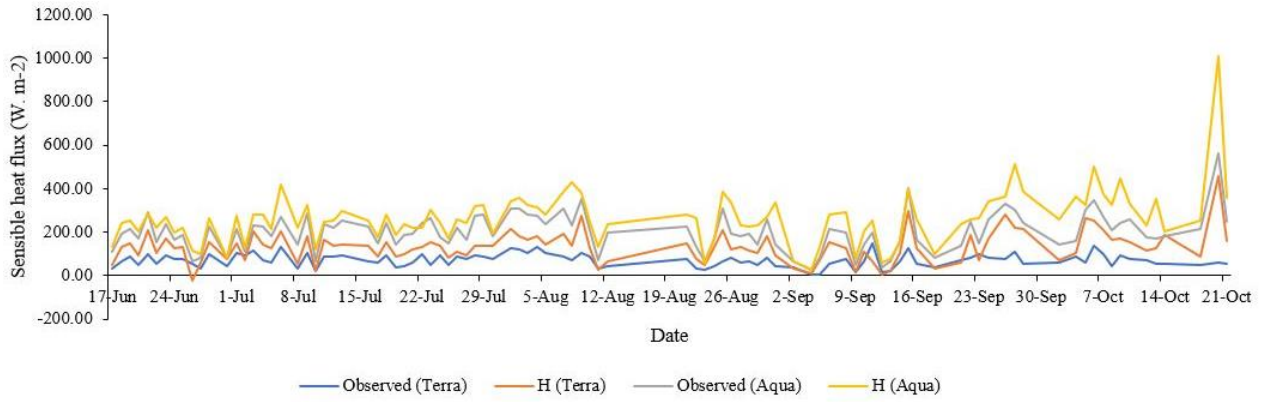


Figure 4.7 A time series comparison of observed and simulated H values during the 2015 measurement period, where the observed data is the *in-situ* H value at the instantaneous overpass time

Sensible heat flux (H) (W. m^{-2}), is the heat flux which heats the air above the soil and plant canopy surfaces and occurs as a result of the difference in temperatures between the surface and the air above (Mengistu, 2008). The H parameter is calculated in the SEBS model independently of the other surface energy balance terms, using wind speed, surface temperature, roughness lengths for heat and momentum transfer and the temperature at the reference height. Van der Kwast *et al.* (2009) stated that the SEBS estimates are less comparable to flux estimates, when the measurement footprint covers multiple land cover types. The SEBS model underestimates H , a phenomenon that usually occurs at high sensible heat flux rates when utilising one source models (Kustas *et al.*, 1996; Huntingford *et al.*, 2000).

The SEBS derived ET_a depends on air temperature (T_a) and land surface temperature (T_o). The sensitivity of H to the $T_o - T_a$ gradient was reported by Su (2002), and Badola (2009) stated that the SEBS model was most sensitive to the $T_o - T_a$ gradient. The land surface temperature variable assists in the determination of R_n and G , and its main contribution includes the aerodynamic resistance in the calculation of H . Lu *et al.* (2013) states that the main factors for the underestimation of H in SEBS and the overestimation of EF , results from the overestimation of ET_a , which could be produced due to the lack of closure of the energy balance, the underestimation of $R_n - G$, the incorrect calculation of aerodynamic parameters and the various land covers in a MODIS pixel.

The quantity of bare soil at a study site significantly impacts the available energy for the sensible and latent heat transfer (Huang *et al.*, 2015). The poor performance of satellite-based ET_a estimation models can largely be attributed to their inability to account for the influence

of soil moisture availability, land surface temperature (*LST*) and physical characteristics of vegetation during the estimation of fluxes (Gokmen *et al.*, 2012; Pardo *et al.*, 2014; Long *et al.*, 2014; Li *et al.*, 2015; Huang *et al.*, 2015). The effect of soil moisture and vegetation fluxes, are included in input variables, disregarding the direct impact on ET_a estimates (Gokmen *et al.*, 2012; Long *et al.*, 2014; Huang *et al.*, 2015, Dziki *et al.*, 2019).

The T_o-T_a gradient is used in the estimation of H , and H is inversely proportional to ET_a (Gibson *et al.*, 2013). The SEBS model was implemented using satellite-derived input variables derived from MODIS Terra and Aqua imagery, respectively. The simulated fluxes were compared against observed fluxes to quantify the influence of the temperature gradient on the modelled estimates. Gibson *et al.* (2013) states that as a result of the diverse meteorological conditions and the differences in T_o-T_a due to the differential heating of the land surface and air, variations and uncertainties would be observed within the simulated and observed flux estimates. The variation of T_o affects the key factors of H , and the temperature gradient between the surface and the atmosphere (Brenner *et al.*, 2017). As a result of the difference in heating of the land differs to the heating of the air, and therefore T_o-T_a , a lag effect occurs, and the time of day of image acquisition may be important and the choice of satellite sensor (MODIS Terra or Aqua) utilised.

Preceding studies have stated that there is uncertain characterisation of the kB^{-1} factor in water stressed and in sparse vegetation cover environments (Gokmen *et al.*, 2012; Gibson, 2013; Paul *et al.*, 2014; Bhattarai *et al.*, 2018; Khand *et al.*, 2019). Chirouze *et al.* (2014) states that the underestimation of H possibly occurs as a result of the overestimation of the kB^{-1} factor at low LAIs. Overestimating the kB^{-1} factor in these environmental conditions would result in an overestimation of Z_{oh} , therefore underestimating H and subsequently overestimating ET_a (Gokmen *et al.*, 2012). According to Khand *et al.* (2019), a common source of error in estimating ET_a from satellite imagery results from cloud cover. A layer of cloud or shaded area owing to cloud presence over nearby pixels may result in an underestimation of LST and consequently, overestimation of ET_a . Studies have shown that a minor bias in LST can significantly influence H and eventually ET_a (Khand *et al.*, 2019).

4.1.4 Latent heat flux

The SEBS model was shown to overestimate LE when compared against the *in-situ* measurements for both MODIS Terra and Aqua imagery, as shown in Table 4.4. Comparisons

between the SEBS derived MODIS Terra LE estimate (LE_{Terra}) and the SEBS derived MODIS Aqua LE estimate (LE_{Aqua}) estimate, against the observed LE data yielded a RVE of -47.57% and -84.34%, respectively. This indicates a greater overestimation of LE_{Aqua} estimates, when compared to the observed LE . The correlation between the data was 0.61 and 0.52 for the LE_{Terra} and the LE_{Aqua} respectively.

Comparisons between the simulated LE_{Terra} and LE_{Aqua} , against the observed LE data yielded R^2 values of 0.37 and 0.27, respectively. A RMSE difference of 44.09 $W. m^{-2}$ was obtained between LE_{Aqua} and LE_{Terra} . As presented in Table 4.4, the assessment of error in data, was carried out with the use of the MAD statistical metric, and yielded values of 92.83 $mm. d^{-1}$ and 99.33 $mm. d^{-1}$ for LE_{Terra} and LE_{Aqua} estimates, respectively.

Table 4.4 Validation of LE estimates obtained from implementing the SEBS model within the riparian region

	$LE_{in-situ}$	LE_{Terra}
AVERAGE ($mm. d^{-1}$)	159.07	234.75
STD DEV	128.42	130.19
RMSE ($W. m^{-2}$)	136.59	
RVE (%)	-47.57	
MAD ($mm. d^{-1}$)	92.83	
PEARSON CORRELATION	0.61	
R^2	0.37	

	$LE_{in-situ}$	LE_{Aqua}
AVERAGE ($mm. d^{-1}$)	158.93	292.97
STD DEV	119.85	127.40
RMSE ($W. m^{-2}$)	180.68	
RVE (%)	-84.34	
MAD ($mm. d^{-1}$)	99.33	
PEARSON CORRELATION	0.52	
R^2	0.27	

According to Mengistu (2008) and Gibson (2013), the correctness of LE is dependent on the accuracy of R_n , G_o and H assuming energy balance closure. From Figure 4.8 and Figure 4.9, it can be seen that there is a greater overestimation of LE for both LE_{Terra} and LE_{Aqua} from August 21st until October 21st 2015. However, both LE_{Terra} and LE_{Aqua} usually follow a similar trend as the *in-situ* data. In environments that contain sparsely vegetated surfaces, such as arid and semi-arid environments, single-source models may yield large errors in estimating terrestrial flux estimates (Cleugh *et al.*, 2007; Li *et al.*, 2019).

The underestimation of H , could have resulted in an overestimation of LE_{Terra} and LE_{Aqua} values, resulting from decreased soil moisture, and an increase in the ability of evaporation over sparse vegetation cover (Zhuang and Wu, 2015). According to Roxy *et al.* (2014), the increased LE estimates result from a high LST and reduced relative humidity. A greater difference between simulated and observed LE estimates, has an impact on the remainder of

the calculations carried out in the SEBS model, resulting in an increased EF , resulting in an overestimation of ET_a .

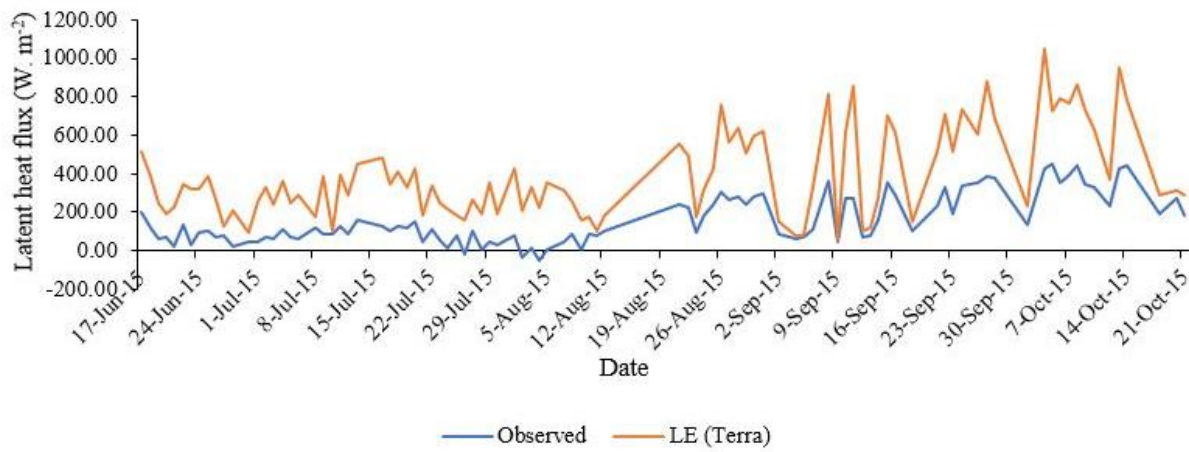


Figure 4.8 A time series comparison of LE_{Terra} estimates obtained from implementing the SEBS model and observed data at the riparian region

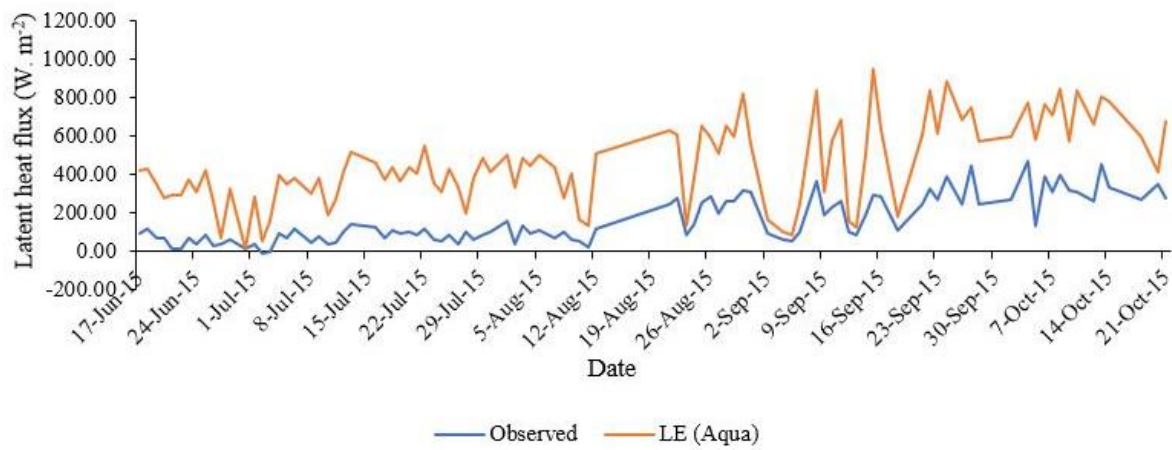


Figure 4.9 A time series comparison of LE_{Aqua} estimates obtained from implementing the SEBS model and observed data at the riparian region

Timmermans *et al.* (2013) and Yi *et al.* (2018) recognized that uncertainties in the estimation of LE using the SEBS model were possible due to the uncertainties obtained for the heat transfer from the incorrect parameterisation of Z_{oh} . The underestimation of H using the SEBS model has been conveyed by (McCabe and Wood, 2006; Chirouze *et al.*, 2014; Ma *et al.*, 2014), especially for bare soil and sparse vegetation environments, resulting in an overestimation of LE . The difference between Z_{om} and Z_{oh} is described by the kB^{-1} factor. The SEBS model is

sensitive to the Z_{oh} or kB^{-1} factor, and consequently, differences in heat flux estimates under diverse treatments of roughness length for heat transfer occur (Gao and Long, 2008).

According to Li *et al.* (2019), the estimation of the spatial and temporal distribution of ET_a and LE is important for monitoring ecosystem health, and in improving water resources management in arid and semi-arid environments (Dinpashoh, 2006). Gibson *et al.* (2011) emphasised the importance of the selection of the satellite sensor being used, and therefore the pixel resolution and heterogeneity of the study area, as the uncertainties obtained are reflected in the estimation of ET_a . Huang *et al.* (2015) states that the SEBS model overestimates ET_a in water limited conditions, whilst Pardo *et al.* (2014) and Gokmen *et al.* (2012) note that the overestimation of EF and LE in the SEBS model is higher, when the soil is dry and there is a reduced amount of vegetation cover. Although LE is mainly affected by soil moisture, surface temperature is also an important factor to consider (Xu *et al.*, 2011). As SEBS does not calculate LE as the energy balance residual, but by using the EF , this may have influenced the increase in the LE estimate (Timmermans *et al.*, 2013).

4.2 Analysis of the Actual Evapotranspiration Estimates

A comparison of ET_a estimates obtained from implementing the SEBS model and *in-situ* measurements at the riparian region are presented in Table 4.5. The SEBS model was shown to overestimate ET_a when compared against the *in-situ* measurements, as comparisons between ET_{Terra} and ET_{Aqua} against the observed ET_a data yielded a RVE of -123.04% and -159.41%, respectively. This indicates an overestimation of both simulated ET_a estimates, but a greater overestimation of ET_{Aqua} , when compared to the observed ET_a , as seen in Table 4.5 and Figure 4.11.

The comparison between ET_{Terra} and ET_{Aqua} against the observed ET_a data yielded Pearson correlation values of 0.63 and 0.59, respectively. Whilst R^2 values of 0.40 and 0.34 were obtained for ET_{Terra} and ET_{Aqua} , respectively. A RMSE difference of 0.65 mm. d⁻¹ was obtained between ET_{Aqua} and ET_{Terra} when compared against observed ET_a data. As presented in Table 4.5, the MAD statistical metric yielded values of 0.96 mm. d⁻¹ and 1.11 mm. d⁻¹ for ET_{Terra} and ET_{Aqua} estimates, respectively. A Kruskal Wallis test was carried out for both ET_{Terra} and ET_{Aqua} estimates, and the p-values obtained indicated a significant difference between the simulated and *in-situ* ET_a estimates.

Table 4.5 Validation of ET_a estimates obtained from implementing the SEBS model within the riparian region

	$ET_{in-situ}$	ET_{Terra}	ET_{Aqua}
AVERAGE (mm. d⁻¹)	1.82	4.06	4.72
STD DEV	1.24	1.59	1.69
RMSE (mm. d⁻¹)		2.56	3.21
RVE (%)		-123.04	-159.41
MAD		0.96	1.11
PEARSON CORRELATION		0.63	0.59
R²		0.40	0.34
KRUSKAL WALLIS TEST		5.07×10^{-18}	1.66×10^{-22}

From Figure 4.10, it can be seen that majority of the points are located above the 1:1 line, indicating an overestimation of ET_a estimates obtained from implementing the SEBS model within the riparian region, which was analysed in Table 4.5. The degree of overestimation is higher at the lower value range. During drier periods ET_a is low, and the satellite-based estimates are unable to account for the influence of water availability and subsequently ET_a is overestimated.

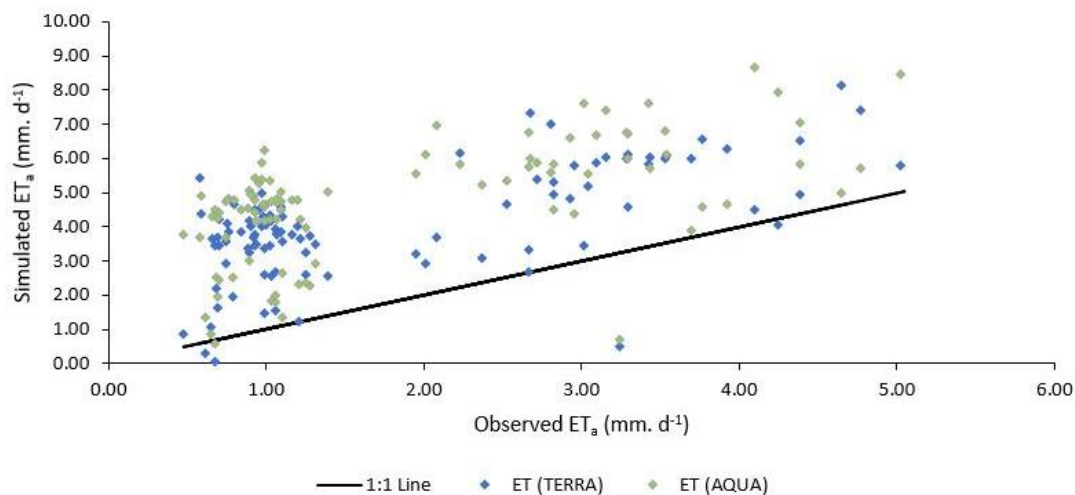


Figure 4.10 A comparison of ET_a estimates obtained from implementing the SEBS model and observed data at the riparian region

From Figure 4.11, it can be seen that there is a significant overestimation of ET_a for both ET_{Terra} and ET_{Aqua} from August 21st until October 21st 2015. However, both ET_{Terra} and ET_{Aqua} generally follow a similar trend as the *in-situ* data. Results from study site 1 is more strongly influenced by bare soils, water limitations and atmospheric effects, whereas results from study site 2 within the riparian region is influenced by climatic conditions, as there is much more

vegetation found in this region. Seasonal and climatic changes also influence stress conditions, which may have contributed to the increased vegetation cover at site 2. According to Gokool *et al.* (2017), the soil water availability along the section of the river that was observed, was affected by the drought. Therefore, variations occurred in vegetation and canopy cover, and soil moisture status between site 1 and site 2, resulting in a greater overestimation of ET_a at site 2.

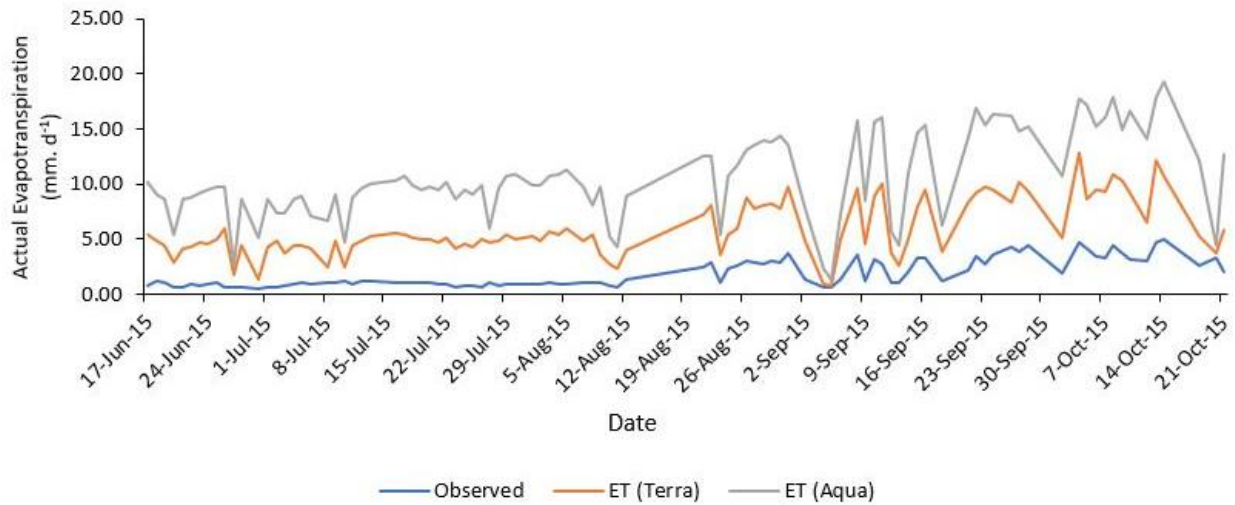


Figure 4.11 A time series comparison of ET_a estimates obtained from implementing the SEBS model and observed data at the riparian region

In this study, the SEBS derived ET_a was assessed using a $\pm 30\%$ threshold (Kalma *et al.*, 2008). Therefore, each observation in the *in-situ* dataset was increased and decreased by 30%, resulting in these values being utilised as the upper and lower thresholds, respectively. Although ET_{Terra} yielded a lower RVE than the ET_{Aqua} when compared against *in-situ* data, (Figure 4.12), only 7.22% and 8.25% of the simulated data from ET_{Terra} and ET_{Aqua} data respectively, were located within the 30% threshold accuracy range.

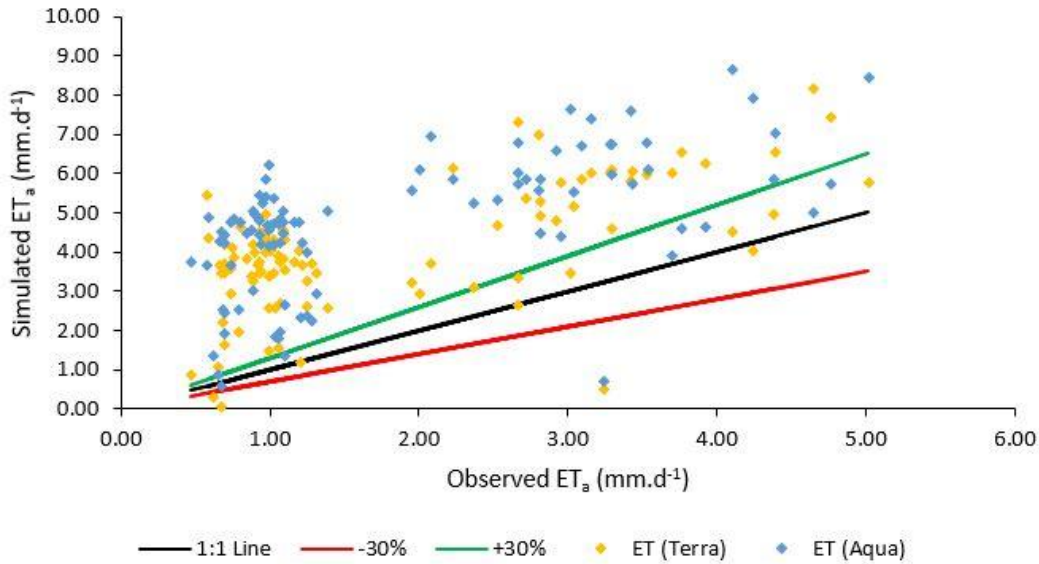


Figure 4.12 Simulated ET_a estimates obtained within an acceptable accuracy range (AAR) of $\pm 30\%$

Overall, SEBS was shown to largely overestimate ET_a when compared against the *in-situ* measurements, with the ET_{Terra} overestimating to a lower degree than the ET_{Aqua} estimate at the riparian region. Inconsistencies in the results can be attributed to the distance between the meteorological station and the EC system, and a difference in spatial scales representative of SEO and *in-situ* data among others. As the spatial resolution of MODIS is 1 km, there is possibility of the other landcovers influencing the ET_a estimate. Variations in environmental conditions during the study period, such as seasonal and climatic changes from winter to summer may have also influenced the ET_a and terrestrial flux estimates. The retrieval of reliable data from EC stations is still a challenge, and is affected by multiple factors, such as the lack of energy balance closure, the presence of vegetation in the field that is not being studied and the distributions of representative source areas, which are among the few that result in an uncertainty in the measurement of ET_a (Sun *et al.*, 2019). The ET_{Terra} and ET_{Aqua} estimates seem unrealistic to obtain, however the observed ET_a estimate is realistic, as the study was carried out during a drought period, hence producing low values of ET_a .

According to Huang *et al.* (2015), the SEBS model overestimates ET_a in water limited conditions, whilst Pardo *et al.* (2014) and Gokmen *et al.* (2012) noted that the overestimation of the EF and LE in the SEBS model is higher, when the soil is dry and there is a reduced vegetation cover. Therefore, the soil moisture and the amount of exposed bare soil had an

impact on the overall estimated ET_a value. Consequently, the SEBS calculated ET_a was significantly higher than the *in-situ* ET_a estimates.

A comparison of ET_a estimates obtained from implementing the SEBS model and *in-situ* at the savanna region are presented in Table 4.6. The SEBS model was shown to overestimate ET_a when compared against the *in-situ* measurements, as comparisons between ET_{Terra} and ET_{Aqua} against the observed ET_a data yielded a RVE of -437.80% and -512.04%, respectively. This indicates an overestimation of both simulated ET_a estimates, but a greater overestimation of ET_{Aqua} estimates, when compared to the observed ET_a , as seen in Table 4.6 and Figure 4.14.

The comparison between ET_{Terra} and ET_{Aqua} against the observed ET_a data yielded Pearson correlation values of 0.30 and 0.39, respectively. Whilst R^2 values of 0.09 and 0.15 were obtained for ET_{Terra} and ET_{Aqua} , respectively. A RMSE difference of 0.59 mm. d⁻¹ was obtained between ET_{Aqua} and ET_{Terra} against observed ET_a data. As presented in Table 4.6, the MAD statistical metric yielded values of 1.14 mm. d⁻¹ and 1.18 mm. d⁻¹ for ET_{Terra} and ET_{Aqua} estimates, respectively. A Kruskal Wallis test was carried out for both ET_{Terra} and ET_{Aqua} estimates, and the p-values obtained indicated a significant difference between the simulated and *in-situ* ET_a estimates.

Table 4.6 Validation of ET_a estimates obtained from implementing the SEBS model within the savanna region

	$ET_{in-situ}$	ET_{Terra}	ET_{Aqua}
AVERAGE (mm. d⁻¹)	0.77	4.16	4.27
STD DEV	0.57	1.51	1.73
RMSE (mm. d⁻¹)		3.68	4.27
RVE (%)		-437.80	-512.04
MAD (mm. d⁻¹)		1.14	1.18
PEARSON CORRELATION		0.30	0.39
R²		0.09	0.15
KRUSKAL WALLIS TEST		2.62 x 10 ⁻²⁷	1.65 x 10 ⁻²⁷

The majority of the points are located above the 1:1 line, as depicted in Figure 4.13, indicating a significant overestimation of ET_a estimates obtained from implementing the SEBS model within the savanna region, which was analysed in Table 4.6. A higher degree of overestimation of ET_a was observed at the lower value range. During drier periods ET_a is low, however satellite-based estimates are unable to account for the influence of water availability and subsequently ET_a is overestimated (Dzikiti *et al.*, 2019).

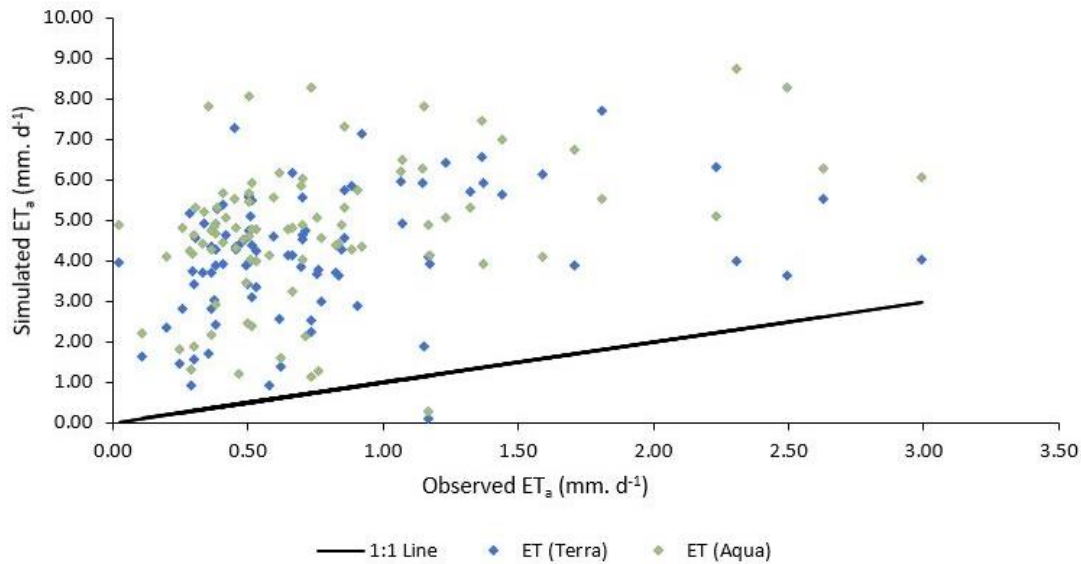


Figure 4.13 A comparison of ET_a estimates obtained from implementing the SEBS model and *in-situ* data at the savanna region

From Figure 4.14, there is a greater overestimation of ET_{Aqua} estimates when compared to observed values. However, both ET_{Terra} and ET_{Aqua} follow a similar trend as the *in-situ* data. The savanna region is influenced by environmental and climatic conditions, such as land cover, bare soils, water limitations and atmospheric effects.

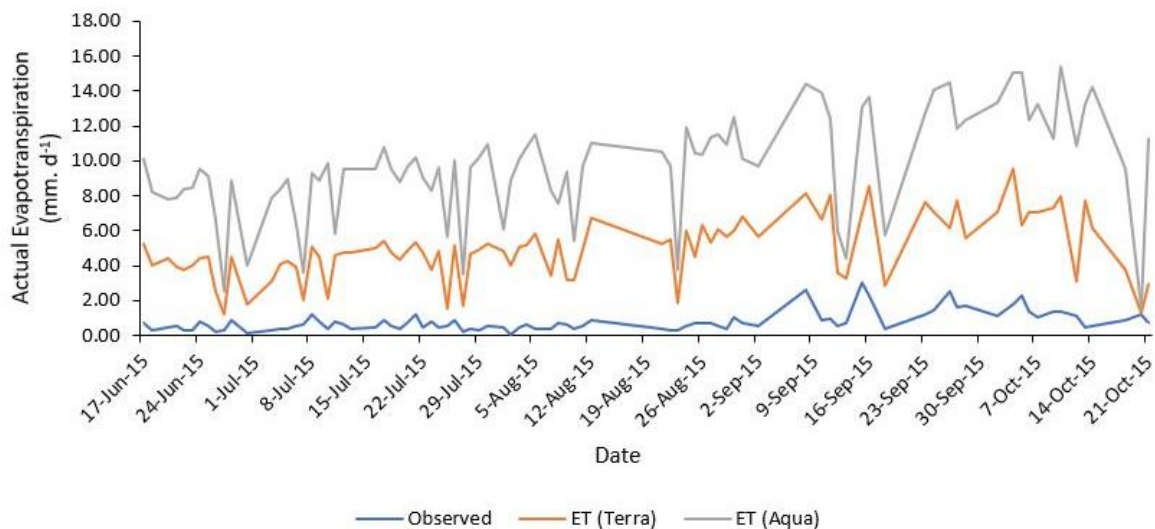


Figure 4.14 A time series comparison of ET_a estimates obtained from implementing the SEBS model and observed data at the savanna region

The only results that were analysed for the Malopeni study site (savanna region), was the comparison of the satellite derived ET_a with the observed (*in-situ*) ET_a . This resulted from the

in-situ flux estimates undergoing a quality control procedure, to remove erroneous data. However, the dataset resulted in, inconsistent and large amounts of missing data.

The SEBS model was shown to overestimate ET_a when compared against the *in-situ* measurements. Whilst the ET_{Terra} data overestimated to a lower degree than the ET_{Aqua} estimates. An overestimation of ET_a could have resulted from the SEBS model ineffectively accounting for the influence of soil moisture (Gokmen *et al.*, 2012; Gibson *et al.*, 2013; Yi *et al.*, 2018). It should be noted that the study period coincided with a large El Niño induced drought (Kogan and Guo, 2016; Gokool *et al.*, 2017).

The SEBS derived ET_a depends on air temperature (T_a) and land surface temperature (T_o). The sensitivity of H to the $T_o - T_a$ gradient was reported by Su (2002), and Badola (2009) stated that the SEBS model was most sensitive to the $T_o - T_a$ gradient. The land surface temperature parameter assists in the determination of Rn and G , and its main contribution includes the aerodynamic resistance in the calculation of H . Lu *et al.* (2013) states that the main factors for the underestimation of H in SEBS and the overestimation of EF , which results in the overestimation of ET_a include; the lack of closure of the energy balance, the underestimation of $Rn - G$, the incorrect calculation of aerodynamic parameters and the various land covers in a MODIS pixel.

Higher ET_a values are usually related with warm, dry conditions (Gush, 2016). The SEBS model does not particularly consider soil moisture and biophysical factors when estimating terrestrial fluxes, as it is included in the input variables, and does not consider the immediate influence on ET_a approximations (Gokmen *et al.*, 2012; Huang *et al.*, 2015). The extent of exposed soil affects the amount of energy that is accessible for sensible and latent heat transfer (Huang *et al.*, 2015). According to Gokmen *et al.* (2012) and Pardo *et al.* (2014), the overestimation of EF and LE in SEBS is higher, due to the lack of vegetation cover and drier soils.

Both the ET_{Terra} and ET_{Aqua} estimates performed poorly when compared to *in-situ* ET_a estimates. The poor correlation was largely attributed to the inability of the SEBS model to adequately account for the influence of soil moisture, LST and biophysical parameters during the derivation of surface fluxes (Gokmen *et al.*, 2012; Pardo *et al.*, 2014; Gibson *et al.*, 2013; Huang *et al.*, 2015; Yi *et al.*, 2018). Subsequently, the SEBS model tends to overestimate the EF and LE parameters for environments experiencing water stress, which results in an

overestimation of ET_a . The influence of soil moisture and vegetation fluxes, are indirectly included in input variables, disregarding their direct impact on ET_a estimates. A study carried out by Wagle *et al.* (2017) discussed that the SEBS model substantially overestimated ET_a during dry conditions, and the model's performance improved with an increase in soil moisture. This result is further supported by the overestimation of LE during the partitioning of available energy by SEBS during non-rainy days.

The inconsistencies seen in the data can be attributed to the distance between the meteorological station and the EC system. At the savanna region, no solar radiation values were recorded. As a result, solar radiation values were obtained from the riparian region and used as inputs into the SEBS model for the savanna region. Tang *et al.* (2011) states that overestimations and uncertainties may arise as a result of different spatial scales representative of satellite earth observed and *in-situ* data, respectively. As the spatial resolution of MODIS is 1 km, there is a possibility of other landcovers influencing the ET_a estimate. Variations in environmental conditions during the study period, resulting from seasonal and climatic changes from winter to summer may have also influenced the ET_a and flux estimates.

Preceding studies have stated uncertain characterisation of the kB^{-1} factor in water limited and in sparse vegetation cover environments (Gokmen *et al.*, 2012; Gibson, 2013; Paul *et al.*, 2014; Bhattarai *et al.*, 2018; Khand *et al.*, 2019). According to Gokmen *et al.* (2012), application of the modified SEBS formulation can improve the estimation of energy and water fluxes, in water-stressed regions. Zhuang *et al.* (2016) states that the kB^{-1} factor has the ability to correct the differences between radiometric and atmospheric temperature and is influenced by numerous variables that relate to structural parameters and environmental conditions.

Days that have a large difference between radiometric and atmospheric temperature, may occur as a result of the T_o-T_a gradient. The LST estimate is influenced by the shortened energy balance equation, due to the incoming and outgoing radiation, and spatially distributed ET_a estimates are based on manipulating LST information obtained from thermal infrared remote (TIR) sensing located on satellite or airborne platforms (Brenner *et al.*, 2017). Other sources of uncertainty include the satellite overpass times of the MODIS Terra and Aqua imagery, the atmospheric correction factor and the estimation of the water vapour content. As a result of the satellite overpass times, and the imagery being obtained at different times, differences in ET_a and terrestrial flux estimates may occur. This may have resulted from the temperature gradient, which influences ET_a and terrestrial flux estimates.

The SEBS model is highly complex, and a combination of several minor factors may result in the overestimation of ET_a and terrestrial flux estimates. According to Kalma *et al.* (2008), the temperature gradient and land surface temperature impact LE , R_n , G_o and H , which are components of the energy balance equation. The errors related with utilising surface temperature to estimate H , include; errors in observed meteorological data, errors in model assumption and the significant inaccuracies in radiometric temperature estimation and the inequality between radiometric and aerodynamic surface temperature (Kalma *et al.*, 2008).

Satellite earth observation data have effectively been used to estimate the spatial distribution of the available energy from combined visible and TIR data, and the spatial distribution of H from thermal data (Troufleau *et al.*, 1997). The H variable is usually related to the gradient between the land surface temperature and air temperature divided by an aerodynamic resistance.

4.2.1 Evaluation of the MOD16 product and the aggregated SEBS derived ET_a estimates

The SEBS model was implemented using satellite-derived input variables derived from MODIS Terra and Aqua imagery, respectively. The simulated fluxes and ET_a were compared against observed ET_a measurements, to quantify the influence of the temperature gradient on the modelled estimates. In order to further gauge, the influence which the model conceptualisation has on the accuracy of the estimates, the MOD16 product was acquired and evaluated as part of these investigations. The rationale for this can be attributed to the absence of the temperature data used during the derivation of ET_a when using the MOD16 algorithm.

Satellites are able to provide information when ET_a estimates are needed at high spatio-temporal resolutions. However, there still exists an influence of the land surface and air temperature gradient on ET_a and terrestrial flux estimates derived using satellite earth observed data. In recent years, numerous global products and datasets derived from SEO, has been made available for public and private use. The $ET_{MOD16A2}$ data was acquired and evaluated for the riparian and savanna region, and the 8-day aggregated ET_{Terra} and ET_{Aqua} for each region was obtained, to determine the accuracy of each method used. An example of the sample code that was used to extract $ET_{MOD16A2}$ data from the MOD16A2 product for the Malopeni site (savanna region) is depicted in Figure 7.1, in Appendix A.

A comparison of aggregated 8-day ET_a estimates obtained from implementing the SEBS model and *in-situ* measurements at the riparian region are presented in Table 4.7. The SEBS model

was shown to overestimate ET_a when compared against the *in-situ* measurements, as comparisons between ET_{Aqua} against the observed ET_a data yielded a RVE of -159.39%. Whilst the $ET_{MOD16A2}$ yielded a RVE of 50.36%, indicating an underestimation of ET_a .

The comparison between ET_{Terra} , ET_{Aqua} and $ET_{MOD16A2}$ against the 8-day aggregated observed ET_a data yielded R^2 values of 0.39, 0.34 and 0.16, respectively. As presented in Table 4.7, the MAD statistical metric yielded values of 5.11 mm. 8d⁻¹, 5.42 mm. 8d⁻¹ and 6.01 mm. 8d⁻¹ for the ET_{Terra} , ET_{Aqua} and $ET_{MOD16A2}$ estimates, respectively. A Kruskal Wallis test was carried out for the ET_{Terra} , ET_{Aqua} and ET_{MOD16} estimates, and the p-values obtained indicated a significant difference between the simulated and *in-situ* ET_a estimates.

Table 4.7 Validation of aggregated 8-day ET_a estimates obtained from implementing the SEBS model within the riparian region

	$ET_{in-situ}$	ET_{Terra}	ET_{Aqua}	$ET_{MOD16A2}$
AVERAGE (mm. 8d⁻¹)	10.90	24.31	28.28	5.41
STD DEV	6.35	8.55	8.74	1.49
RMSE (mm. 8d⁻¹)		14.93	18.73	8.78
RVE (%)		-122.98	-159.39	50.36
MAD (mm. 8d⁻¹)		5.11	5.42	6.01
PEARSON CORRELATION		0.62	0.58	-0.40
R²		0.39	0.34	0.16
KRUSKAL WALLIS TEST		1.64 x 10 ⁻⁴	2.43 x 10 ⁻⁵	2.90 x 10 ⁻³

From Figure 4.15, it can be seen that ET_{Terra} and ET_{Aqua} overestimate ET_a , whilst there is a good correlation between the $ET_{MOD16A2}$ and the *in-situ* ET_a until August 13th. There is a greater overestimation of ET_a for both 8-day aggregated ET_{Terra} and ET_{Aqua} estimates from August 21st until October 21st 2015. However, both ET_{Terra} and ET_{Aqua} generally follow a similar trend as the *in-situ* data. However, the $ET_{MOD16A2}$ was underestimated during this period.

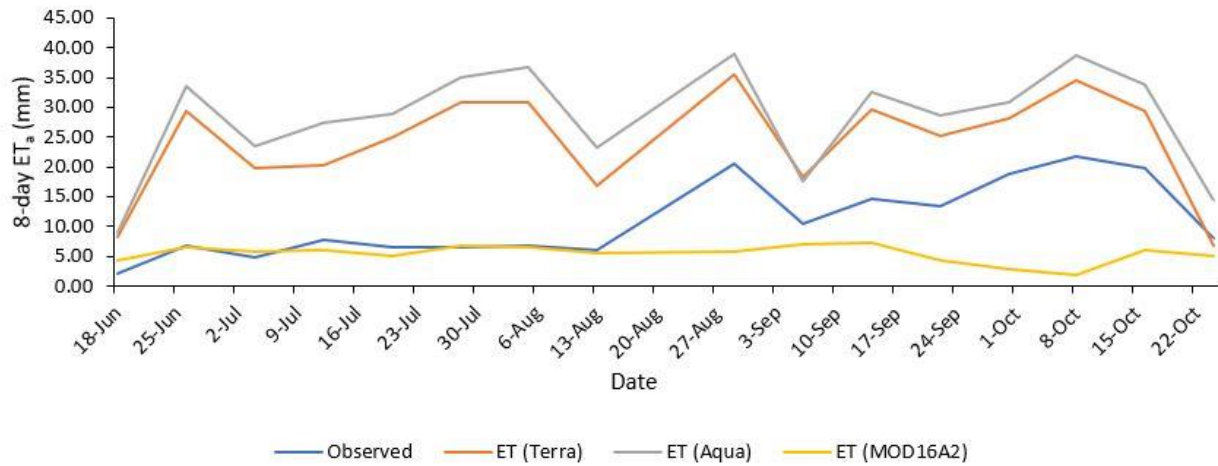


Figure 4.15 A time series comparison of aggregated 8-day ET_a estimates obtained from implementing the SEBS model and *in-situ* data at the riparian region

The various methods to estimate ET_a for the 26th June 2015 are presented in Figure 4.16, with the ET_a estimates depicted in Table 4.8. The ET_{Aqua} estimate is in the least agreement with the *in-situ* ET_a measurement, whilst the MOD16 product has the best agreement with the observed data. The script that was utilised to obtain the $ET_{MOD16A2}$ image is presented in Figure 7.2, in Appendix A.

Table 4.8 A comparison of derived ET_a estimates from various spatial resolutions for Site 1 for 26 June 2015

	Spatial Resolution (m)	8-day ET_a (mm)
<i>In-situ ET_a</i>		6.68
<i>ET_{Terra}</i>	1000	29.36
<i>ET_{Aqua}</i>	1000	33.49
<i>$ET_{MOD16A2}$</i>	500	6.50

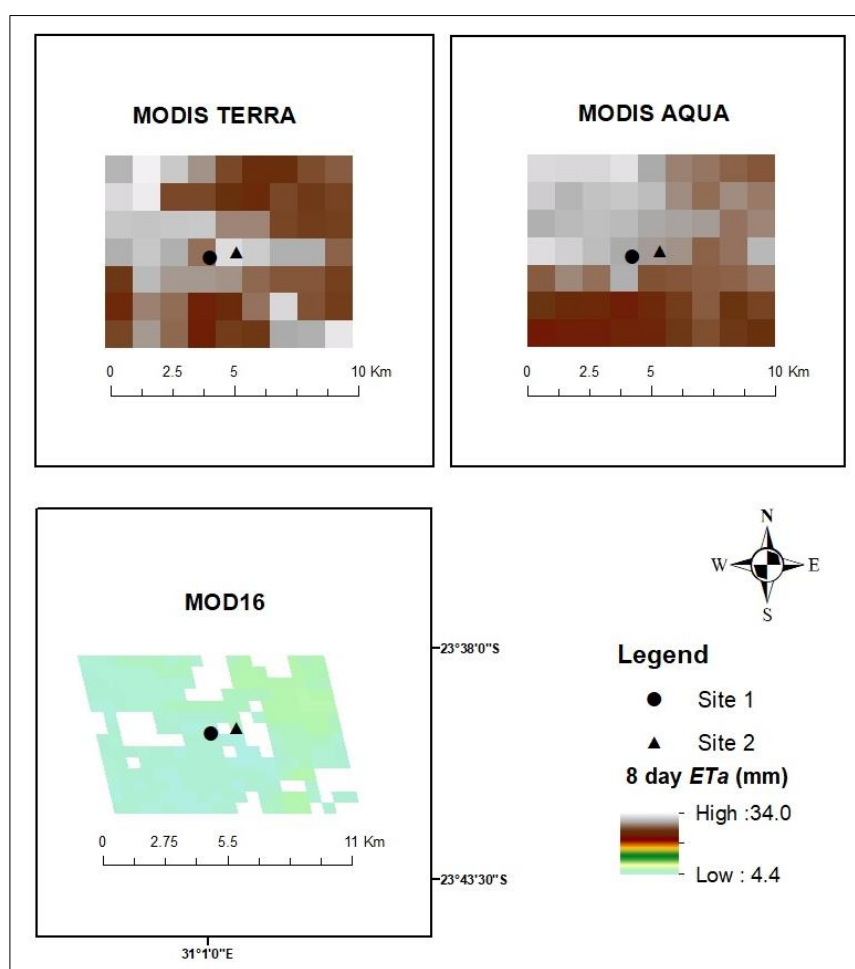


Figure 4.16 A comparison of the MOD16 product and the aggregated 8-day ET_a estimates obtained from implementing the SEBS model for 26 June 2015

A comparison of aggregated 8-day ET_a estimates obtained from implementing the SEBS model and *in-situ* measurements at the savanna region are presented in Table 4.9. The SEBS model was shown to overestimate ET_a when compared against the *in-situ* measurements, as comparisons between ET_{Terra} and ET_{Aqua} against the observed ET_a data yielded a RVE of -159.39% and -492.07%, respectively. Whilst the $ET_{MOD16A2}$ yielded a RVE of 9.46%, indicating an underestimation of ET_a .

The evaluation between ET_{Terra} , ET_{Aqua} and $ET_{MOD16A2}$ against the 8-day aggregated observed ET_a data yielded R^2 values of 0.27, 0.32 and 0.06, respectively. As presented in Table 4.9, the MAD statistical metric yielded values of 7.36 mm. 8d⁻¹, 8.29 mm. 8d⁻¹ and 2.22 mm. 8d⁻¹ for the simulated ET_{Terra} , ET_{Aqua} and $ET_{MOD16A2}$ estimates, respectively. A Kruskal Wallis test was carried out and a p-value of 0.68 was obtained for the $ET_{MOD16A2}$ estimate, indicating no

significant difference between the $ET_{MOD16A2}$ and the *in-situ* ET_a estimates. However, the null hypothesis was rejected for the aggregated 8-day ET_{Terra} and ET_{Aqua} estimates.

Table 4.9 Validation of aggregated 8-day ET_a estimates obtained from implementing the SEBS model within the savanna region

	$ET_{in-situ}$	ET_{Terra}	ET_{Aqua}	$ET_{MOD16A2}$
AVERAGE (mm. 8d⁻¹)	4.01	21.36	23.73	3.63
STD DEV	2.34	10.24	10.72	1.17
RMSE (mm. 8d⁻¹)		19.51	21.78	2.79
RVE (%)		-433.06	-492.07	9.46
MAD		7.36	8.29	2.22
PEARSON CORRELATION		0.52	0.56	-0.25
R²		0.27	0.32	0.06
KRUSKAL WALLIS TEST		6.40×10^{-5}	1.93×10^{-5}	679.18×10^{-3}

The savanna region was analysed from June until October 2015. The daily ET_{Terra} and ET_{Aqua} estimates were aggregated to 8-day ET_a values. From Figure 4.17, an overestimation of the ET_{Terra} and ET_{Aqua} estimates can be seen, whilst the $ET_{MOD16A2}$ underestimates ET_a during the summer months when compared to the *in-situ* ET_a measurements. The ET_{Terra} and ET_{Aqua} estimates generally follow a similar trend to the *in-situ* ET_a measurements.

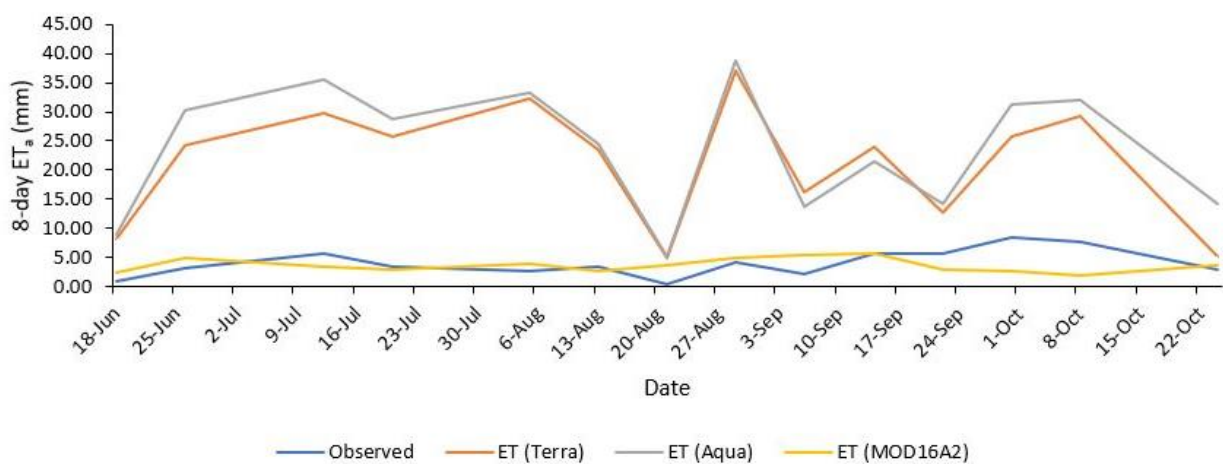


Figure 4.17 A time series comparison of aggregated 8-day ET_a estimates obtained from implementing the SEBS model and *in-situ* data at the savanna region

The various types of land cover at the riparian and savanna regions may have resulted in the underestimation and overestimation of ET_a when using ET_{Terra} , ET_{Aqua} and MOD16 to estimate ET_a . This results from the various landcovers requiring different amounts of water, impacting

the amount of ET_a occurring. When utilising the MOD16 product, an increase in air temperature, resulted in a decrease in the $ET_{MOD16A2}$ estimation. According to Allen *et al.* (1998), an increase in humidity of the air causes a decrease in the ET_a demand, as plants can reduce ET_a in response to increased VPD by closing their stomata (Massmann *et al.*, 2019).

The results indicated an underestimation of the $ET_{MOD16A2}$ estimate, when compared against the observed ET_a data, whilst the ET_{Terra} and ET_{Aqua} overestimated the observed ET_a data. It is apparent that the ET_a values derived from the EC system are higher than the $ET_{MOD16A2}$ values during warmer months and are closely related during colder months (June until mid-August). These results rather match with the results observed by Ramoelo *et al.* (2014).

Aguilar *et al.* (2018) stated that soil moisture influences the aerodynamic or surface resistance of the vegetation and the resistance of the soil surface, which are important parameters in the MOD16 algorithm. Prior model validations of the MOD16 product presented comparable underestimations of ET_a in sparse natural vegetation, namely; crops (Rodriguez, 2016), savanna (Mu *et al.*, 2007) and grassland (Chi *et al.*, 2017). The differences could have resulted from the uncertainty of the input variables (LAI or meteorological data) (Aguilar *et al.*, 2018).

The MOD16 product does not account for disturbance history or species composition and stand age, which could also add further uncertainty (Ramoelo *et al.*, 2014). The algorithm assumes that the stomata close at night, whilst Musselman and Minnick (2000) have stated that the stomata open at night. This results in the underestimation of daily ET_a , due to the bias imposed by transpiration occurring at night (Ramoelo *et al.*, 2014). Ramoelo *et al.* (2014) also states that the MOD16 is generally poor and the accuracy is inconsistent over a period in selected savanna ecosystem sites. According to Hu *et al.* (2015), the best performance of the MOD16 product is observed in forested areas, whilst poorer performances are detected in arid and polar climates.

The discrepancies in the SEBS derived ET_a may have resulted from the spatio-temporal resolution of the MODIS Terra and Aqua imagery, as the correctness of the satellite products vary in space and time. The meteorological data that was utilised for the SEBS modelling was obtained from two EC systems, and each system collected meteorological data over different land cover and vegetation types. The differences between the $ET_{MOD16A2}$ and the *in-situ* ET_a estimates could be as a result of multiple factors such as; the flux tower footprint, the MODIS Terra, MODIS Aqua and MOD16 pixel size, remote sensing data and *in-situ* data. The EC

system instruments are also susceptible to errors in measurement through factors such as, malfunctioning instrumentation and errors in sensor configuration, and it also limited by regions of low wind speed (Spittlehouse and Black, 1980). The factors influencing the *in-situ* data may have affected the accuracy of the simulated results. According to Hartanto *et al.* (2017) other factors that may influence the accuracy of results obtained include; atmospheric conditions, the region of interest and local surface conditions.

5. CONCLUSION AND RECOMMENDATIONS

The conclusions and recommendations derived from this research study are discussed in this chapter.

5.1 Conclusion

South Africa is considered as a semi-arid and water-scarce country, and global climate change has placed further strain on its limited water resources. It is imperative to understand all processes of the hydrological cycle in detail, as it has a vital influence on water resources management.

Several methods have been developed to account for ET_a in the hydrological cycle at different spatial and temporal scales, with micro-meteorological methods being amongst the most frequently applied approaches. Despite the successful application of these techniques to develop an improved understanding of water and energy fluxes, they are limited in their ability to provide spatially representative information for large geographic extents and are expensive to use over long periods.

The use of SEO methods and associated technologies have been proposed as a suitable alternative to conventional ET_a estimation methods, largely due to their ability to capture spatially and temporally explicit hydrological process information, particularly in poorly gauged environments. However, it is important to take cognisance of the limitations associated with the satellite-based models and associated data sets prior to utilising these data sources and tools to guide decision making, as this ultimately influences the success of their intended use. Previous studies have successfully demonstrated how satellite-based energy-balanced ET models can provide fairly accurate estimates of terrestrial fluxes and ET_a . However, it has also been shown that these models have the tendency to perform poorly in water stressed environments due to an inherent limitation in their conceptualisation which relates to the temperature gradient ($T_o - T_a$). Given this limitation, the study aimed to establish whether the selection of an image based upon the satellite overpass time would influence the accuracy of the modelled flux and ET_a estimates, as this is closely linked to the dynamic nature of the temperature gradient.

The SEBS model was implemented using satellite-derived input variables derived from MODIS Terra and Aqua imagery, respectively. The simulated fluxes and ET_a were then compared against observed ET_a to quantify the influence of the temperature gradient on the modelled estimates. The SEBS derived ET_a estimates indicated that both the ET_{Terra} and ET_{Aqua} largely overestimated *in-situ* ET_a measurements. After the evaluation of the individual terrestrial fluxes, the SEBS estimated Rn compared favourably with the *in-situ* estimates for both MODIS Terra and Aqua data. However, the Rn_{Aqua} results performed better than the Rn_{Terra} estimates. The Go_{Aqua} estimate correlated better than the Go_{Terra} estimate to the *in-situ* data. The H_{Terra} and H_{Aqua} estimates showed no agreement with the *in-situ* results. Overall, the SEBS derived MODIS Aqua estimates compared favourably with the *in-situ* estimates, as compared to the MODIS Terra estimates.

The simulated Rn overestimated the *in-situ* Rn estimates. This could have resulted from the difference in the spatial and temporal scale of the measurements, that are observed by the field instruments and the MODIS sensors. The different satellite overpass times has an influence on the ET_a and terrestrial flux estimates obtained, which may have resulted from the T_o-T_a gradient. As a result of the diverse meteorological conditions and the differences in T_o-T_a due to the differential heating of the land surface and air, variations and uncertainties are observed within the simulated and *in-situ* terrestrial flux estimates, as a lag effect occurs. Therefore, promoting the importance of the time of day of image acquisition and the correction selection of the satellite sensor (MODIS Terra or Aqua) being utilised.

Regions consisting of sparse vegetation, are influenced by the amount of radiation reaching the soil and is highly dependent on the geometry of the sun and leaf orientations. The soil moisture and the amount of exposed bare soil has an impact on Go measured at the study sites. The SEBS model overestimates ET_a in water limited conditions, and the overestimation of the EF and LE in the SEBS model is higher, when the soil is dry and there is a reduced amount of vegetation cover. The direct soil evaporation component of ET_a is large, as there are vast areas of bare soil within the study sites, and the SEBS model is more sensitive to surface soil temperature than the surface aerodynamic parameters and has been confirmed in earlier studies.

Both H_{Terra} and H_{Aqua} estimates were underestimated when compared to *in-situ* data. Several single-source models, such as the SEBS model underestimates H especially for bare soil and sparse vegetation environments. This resulted in an overestimation of LE , which occurred from a decrease in soil moisture, and an increase in the ability of evaporation and sparse vegetation

cover. Discrepancies obtained within the results may influence the remainder of the calculations carried out in SEBS, resulting in an increased EF and an overestimation of ET_a .

Increased LE estimates result from a high LST and reduced relative humidity. As SEBS does not calculate LE as the energy balance residual, but using the EF , this results in an increased LE . Earlier studies have stated uncertain characterisation of the kB^{-1} factor in water stressed and in sparse vegetation cover environments. The underestimation of H possibly occurs as a result of the overestimation of the kB^{-1} factor at low LAIs. Overestimating the kB^{-1} factor in these environmental conditions would result in an overestimation of Z_{oh} , therefore underestimating H and subsequently overestimating ET_a . The SEBS model is sensitive to the Z_{oh} or kB^{-1} factor, consequently differences in heat flux estimates under diverse treatments of roughness length for heat transfer occur. Studies have shown that a minor bias in LST can significantly influence H and eventually ET_a . Although LE is largely influenced by soil moisture, surface temperature is also an important factor to consider. Application of the modified SEBS formulation can improve the estimation of energy and water fluxes, in water-stressed regions.

The SEBS model is highly complex, and a combination of several minor factors may result in the overestimation of ET_a and terrestrial flux estimates. The temperature gradient and land surface temperature impact LE , R_n , Go and H , which are components of the energy balance equation. Overall, results showed that the SEBS derived ET_a were largely overestimated. Inconsistencies in the results can be attributed to the distance between the meteorological station and the EC system, and a difference in spatial scales representative of SEO and *in-situ* data, among a few. Variations in environmental conditions during the study period, such as seasonal and climatic changes from winter to summer influenced the ET_a and terrestrial flux estimates, as the study period coincided with a large El Niño induced drought.

Higher ET_a values are usually related with warm, dry conditions. The extent of exposed soil affects the amount of energy that is accessible for sensible and latent heat transfer. Both the ET_{Terra} and ET_{Aqua} estimates performed poorly when compared to *in-situ* ET_a estimates at the savanna region. The poor correlation was largely attributed to the SEBS model being unable to adequately account for the influence of soil moisture, LST and biophysical parameters during the derivation of surface fluxes. The influence of soil moisture and vegetation fluxes, are indirectly included in input variables, ignoring their direct impact on ET_a estimates.

The alternate hypothesis stating that the gradient between land surface and air temperature significantly influences the accuracy of satellite-derived ET_a and terrestrial flux estimates is accepted. As days that have a large difference between radiometric and atmospheric temperature, may occur as a result of the T_o-T_a gradient. The LST estimate is influenced by the shortened energy balance equation, and spatially distributed ET_a estimates are based on manipulating LST information obtained from thermal infrared remote (TIR) sensing located on satellite or airborne platforms.

Satellites are able to provide information when ET_a estimates are needed at high spatio-temporal resolutions. In recent years, numerous global products and datasets derived from SEO, and have been made available for public and private use. The SEBS model was implemented using satellite-derived input variables derived from MODIS Terra and Aqua imagery, respectively. In order to further gauge, the influence which the model conceptualisation has on the accuracy of the estimates, the $ET_{MOD16A2}$ data was acquired and evaluated. The rationale for this can be attributed to the absence of the temperature data used during the derivation of ET_a using the MOD16 algorithm.

The aggregated 8-day ET_{Terra} and ET_{Aqua} overestimated the observed ET_a measurements, whilst the MOD16 product tends to underestimate ET_a during the summer months when compared to the *in-situ* ET_a . It is apparent that the ET_a values derived from the EC system are higher than the $ET_{MOD16A2}$ values during warmer months and are closely related during colder months (June until mid-August). These results rather match with the results observed by previous studies that have been undertaken.

Soil moisture influences the aerodynamic or surface resistance of the vegetation and the resistance of the soil surface, which are important parameters in the MOD16 algorithm. Prior model validations of the MOD16 product presented comparable underestimations of ET_a in sparse natural vegetation, namely; crops, savanna and grassland. The differences could result from the uncertainty of the input variables (LAI or meteorological data).

Earlier investigations and projects have stated that the $ET_{MOD16A2}$ estimates are generally poor and the accuracy is inconsistent over a period in selected savanna ecosystem sites. According to previous studies, the best performance of the MOD16 product is observed in forested areas, whilst poorer performances are detected in arid and polar climates.

Preceding studies have stated that the estimation of the spatial and temporal distribution of ET_a and LE is important for monitoring ecosystem health, and in improving water resources management in arid and semi-arid environments. Future research should be undertaken, to include the soil moisture influence in the SEBS model, and to effectively represent the influence of water-stress in arid and semi-arid environments. The MOD16A2 product can be used to estimate regional water and energy balance, soil water status. Therefore, providing important information for water resources management, and the provision of long-term data records, that may assist in decision making.

Whilst, the results in this study show unfavourable application of SEO data, other studies show favourable application of SEO data. The application of SEO data products in water resources management creates awareness and assists in the planning of water use and management operations. Current SEO data and products assist in the monitoring of and estimation of regional water and energy balance and soil moisture status. The use of GEE is enabling and empowering the scientific community to monitor, track and manage the Earth's environment and its resources in an easy and time efficient manner (Gorelick *et al.*, 2017). Therefore, providing important information towards water resources management

5.2 Recommendations

The recommendations listed below could be used to address the limitations of the study, and may assist and guide future studies:

- A major limitation at the Malopeni study site (savanna region) was the unavailability of solar radiation, hence solar radiation values were used from nearby sites and used as an input into the SEBS model. Solar radiation estimates are rarely available from meteorological stations and are required in the estimation of ET_a . A lack of solar radiation at study sites, requires the use of models to derive solar radiation estimates (Allen *et al.*, 1998), and this increases uncertainty. Therefore, there is a need for stations to be able to provide solar radiation measurements.
- The study sites were used, due to the availability of data. However, as this study was carried out during the large El Niño drought period, it was able to highlight important facts that should be considered during drought conditions when research and investigations are undertaken. Therefore, the study should be carried out in a region that is not water-stressed and not irrigated, and for a longer time period. This would

enable one to determine distinct differences and seasonal variations, out of drought periods, and a clearer insight into the use of MODIS Terra, MODIS Aqua and the MOD16 product to determine ET_a and terrestrial flux estimates.

- For future studies, the height of the net radiometer should be taken into consideration when placed above the ground, as overestimations and uncertainties may arise as a result of the differences between spatial scales of the SEO data and the *in-situ* data.
- Large amounts of data are required to be processed, hence having the knowledge of coding and the ability to write scripts and the knowledge of python, would make the process much easier and less time consuming. The MOD16 product was accessed via GEE, reducing the computing time and making the satellite earth observed data readily available.
- The validation of the MOD16 and MOD16A2 product should be carried out at multiple sites within arid and semi-arid environments, as this would improve the decisions about the precision of these products within these environments.
- Plant water stress information can be presented into the sensible heat flux solution method, by modifying the kB^{-1} value with a scaling factor, that considers soil moisture and water stress level (Pardo *et al.*, 2014; Li *et al.*, 2015). Subsequently, this method is generally utilised to correct the underestimation of H proposed by Gokmen *et al.* (2012) to reduce the overestimation of LE and EF . Application of the modified SEBS formulation can improve the estimation of energy and water fluxes, in water-stressed regions. The kB^{-1} factor can correct the differences between T_o-T_a , as it is influenced by numerous variables that relate to structural parameters and environmental conditions.
- Uncertainties are presented in the validation results, as micro-meteorological methods provide point-based estimates, as compared to SEO products, where a single pixel is larger than the field of view (Li *et al.*, 2017). A dense network of meteorological stations is essential for a reasonable assessment of satellite and *in-situ* data; therefore, the study could be carried out in an area that contains a denser network of meteorological stations.
- There are inherent weaknesses associated with every SEO sensor available, which are often associated with spatial and temporal resolution. MODIS has a coarse spatial resolution and a high temporal resolution; however, Landsat has a medium to fine spatial resolution and a course temporal resolution (Denis, 2013). Therefore, disaggregation techniques can be performed to address the limitation of the trade-off

between the spatial and temporal resolutions that are associated with satellite imagery (Hong *et al.*, 2011; Spiliotopolous *et al.*, 2013). This would produce better-quality SEO estimates when compared to *in-situ* data, reducing errors and uncertainty; hence assisting in improved water resources management decisions.

- A correction factor or calibration can be introduced for areas with dry bare soil, therefore reducing the overestimation of simulated data when compared against observed data.

6. REFERENCES

- Aguilar, A, Flores, H, Crespo, G, Marín, M, Campos, I and Calera, A. 2018. Performance assessment of MOD16 in evapotranspiration evaluation in Northwestern Mexico. *Water* 10(7):901.
- Allen, RG, Pereira, LS, Raes, D and Smith, M. 1998. Crop evapotranspiration-Guidelines for computing crop water requirements-FAO Irrigation and drainage paper 56. *Fao, Rome*, 300(9):D05109.
- Allen, RG, Tasumi, M and Trezza, R. 2007. Satellite-based energy balance for mapping evapotranspiration with internalized calibration (METRIC)—Model. *Journal of irrigation and drainage engineering* 133(4):380-394.
- Awad, MM. 2019. An innovative intelligent system based on remote sensing and mathematical models for improving crop yield estimation. *Information Processing in Agriculture* 6(3):316-325.
- Badola, A. 2009. Validation of Surface Energy Balance System (SEBS) over forest land cover and sensitivity analysis of the model. *International Institute for Geoinformation Science and Earth Observation*. University of Twente, The Netherlands.
- Baldocchi, DD. 2003. Assessing the eddy covariance technique for evaluating carbon dioxide exchange rates of ecosystems: past, present and future. *Global change biology* 9(4): 479-492.
- Bastiaanssen, WG, Menenti, M, Feddes, RA and Holtslag, AAM. 1998. A remote sensing surface energy balance algorithm for land (SEBAL). 1. Formulation. *Journal of hydrology* 212:198-212.
- Bhattarai, N, Shaw, SB, Quackenbush, LJ, Im, J and Niraula, R. 2016. Evaluating five remote sensing based single-source surface energy balance models for estimating daily evapotranspiration in a humid subtropical climate. *International journal of applied earth observation and geoinformation* 49:75-86.
- Bhattarai, N, Mallick, K, Brunsell, NA, Sun, G and Jain, M. 2018. Regional evapotranspiration from an image-based implementation of the Surface Temperature Initiated Closure (STIC1. 2) model and its validation across an aridity gradient in the conterminous US. *Hydrology and Earth System Sciences* 22(4):2311-2341.

- Bicalho, KV, Araujo, LC, Cui, YJ and Dantas, BT. 2016. Evaluation of empirical methods for estimating potential evaporation values in northeast France. In *E3S Web of Conferences* 9:16005. EDP Sciences.
- Bombelli, A, Henry, M, Castaldi, S, Adu-Bredu, S, Arneth, A, De Grandcourt, A, Grieco, E, Kutsch, W.L, Lehsten, V, Rasile, A and Reichstein, M. 2009. An outlook on the Sub-Saharan Africa carbon balance. *Biogeosciences* (6):2193-2205.
- Brenner, C, Thiem, CE, Wizemann, HD, Bernhardt, M and Schulz, K. 2017. Estimating spatially distributed turbulent heat fluxes from high-resolution thermal imagery acquired with a UAV system. *International journal of remote sensing* 38(8-10):3003-3026.
- Brutsaert, W. 1982. Evaporation into the atmosphere: Theory, history, and applications. D. Reidel Publ., Boston, MA. *Evaporation into the atmosphere: Theory, history, and applications. D. Reidel Publ., Boston, MA.*
- Burba, G and Anderson, D. 2007. Introduction to the eddy covariance method: General guidelines and conventional workflow. *Li-Cor Biosciences*, 15-16.
- Burba, G. 2013. Eddy covariance method for scientific, industrial, agricultural and regulatory applications: A field book on measuring ecosystem gas exchange and areal emission rates. LI-Cor Biosciences.
- Chacko, PT and Renuka, G. 2002. Temperature mapping, thermal diffusivity and subsoil heat flux at Kariavattom of Kerala. *Journal of Earth System Science* 111(1):79-85.
- Chang, Y, Qin, D, Ding, Y, Zhao, Q and Zhang, S. 2018. A modified MOD16 algorithm to estimate evapotranspiration over alpine meadow on the Tibetan Plateau, China. *Journal of hydrology* 561:16-30.
- Che, N, Xiong, X and Barnes, WL. 2003. On-orbit spectral characterization results for of the Terra MODIS reflective solar bands. In *Earth Observing Systems VIII* (5151):367-375. International Society for Optics and Photonics.
- Choudhury, BJ and DiGirolamo, NE. 1998. A biophysical process-based estimate of global land surface evaporation using satellite and ancillary data I. Model description and comparison with observations. *Journal of Hydrology* 205(3-4):164-185.
- Chi, J, Maureira, F, Waldo, S, Pressley, SN, Stöckle, CO, O'Keefe, PT, Pan, WL, Brooks, ES, Huggins, DR and Lamb, BK. 2017. Carbon and water budgets in multiple wheat-based cropping systems in the Inland Pacific Northwest US: comparison of CropSyst simulations with eddy covariance measurements. *Frontiers in Ecology and Evolution* 5:1-18.

- Chirouze, J, Boulet, G, Jarlan, L, Fieuzal, R, Rodriguez, JC, Ezzahar, J, Raki, SE, Bigeard, G, Merlin, O, Garatuza-Payan, J and Watts, C. 2014. Intercomparison of four remote-sensing-based energy balance methods to retrieve surface evapotranspiration and water stress of irrigated fields in semi-arid climate. *Hydrology and Earth System Sciences Discussions* (18):1165-1188.
- Cleugh, HA, Leuning, R, Mu, Q and Running, SW. 2007. Regional evaporation estimates from flux tower and MODIS satellite data. *Remote Sensing of Environment* 106(3):285-304.
- Courault, D, Seguin, B and Olioso, A. 2005. Review on estimation of evapotranspiration from remote sensing data: From empirical to numerical modelling approaches. *Irrigation and Drainage systems* 19(3):223-249.
- Denis, DM. 2013. Irrigation Performance Assessment using SEBS and SCOPE. A case study of Tonness pump Canal Command in India. University of Twente Faculty of Geo-Information and Earth Observation (ITC).
- Dinpashoh, Y. 2006. Study of reference crop evapotranspiration in IR of Iran. *Agricultural Water Management* 84(1-2):123-129.
- Döll, P, Kaspar, F and Lehner, B. 2003. A global hydrological model for deriving water availability indicators: model tuning and validation. *Journal of Hydrology* 270(1): 105-134.
- Drexler, JZ, Snyder, RL, Spano, D and Paw U, KT. 2004. A review of models and micrometeorological methods used to estimate wetland evapotranspiration. *Hydrological Processes*, 18(11):2071-2101.
- Dye, PJ, Gush, MB, Everson, CS, Jarman, C, Clulow, A, Mengistu, M, Geldenhuys, CJ, Wise, R, Scholes, RJ, Archibald, S and Savage, MJ. 2008. Water-use in relation to biomass of indigenous tree species in woodland, forest and/or plantation conditions. *Water Research Commission Report Report No. 361/08*, Water Research Commission, Pretoria, RSA.
- Dzikiti, S, Jovanovic, NZ, Bagan, RD, Ramoelo, A, Majozi, NP, Nickless, A, Cho, MA, Le Maitre, DC, Ntshidi, Z and Pienaar, HH. (2019). Comparison of two remote sensing models for estimating evapotranspiration: algorithm evaluation and application in seasonally arid ecosystems in South Africa. *Journal of Arid Land*, 11(4):495-512.
- Fensholt, R, Langanke, T, Rasmussen, K, Reenberg, A, Prince, SD, Tucker, C, Scholes, RJ, Le, QB, Bondeau, A, Eastman, R and Epstein, H. 2012. Greenness in semi-arid areas across the globe 1981–2007 an Earth Observing Satellite based analysis of trends and drivers. *Remote sensing of environment* 121:144-158.

- Fisher, JB, Tu, KP and Baldocchi, DD. 2008. Global estimates of the land–atmosphere water flux based on monthly AVHRR and ISLSCP-II data, validated at 16 FLUXNET sites. *Remote Sensing of Environment* 112(3):901-919.
- Gao, Y and Long, D. 2008. Intercomparison of remote sensing-based models for estimation of evapotranspiration and accuracy assessment based on SWAT. *Hydrological Processes: An International Journal* 22(25):4850-4869.
- García, M, Sandholt, I, Ceccato, P, Ridler, M, Mougin, E, Kergoat, L, Morillas, L, Timouk, F, Fensholt, R and Domingo, F. 2013. Actual evapotranspiration in drylands derived from in-situ and satellite data: Assessing biophysical constraints. *Remote Sensing of Environment* 131:103-118.
- Gibson, L, Munch, Z, Carstens, M and Conrad, J. 2011. Remote sensing evapotranspiration (SEBS) evaluation using water balance. *Water Research Commission Report No. KV 272/11*, Water Research Commission, Pretoria, RSA.
- Gibson, LA. 2013. The application of the surface energy balance system model to estimate evapotranspiration in South Africa. Doctoral dissertation, Department of Environmental and Geographical Science, University of Cape Town, RSA.
- Gibson, LA, Jarman, C, Su, Z and Eckardt, FE. 2013. Estimating evapotranspiration using remote sensing and the Surface Energy Balance System-A South African perspective. *Water SA* 39(4):477-482.
- Glenn, EP, Huete, AR, Nagler, PL, Hirschboeck, KK and Brown, P. 2007. Integrating remote sensing and ground methods to estimate evapotranspiration. *Critical Reviews in Plant Sciences* 26(3):139-168.
- Glenn, EP, Nagler, PL and Huete, AR. 2010. Vegetation index methods for estimating evapotranspiration by remote sensing. *Surveys in Geophysics* 31(6):531-555.
- Gokmen, M, Vekerdy, Z, Verhoef, A, Verhoef, W, Batelaan, O and Van der Tol, C. 2012. Integration of soil moisture in SEBS for improving evapotranspiration estimation under water stress conditions. *Remote Sensing of Environment* 121:261-274.
- Gokool, S, Chetty, KT, Jewitt, GPW and Heeralal, A. 2016. Estimating total evaporation at the field scale using the SEBS model and data infilling procedures. *Water SA* 42(4): 673-683.
- Gokool, S, Jarman, C, Riddell, E, Swemmer, A, Lerm Jr, R and Chetty, KT. 2017. Quantifying riparian total evaporation along the Groot Letaba River: A comparison between infilled and spatially downscaled satellite derived total evaporation estimates. *Journal of Arid Environments* 147:114-124.

- Gokool, S, Riddell, E, Jarman, C, Chetty, K, Feig, G and Thenga, H. 2019. Evaluating the accuracy of satellite-derived evapotranspiration estimates acquired during conditions of water stress. *International Journal of Remote Sensing* 1-21.
- Gorelick, N, Hancher, M, Dixon, M, Ilyushchenko, S, Thau, D and Moore, R. 2017. Google Earth Engine: Planetary-scale geospatial analysis for everyone. *Remote Sensing of Environment* 202:18-27.
- Gribovszki, Z, Szilágyi, J and Kalicz, P. 2010. Diurnal fluctuations in shallow groundwater levels and streamflow rates and their interpretation—A review. *Journal of Hydrology* 385(1-4):371-383.
- Gu, L, Hu, Z, Yao, J and Sun, G. 2017. Actual and Reference Evapotranspiration in a Cornfield in the Zhangye Oasis, Northwestern China. *Water* 9(7):499.
- Gush, MB. 2016. Water use measurements of an ‘Afourer’ Mandarin orchard in the winter rainfall region of the Western Cape, South Africa. Unpublished WRC report, CSIR, Stellenbosch, RSA.
- Hartanto, IM, Van Der Kwast, J, Alexandridis, TK, Almeida, W, Song, Y, van Andel, SJ and Solomatine, DP. 2017. Data assimilation of satellite-based actual evapotranspiration in a distributed hydrological model of a controlled water system. *International journal of applied earth observation and geoinformation* 57:123-135.
- He, M, Kimball, JS, Yi, Y, Running, SW, Guan, K, Moreno, A, Wu, X and Maneta, M. 2019. Satellite data-driven modeling of field scale evapotranspiration in croplands using the MOD16 algorithm framework. *Remote Sensing of Environment* 230:111201.
- Heritage, GL, Moon, BP and Large, ARG. 2001. The February 2000 floods on the Letaba River, South Africa: an examination of magnitude and frequency. *Koedoe* 44(2):1-6.
- Hollmann, R, Merchant, CJ, Saunders, R, Downy, C, Buchwitz, M, Cazenave, A, Chuvieco, E, Defourny, P, de Leeuw, G, Forsberg, R and Holzer-Popp, T. 2013. The ESA climate change initiative: Satellite data records for essential climate variables. *Bulletin of the American Meteorological Society* 94(10):1541-1552.
- Hong, SH, Hendrickx, JM and Borchers, B. 2011. Down-scaling of SEBAL derived evapotranspiration maps from MODIS (250m) to Landsat (30m) scales. *International journal of remote sensing* 32(21):6457-6477.
- Hu, G, Jia, L and Menenti, M. 2015. Comparison of MOD16 and LSA-SAF MSG evapotranspiration products over Europe for 2011. *Remote Sensing of Environment* 156:510-526.

- Huang, C, Li, Y, Gu, J, Lu, L and Li, X. 2015. Improving estimation of evapotranspiration under water-limited conditions based on sebs and MODIS data in arid regions. *Remote Sensing* 7(12):16795-16814.
- Hulley, GC, Hughes, CG and Hook, SJ. 2012. Quantifying uncertainties in land surface temperature and emissivity retrievals from ASTER and MODIS thermal infrared data. *Journal of Geophysical Research: Atmospheres* 117(D23).
- Huntingford, C, Verhoef, A and Stewart, J. 2000. Dual versus single source models for estimating surface temperature of African savannah. *Hydrology and Earth System Sciences Discussions* 4(1):185-191.
- Indirabai, I, Nair, MH, Nair, JR and Nidamanuri, RR. 2019. Optical Remote Sensing for Biophysical Characterisation in Forests: A Review. *International Journal of Applied Engineering Research* 14(2):344-354.
- Jarmain, C, Mengitsu, M, Jewitt, GPW, Kongo, V and Bastiaanssen, W. 2009. A methodology for near-real time spatial estimation of evaporation. *Water Research Commission Report No: 1751/1/09*, ISBN 978-1-77005-725-8, Water Research Commission, Pretoria, RSA.
- Jensen, ME. 1967. Empirical methods of estimating or predicting evapotranspiration using radiation. In: Proc. ASAE Conference. *Evapotranspiration and Its Role in Water Resources Management*. USA-IL-Chicago, 64:49-53.
- Jones, HG. 1992. *Plants and microclimate: a quantitative approach to environmental plant physiology*. Cambridge University Press.
- Jovanovic, N, Mu, Q, Bagan, RD and Zhao, M. 2015. Dynamics of MODIS evapotranspiration in South Africa. *Water SA* 41(1):79-90.
- Kalma, JD, McVicar, TR and McCabe, MF. 2008. Estimating land surface evaporation: A review of methods using remotely sensed surface temperature data. *Surveys in Geophysics* 29(4-5):421-469.
- Karimi, P, Bongani, B, Blatchford, M and de Fraiture, C. 2019. Global Satellite-Based ET Products for the Local Level Irrigation Management: An Application of Irrigation Performance Assessment in the Sugarbelt of Swaziland. *Remote Sensing* 11(6):705.
- Katambara, Z and Ndiritu, JG. 2010. A hybrid conceptual–fuzzy inference streamflow modelling for the Letaba River system in South Africa. *Physics and Chemistry of the Earth, Parts A/B/C* 35(13-14):582-595.

- Ke, Y, Im, J, Park, S and Gong, H. 2016. Downscaling of MODIS One kilometer evapotranspiration using Landsat-8 data and machine learning approaches. *Remote Sensing* 8(3):215.
- Kelliher, FM, Leuning, R, Raupach, MR and Schulze, ED. 1995. Maximum conductances for evaporation from global vegetation types. *Agricultural and Forest Meteorology* 73(1-2):1-16.
- Khand, K, Taghvaeian, S, Gowda, P and Paul, G. 2019. A modeling framework for deriving daily time series of evapotranspiration maps using a surface energy balance model. *Remote Sensing* 11(5):508.
- Kim, HW, Hwang, K, Mu, Q, Lee, SO and Choi, M. 2012. Validation of MODIS 16 global terrestrial evapotranspiration products in various climates and land cover types in Asia. *KSCE Journal of Civil Engineering* 16(2):229-238.
- Kirton, A and Scholes, RJ. 2012. Site Characterisation of the Malopeni Flux Tower Site, Kruger National Park, South Africa. Ecosystem Processes and Dynamics, Natural Resources and the Environment, CSIR. Available online: http://www.carboafrika.eu/downs/ws/accra/6-Posters/Malopeni_Site_Characterisation.pdf (Accessed: 27 February 2019).
- Kjærsgaard, JH, Cuenca, RH, Martínez-Cob, A, Gavilán, P, Plauborg, F, Møllerup, M and Hansen, S. 2009. Comparison of the performance of net radiation calculation models. *Theoretical and Applied Climatology* 98(1-2):57-66.
- Kogan, F and Guo, W. 2017. Strong 2015–2016 El Niño and implication to global ecosystems from space data. *International Journal of Remote Sensing* 38(1):161-178.
- Kohsiek, W, Meijninger, WML, Moene, AF, Heusinkveld, BG, Hartogensis, OK, Hillen, WCAM and De Bruin, HAR. 2002. An extra large aperture scintillometer for long range applications. *Boundary-Layer Meteorology* 105(1):119-127.
- Kong, J, Hu, Y, Yang, L, Shan, Z and Wang, Y. 2019. Estimation of evapotranspiration for the blown-sand region in the Ordos basin based on the SEBAL model. *International Journal of Remote Sensing* 40(5-6):1945-1965.
- Krause, P, Boyle, DP and Båse, F. 2005. Comparison of different efficiency criteria for hydrological model assessment. *Advances in Geosciences* 5:89-97.
- Kruskal, WH and Wallis, WA. 1952. Use of ranks in one-criterion variance analysis. *Journal of the American statistical Association* 47(260):583-621.
- Kustas, WP and Daughtry, CS. 1990. Estimation of the soil heat flux/net radiation ratio from spectral data. *Agricultural and Forest Meteorology* 49(3):205-223.

- Kustas, WP, Humes, KS, Norman, JM and Moran, MS. 1996. Single-and dual-source modeling of surface energy fluxes with radiometric surface temperature. *Journal of Applied Meteorology* 35(1):110-121.
- Landsberg, JJ and Gower, ST. 1997. *Applications of Physiological Ecology to Forest Management* 40(3):344.
- Li, Y, Zhou, J, Wang, H, Li, D, Jin, R, Zhou, Y and Zhou, Q. 2015. Integrating soil moisture retrieved from L-band microwave radiation into an energy balance model to improve evapotranspiration estimation on the irrigated oases of arid regions in northwest China. *Agricultural and Forest Meteorology* 214:306-318.
- Li, Y, Kustas, WP, Huang, C, Nieto, H, Haghighi, E, Anderson, MC, Domingo, F, Garcia, M and Scott, RL. 2019. Evaluating Soil Resistance Formulations in Thermal-Based Two-Source Energy Balance (TSEB) Model: Implications for Heterogeneous Semiarid and Arid Regions. *Water Resources Research* 55(2):1059-1078.
- Li, ZL, Tang, R, Wan, Z, Bi, Y, Zhou, C, Tang, B, Yan, G and Zhang, X. 2009. A review of current methodologies for regional evapotranspiration estimation from remotely sensed data. *Sensors* 9(5):3801-3853.
- Liang, S. 2001. Narrowband to broadband conversions of land surface albedo I: Algorithms. *Remote Sensing of Environment* 76(2):213-238.
- Liang, S, Shuey, CJ, Russ, AL, Fang, H, Chen, M, Walthall, CL, Daughtry, CST and Hunt, R. 2003. Narrowband to broadband conversions of land surface albedo: II. Validation. *Remote Sensing of Environment* 84(1):25-41.
- Liang, S, Li, X and Wang, J. 2012. *Advanced remote sensing: terrestrial information extraction and applications*. Academic Press 1:501-531.
- Long, D, Longuevergne, L and Scanlon, BR. 2014. Uncertainty in evapotranspiration from land surface modeling, remote sensing, and GRACE satellites. *Water Resources Research* 50(2):1131-1151.
- Lu, J, Li, ZL, Tang, R, Tang, BH, Wu, H, Yang, F, Labed, J and Zhou, G. 2013. Evaluating the SEBS-estimated evaporative fraction from MODIS data for a complex underlying surface. *Hydrological Processes* 27(22):3139-3149.
- Ma, Y, Liu, S, Zhang, F, Zhou, J, Jia, Z and Song, L. 2014. Estimations of regional surface energy fluxes over heterogeneous oasis–desert surfaces in the middle reaches of the Heihe River during HiWATER-MUSOEXE. *IEEE Geoscience and Remote Sensing Letters* 12(3):671-675.

- Massmann, A, Gentine, P and Lin, C. 2019. When does vapor pressure deficit drive or reduce evapotranspiration? *Journal of Advances in Modeling Earth Systems*, 11(10):3305-3320.
- Massman, WJ. 1999. Molecular diffusivities of Hg vapor in air, O₂ and N₂ near STP and the kinematic viscosity and thermal diffusivity of air near STP. *Atmospheric Environment* 33(3):453-457.
- McCabe, MF and Wood, EF. 2006. Scale influences on the remote estimation of evapotranspiration using multiple satellite sensors. *Remote Sensing of Environment*, 105(4): 271-285.
- McCabe, MF, Wood, EF, Wójcik, R, Pan, M, Sheffield, J, Gao, H and Su, H. 2008. Hydrological consistency using multi-sensor remote sensing data for water and energy cycle studies. *Remote Sensing of Environment* 112(2):430-444.
- McCabe, MF, Miralles, DG, Holmes, TR and Fisher, JB. 2019. Advances in the Remote Sensing of Terrestrial Evaporation.
- Menenti, M. 1984. Physical aspects of and determination of evaporation in deserts applying remote sensing techniques. *Report 10 (special issue)*, Institute for Land and Water Management Research (ICW), The Netherlands.
- Menenti, M and Choudhury, BJ. 1993. Parametrization of land surface evapotranspiration using a location-dependent potential evapotranspiration and surface temperature range. In: *Exchange processes at the land surface for a range of space and time scales*, Bolle, H.J. et al. (Eds.). IAHS 212:561–568.
- Menenti, M, Jia, L and Su, Z. 2003. On SEBI-SEBS validation in France, Italy, Spain, USA and China. In *Proceedings of the workshop on use of remote sensing of crop evapotranspiration for large regions. International Commission on Irrigation and Drainage (ICID), Montpellier*.
- Mengistu, MG. 2008. *Heat and energy exchange above different surfaces using surface renewal* (Doctoral dissertation). University of KwaZulu-Natal, Pietermaritzburg.
- Mengistu, MG and Savage, MJ. 2010. Surface renewal method for estimating sensible heat flux. *Water SA* 36(1):9-18.
- Merbold, L, Ardö, J, Arneth, A, Scholes, R.J, Nouvellon, Y, De Grandcourt, A, Archibald, S, Bonnefond, J.M, Boulain, N, Brueggemann, N. and Bruemmer, C. 2009. Precipitation as driver of carbon fluxes in 11 African ecosystems. *Biogeosciences* (6):1027-1041.
- Meyers, TP and Baldocchi, DD. 2005. Current micrometeorological flux methodologies with applications in agriculture. *Micrometeorology in agricultural systems*, 47:381-396.

- Miralles, DG, Holmes, TRH, De Jeu, RAM, Gash, JHC, Meesters, AGCA and Dolman, AJ. 2011. Global land-surface evaporation estimated from satellite-based observations. *Hydrology and Earth System Sciences* 15:453-469.
- Monteith, JL. 1965. Evaporation and environment. In *Symposia of the Society for Experimental Biology* 19(4):205-234.
- Monteith, JL. 1973. *Principles of Environmental Physics*. Edward Arnold Press:241.
- Monteith, J and Unsworth, M. 2013. *Principles of Environmental Physics: plants, animals, and the atmosphere*. Academic Press 4:289-320.
- Montanari, A, Young, G, Savenije, HHG, Hughes, D, Wagener, T, Ren, LL, Koutsoyiannis, D, Cudennec, C, Toth, E, Grimaldi, S and Blöschl, G. 2013. “Panta Rhei—everything flows”: change in hydrology and society—the IAHS scientific decade 2013–2022. *Hydrological Sciences Journal* 58(6):1256-1275.
- Moran, MS, Inoue, Y and Barnes, EM. 1997. Opportunities and limitations for image-based remote sensing in precision crop management. *Remote sensing of Environment* 61(3):319-346.
- Mu, Q, Heinsch, FA, Zhao, M and Running, SW. 2007. Development of a global evapotranspiration algorithm based on MODIS and global meteorology data. *Remote sensing of Environment* 111(4):519-536.
- Mu, Q, Zhao, M and Running, SW. 2011. Improvements to a MODIS global terrestrial evapotranspiration algorithm. *Remote Sensing of Environment* 115(8):1781-1800.
- Mu, Q, Zhao, M and Running, SW. 2013. MODIS global terrestrial evapotranspiration (ET) product (NASA MOD16A2/A3) collection 5. NASA Headquarters. Available from: <https://pdfs.semanticscholar.org/d384/6afef0ea84b40360e7a18d2c76a7d68f24c5.pdf> [Accessed 20 June 2019].
- Muhammed, AH. 2012. Satellite Based Evapotranspiration Estimation and Runoff Simulation: A Topmodel Application to the Gilgel Abay Catchment, Ethiopia. University of Twente Faculty of Geo-Information and Earth Observation (ITC).
- Musselman, RC and Minnick, TJ. 2000. Nocturnal stomatal conductance and ambient air quality standards for ozone. *Atmospheric Environment* 34(5):719-733.
- Odhiambo, GO and Savage, MJ. 2009. Surface layer scintillometry for estimating the sensible heat flux component of the surface energy balance. *South African Journal of Science* 105(5-6):208-216.

- Oku, Y, Ishikawa, H and Su, Z. 2007. Estimation of land surface heat fluxes over the Tibetan Plateau using GMS data. *Journal of Applied Meteorology and Climatology* 46(2):183-195.
- Pan, M, Wood, EF, Wójcik, R and McCabe, MF. 2008. Estimation of regional terrestrial water cycle using multi-sensor remote sensing observations and data assimilation. *Remote Sensing of Environment* 112(4):1282-1294.
- Pardo, N, Sánchez, ML, Timmermans, J, Su, Z, Pérez, IA and García, MA. 2014. SEBS validation in a Spanish rotating crop. *Agricultural and Forest Meteorology* 195:132-142.
- Paul, G, Gowda, PH, Prasad, PV, Howell, TA, Aiken, RM and Neale, CM. 2014. Investigating the influence of roughness length for heat transport (zoh) on the performance of SEBAL in semi-arid irrigated and dryland agricultural systems. *Journal of Hydrology* 509:231-244.
- Pelgrum, H, Miltenburg, I, Cheema, M, Klaasse, A and Bastiaanssen, W. 2010. ETLook a novel continental evapotranspiration algorithm. In *Remote Sensing and Hydrology Symposium, Jackson Hole, Wyoming, USA*.
- Percival, V and Homer-Dixon, T. 1998. Environmental scarcity and violent conflict: the case of South Africa. *Journal of Peace Research* 35(3):279-298.
- Pollard, S and Du Toit, D. 2011. Towards adaptive integrated water resources management in southern Africa: the role of self-organisation and multi-scale feedbacks for learning and responsiveness in the Letaba and Crocodile catchments. *Water Resources Management*, 25(15):4019-4035.
- Pollard, S and Du Toit, D. 2011a. Towards the sustainability of freshwater systems in South Africa: An exploration of factors that enable and constrain meeting the ecological Reserve within the context of Integrated Water Resources Management in the catchments of the lowveld. WRC Report No K8/1711.
- Priestley, CHB and Taylor, RJ. 1972. On the assessment of surface heat flux and evaporation using large-scale parameters. *Monthly weather review* 100(2):81-92.
- Qiu, J, Su, HB, Watanabe, T and Brunet, Y. 1995. Surface renewal analysis: a new method to obtain scalar fluxes. *Agricultural and Forest Meteorology* 74(1-2):119-137.
- Rahman, H and Dedieu, G. 1994. SMAC: a simplified method for the atmospheric correction of satellite measurements in the solar spectrum. *Remote Sensing* 15(1): 123-143.

- Ramoelo, A, Majazi, N, Mathieu, R, Jovanovic, N, Nickless, A and Dzikiti, S. 2014. Validation of global evapotranspiration product (MOD16) using flux tower data in the African savanna, South Africa. *Remote Sensing* 6(8):7406-7423.
- Reusser, DE, Blume, T, Schaefli, B and Zehe, E. 2009. Analysing the temporal dynamics of model performance for hydrological models. *Hydrology and Earth System Sciences* 13(7):999-1018.
- Riddell, ES, Nel, JM, Gokool, S, Jarman, C, Raubenheimer, R, Strydom, T, Swemmer, A. 2017. Quantification of transmission losses along the Letaba River for improved delivery of environmental water requirements (ecological reserve). Water Research Commission Report, Project Number K5/2338.
- Righini, M and Surian, N. 2018. Remote sensing as a tool for analysing channel dynamics and geomorphic effects of floods. In *Flood Monitoring through Remote Sensing* : 27-59.
- Rodriguez, J. 2016. Downscaling Modis Evapotranspiration via Cokriging in Wellton-Mohawk Irrigation and Drainage District, Yuma, AZ. PhD Dissertation, University of Arizona, Tucson, AZ, USA.
- Roxy, MS, Sumithranand, VB and Renuka, G. 2014. Soil heat flux and day time surface energy balance closure at astronomical observatory, Thiruvananthapuram, south Kerala. *Journal of earth system science* 123(4):741-750.
- Running, SW, Nemani, RR, Heinsch, FA, Zhao, M, Reeves, M and Hashimoto, H. 2004. A continuous satellite-derived measure of global terrestrial primary production. *Bioscience* 54(6):547-560.
- Running, SW and Kimball, JS. 2006. Satellite-based analysis of ecological controls for land surface evaporation resistance. *Encyclopedia of Hydrological Sciences*.
- Running, SW, Mu, Q, Zhao, M and Moreno, A. 2017. Modis Global Terrestrial Evapotranspiration (ET) Product (NASA MOD16A2/A3) NASA Earth Observing System Modis Land Algorithm. *NASA: Washington, DC, USA*.
- Running, SW, Mu, Q, Zhao, M and Moreno, A. 2019. MODIS Global Terrestrial Evapotranspiration (ET) Product (MOD16A2/A3 and Year-end Gap-filled MOD16A2GF/A3GF) NASA Earth Observing System MODIS Land Algorithm (For Collection 6).
- Salomonson, VV, Guenther, B and Masuoka, E. 2001. A summary of the status of the EOS Terra Mission Moderate Resolution Imaging Spectroradiometer (MODIS) and attendant data product development after one year of on-orbit performance. In

- Geoscience and Remote Sensing Symposium, 2001. IGARSS'01. IEEE 2001 International* (3):1197-1199.
- Sauer, TJ and Horton, R. 2005. Soil heat flux. *Micrometeorology in Agricultural Systems Agronomy Monograph* 47:131-154.
- Savage, MJ, Everson, CS, Odhiambo, GO, Mengistu, MG and Jarman, C. 2004. Theory and practice of evaporation measurement, with special focus on surface layer scintillometry as an operational tool for the estimation of spatially averaged evaporation. *Water Research Commission Report* number 1335/1/04:204.
- Savtchenko, A, Ouzounov, D, Ahmad, S, Acker, J, Leptoukh, G, Koziana, J and Nickless, D. 2004. Terra and Aqua MODIS products available from NASA GES DAAC. *Advances in Space Research* 34(4):710-714.
- Sazib, N, Mladenova, I and Bolten, J. 2018. Leveraging the google earth engine for drought assessment using global soil moisture data. *Remote Sensing* 10(8):1265.
- Schmugge, TJ, Kustas, WP, Ritchie, JC, Jackson, TJ and Rango, A. 2002. Remote sensing in hydrology. *Advances in Water Resources* 25(8):1367-1385.
- Schulze, ED, Kelliher, FM, Körner, C, Lloyd, J and Leuning, R. 1994. Relationships among maximum stomatal conductance, ecosystem surface conductance, carbon assimilation rate, and plant nitrogen nutrition: a global ecology scaling exercise. *Annual Review of Ecology and Systematics* 25(1):629-662.
- Schulze, RE. 2008. Electronic version of the South African atlas of climatology and agrohydrology. South African Atlas of Climatology and Agrohydrology. RE Schulze. Water Research Commission, Pretoria, South Africa, WRC Report 1489/1/06, Section 1.1.
- Scott, RL. 2010. Using watershed water balance to evaluate the accuracy of eddy covariance evaporation measurements for three semiarid ecosystems. *Agricultural and Forest Meteorology* 150(2):219-225.
- Seneviratne, SI, Corti, T, Davin, EL, Hirschi, M, Jaeger, EB, Lehner, I, Orlowsky, B and Teuling, AJ. 2010. Investigating soil moisture–climate interactions in a changing climate: A review. *Earth-Science Reviews* 99(3-4):125-161.
- Sinha, PK and Kumar, R. 2015. Statistical analysis to investigate the possible impact of climate change on water availability in Letaba river of South Africa. *International Journal of Recent Technology and Engineering* 3(6):41-51.

- Small, EE and Kurc, S. 2001. *The influence of soil moisture on the surface energy balance in semiarid environments* (No. 318). New Mexico Water Resources Research Institute, New Mexico State University.
- Small, EE and Kurc, SA. 2003. Tight coupling between soil moisture and the surface radiation budget in semiarid environments: Implications for land-atmosphere interactions. *Water Resources Research* 39(10):11-13.
- Snyder, RL, Spano, D and Pawu, KT. 1996. Surface renewal analysis for sensible and latent heat flux density. *Boundary-Layer Meteorology* 77(3-4):249-266.
- Sobrino, JA, El Kharraz, J and Li, ZL. 2003. Surface temperature and water vapour retrieval from MODIS data. *International Journal of Remote Sensing* 24(24):5161-5182.
- Song, X, Lu, F, Xiao, W, Zhu, K, Zhou, Y and Xie, Z. 2019. Performance of 12 reference evapotranspiration estimation methods compared with the Penman–Monteith method and the potential influences in northeast China. *Meteorological Applications* 26(1):83-96.
- Spiliotopoulos, M, Adaktylou, N, Loukas, A, Michalopoulou, H, Mylopoulos, N and Toullos, L. 2013. A spatial downscaling procedure of MODIS derived actual evapotranspiration using Landsat images at central Greece. In *First International Conference on Remote Sensing and Geoinformation of the Environment (RSCy2013); SPIE Conference Proceedings*.
- Spittlehouse, DL and Black, TA. 1980. Evaluation of the Bowen ratio/energy balance method for determining forest evapotranspiration. *Atmosphere-Ocean* 18(2):98-116.
- Stancalie, G, Marica, A and Toullos, L. 2010. Using earth observation data and CROPWAT model to estimate the actual crop evapotranspiration. *Physics and Chemistry of the Earth, Parts A/B/C* 35(1-2):25-30.
- Strydom, T, Riddell, ES, Swemmer, A, Nel, JM and Jarman, C. 2014. Quantification of transmission processes along the Letaba River for improved delivery of environmental water requirements (Ecological Reserve). *WRC Report no. K5/2338/1*. Water Research Commission, Pretoria, RSA.
- Su, H, McCabe, MF, Wood, EF, Su, Z and Prueger, J H. 2005. Modelling evapotranspiration during SMACEX: Comparing two approaches for local-and regional-scale prediction. *Journal of Hydrometeorology* 6(6):910-922.
- Su, Z and Jacobs, C. 2001. ENVISAT: actual evaporation. BCRS Report 2001: USP-2 Report 2001. *Publication of the National Remote Sensing Board (BCRS), Delft*.

- Su, Z. 2002. The Surface Energy Balance System (SEBS) for estimation of turbulent heat fluxes. *Hydrology and Earth System Sciences Discussions* 6(1):85-100.
- Su, Z and Wang, L. 2013. Earth Observation of Water Resources (SEBS). Practical Session Instructions (July 2013). ITC. University of Twente. The Netherlands.
- Sugita, F and Kishii, T. 2002. Effect of roughness distribution on evaporation processes over non-homogeneous sand surfaces: a wind tunnel investigation. *Hydrological Processes* 16(11):2141-2153.
- Sumithranand, VB, Roxy, MS and Renuka, G. 2009. Variability of surface albedo with soil moisture and soil temperature at Astronomical Observatory, Thiruvananthapuram; *Ultra Sci* 21(1):63-66.
- Sun, H, Yang, Y, Wu, R, Gui, D, Xue, J, Liu, Y and Yan, D. 2019. Improving Estimation of Cropland Evapotranspiration by the Bayesian Model Averaging Method with Surface Energy Balance Models. *Atmosphere* 10(4):188.
- Szporak-Wasilewska, S, Szatyłowicz, J, Okruszko, T and Ignar, S. 2013. Application of the Surface Energy Balance System Model (SEBS) for mapping evapotranspiration of extensively used river valley with wetland vegetation. *Towards Horiz* 2020:929-942.
- Tang, R, Li, ZL and Chen, KS. 2011. Validating MODIS-derived land surface evapotranspiration with in-situ measurements at two AmeriFlux sites in a semiarid region. *Journal of Geophysical Research: Atmospheres* 116(D4):6-11.
- Thiermann, V and Grassl, H. 1992. The measurement of turbulent surface-layer fluxes by use of bichromatic scintillation. *Boundary-Layer Meteorology* 58(4):367-389.
- Thornton, PE. 1998. Regional ecosystem simulation: combining surface-and satellite-based observations to study linkages between terrestrial energy and mass budgets. PhD Dissertation, School of Forestry, The University of Montana, Missoula, MT.
- Thornthwaite, CW. 1948. An approach toward a rational classification of climate. *Geographical review* 38(1):55-94.
- Timmermans, WJ, Su, Z and Olioso, A. 2009. Footprint issues in scintillometry over heterogeneous landscapes. *Hydrology and Earth System Sciences* 13(11):2179-2190.
- Timmermans, J, Su, Z, Tol, C, Verhoef, A and Verhoef, W. 2013. Quantifying the uncertainty in estimates of surface-atmosphere fluxes through joint evaluation of the SEBS and SCOPE models. *Hydrology and earth system sciences* 17(4):1561-1573.
- Troufleau, D, Lhomme, JP, Monteny, B and Vidal, A. 1997. Sensible heat flux and radiometric surface temperature over sparse Sahelian vegetation. I. An experimental analysis of the kB- 1 parameter. *Journal of Hydrology* 188:815-838.

- Tsouni, A, Kontoes, C, Koutsoyiannis, D, Elias, P and Mamassis, N. 2008. Estimation of actual evapotranspiration by remote sensing: Application in Thessaly Plain, Greece. *Sensors* 8(6):3586-3600.
- United States Geological Survey (USGS). 2016. Landsat 8 (18) Data Users Handbook. Version 2.0.
- van de Griend, AA and Owe, M. 1994. Bare soil surface resistance to evaporation by vapor diffusion under semiarid conditions. *Water Resources Research* 30(2):181-188.
- Van der Kwast, J, Timmermans, W, Gieske, A, Su, Z, Oliso, A, Jia, L, Elbers, J, Karssenber, D and de Jong, S. 2009. Evaluation of the Surface Energy Balance System (SEBS) applied to ASTER imagery with flux-measurements at the SPARC 2004 site (Barrax, Spain). *Hydrology and Earth System Sciences Discussions* 6(1):1165-1196.
- Wagle, P, Bhattarai, N, Gowda, PH and Kakani, VG. 2017. Performance of five surface energy balance models for estimating daily evapotranspiration in high biomass sorghum. *ISPRS Journal of Photogrammetry and Remote Sensing* 128:192-203.
- Wallace, JS and Holwill, CJ. 1997. Soil evaporation from tiger-bush in south-west Niger. *Journal of Hydrology* 188:426-442.
- Wheater, H, Sorooshian, S and Sharma, KD. 2007. *Hydrological modelling in arid and semi-arid areas*. Cambridge University Press 30-32.
- White, MA, Thornton, PE, Running, SW and Nemani, RR. 2000. Parameterization and sensitivity analysis of the BIOME-BGC terrestrial ecosystem model: net primary production controls. *Earth interactions* 4(3):1-85.
- Wilcox, BP, Seyfried, MS, Breshears, DD, Stewart, B and Howell, T. 2003. The water balance on rangelands. *Encyclopedia of water science* 791-794.
- Willmott, CJ and Matsuura, K. 2005. Advantages of the mean absolute error (MAE) over the root mean square error (RMSE) in assessing average model performance. *Climate research* 30(1):79-82.
- Xiong, X, Wu, A and Cao, C. 2008. On-orbit calibration and inter-comparison of Terra and Aqua MODIS surface temperature spectral bands. *International Journal of Remote Sensing* 29(17-18):5347-5359.
- Xiong, X, Chiang, K, Sun, J, Barnes, WL, Guenther, B and Salomonson, VV. 2009. NASA EOS Terra and Aqua MODIS on-orbit performance. *Advances in Space Research* 43(3):413-422.

- Xu, T, Liu, S, Liang, S and Qin, J. 2011. Improving predictions of water and heat fluxes by assimilating MODIS land surface temperature products into the common land model. *Journal of Hydrometeorology* 12(2):227-244.
- Xue, J and Su, B. 2017. Significant remote sensing vegetation indices: A review of developments and applications. *Journal of Sensors* 2017:1-9.
- Yagci, AL and Santanello, JA. 2017. Estimating Evapotranspiration From Satellite Using Easily Obtainable Variables: A Case Study Over the Southern Great Plains, USA. *IEEE journal of selected topics in applied earth observations and remote sensing* 11(1):12-23.
- Yi, Z, Zhao, H, Jiang, Y, Yan, H, Cao, Y, Huang, Y and Hao, Z. 2018. Daily Evapotranspiration Estimation at the Field Scale: Using the Modified SEBS Model and HJ-1 Data in a Desert-Oasis Area, Northwestern China. *Water* 10(5):640.
- Zhao, L, Xia, J, Xu, CY, Wang, Z, Sobkowiak, L and Long, C. 2013. Evapotranspiration estimation methods in hydrological models. *Journal of Geographical Sciences* 23(2): 359-369.
- Zhao, M, Heinsch, FA, Nemani, RR and Running, SW. 2005. Improvements of the MODIS terrestrial gross and net primary production global data set. *Remote sensing of Environment* 95(2):164-176.
- Zheng, C, Jia, L, Hu, G and Lu, J. 2019. Earth Observations-Based Evapotranspiration in Northeastern Thailand. *Remote Sensing* 11(2):138.
- Zhuang, Q and Wu, B. 2015. Estimating evapotranspiration from an improved two-source energy balance model using ASTER satellite imagery. *Water* 7(12):6673-6688.
- Zhuang, Q, Wu, B, Yan, N, Zhu, W and Xing, Q. 2016. A method for sensible heat flux model parameterization based on radiometric surface temperature and environmental factors without involving the parameter KB^{-1} . *International journal of applied earth observation and geoinformation* 47:50-59.
- Zitouna-Chebbi, R, Prévot, L, Chakhar, A, Marniche-Ben Abdallah, M and Jacob, F. 2018. Observing actual evapotranspiration from flux tower eddy covariance measurements within a hilly watershed: Case study of the Kamech site, Cap Bon Peninsula, Tunisia. *Atmosphere* 9(2):68.

7. APPENDICES

This chapter contains further information pertaining to the methodology of this study.

7.1 Appendix A

This section contains the acquisition of the $ET_{MOD16A2}$ estimates and the conversion of the $ET_{MOD16A2}$ product into a GeoTiff format.

```
Imports (1 entry)
1  /// Add region of interest
2  Map.addLayer(Site1, {}, 'Malopeni')
3
4  //Collect data and filter by dates
5  var ET = ee.ImageCollection('MODIS/006/MOD16A2')
6  .filterDate('2015-01-01', '2015-12-31')
7
8  //Clip and display ET data for region of interest
9  var ET_Site1 = ET.map(function(img) {return img.clip(Site1)})
10 Map.addLayer(ET_Site1)
11 Map.centerObject(Site1)
12
13 // Multiply by ET scale factor
14 ET = ET.map(
15   function(img) {
16     var rescaled_ET = img.select('ET')
17       .multiply(0.1)
18       .rename('ET_rescaled');
19     return img.addBands(rescaled_ET);
20   }
21 );
22
23 //ET Time-Series plot
24 print (ui.Chart.image.seriesByRegion(ET, Site1, ee.Reducer.mean(), 'ET_rescaled', 500, 'system:time_start')
25   .setOptions({title: 'ET Long-Term Series',
26     vAxis: {title: 'ET'},
27   })))
28
29 // Export a .csv table of date, mean ET for watershed
30 Export.table.toDrive({
31   collection: ET,
32   description: 'MODIS_ET_stats',
33   folder: 'Trial',
34   fileFormat: 'CSV'
35 });
36
37
```

Figure 7.1 Sample of the code used to extract ET_a data from the MOD16A2 product for the Malopeni (savanna) study site

```

MOD16ET_Export image
Get Link Save Run Reset
Imports (1 entry)
  ▶ var Letaba: Polygon, 4 vertices
1 var MOD16 = ee.ImageCollection('MODIS/006/MOD16A2')
2   .filter(ee.Filter.date('2015-06-19', '2015-06-27'))
3   .filterBounds(Letaba)
4
5 var ET_scaled = MOD16.map(function(img)
6   {var rescaled_ET = img.select('ET')
7     .multiply(0.1)
8     .rename('ET_rescaled');
9   return img.addBands(rescaled_ET)})
10
11 //Clip and display for ROI
12 var ET_select = ET_scaled.select('ET_rescaled');
13
14 var ETVis = {
15   min: 0.0,
16   max: 80.0,
17   palette: [
18     'ffffff', 'fcd163', '99b718', '66a000', '3e8601', '207401', '056201',
19     '004c00', '011301'
20   ],
21 };
22 var ET_site1 = ET_select.map(function(img) {return img.clip(Letaba)})
23   // .sort('ET_QC')
24   .first()
25
26 Map.centerObject(Letaba, 12);
27 Map.addLayer(ET_site1, ETVis, 'Evapotranspiration');
28
29 //ET image
30 Export.image.toDrive({
31   image: ET_site1,
32   description: 'ETtoGeoTiff',
33   scale: 500,
34   fileFormat: 'GeoTiff'})
35
36

```

Figure 7.2 The script used to export an image into a GeoTiff format